Aptamers that bind SARS-CoV-2 spike protein for COVID-19 rapid diagnostics and therapeutics

Lucy Fifi Yang

A dissertation
submitted in partial fulfillment
of the requirements for the degree of

Doctor of Philosophy

University of Washington

2022

Reading Committee:

Suzie H. Pun, Chair

Patrick Stayton

Bo Zhang

Program Authorized to Offer Degree:

Bioengineering

University of Washington

Abstract

Aptamers that bind SARS-CoV-2 spike protein for COVID-19 rapid diagnostics and therapeutics

Lucy Fifi Yang

Chair of the Supervisory Committee:
Dr. Suzie H. Pun
Bioengineering

The coronavirus disease 2019 (COVID-19) pandemic continues to severely impact healthcare and socioeconomic circumstances despite advances in rapid diagnostics and vaccines. One hurdle is the emergence of SARS-CoV-2 variants of concern, including the Omicron variant, which has enhanced infectivity and immune invasion. Improved rapid tests can limit viral spread by informing individuals of their infection status for personal risk assessment as well as disease surveillance. To that end, DNA aptamer-based rapid diagnostics show promise as cost-effective, shelf-stable alternatives to those based on antibodies. In the introduction, I discuss what DNA aptamers are, how they are discovered, and how they are applied to biosensing. In chapter 1, we selected for novel DNA aptamers that bind to the SARS-CoV-2 spike glycoprotein with high specificity and affinity (< 80 nM). Through binding assays and high resolution cryo-EM, we demonstrate that SNAP1 (SARS-CoV-2 spike protein N-terminal domain-binding aptamer 1) binds to the S N-terminal domain. We applied SNAP1 in lateral flow assays (LFAs) and ELISAs to detect UV-inactivated SARS-CoV-

2 at concentrations as low as 5 x 10^5 copies/mL. In chapter 2, we describe a new aptamer that also binds wild-type spike protein at the NTD, named SARS-CoV-2 spike protein NTD-binding DNA aptamer 4 (SNAP4). SNAP4 binds with high affinity (< 30 nM) for SARS-CoV-2 spike protein, a 2-fold improvement over SNAP1. We utilized both SNAP1 and SNAP4 in an aptamer sandwich LFA (AptaFlow), which detected UV-inactivated intact SARS-CoV-2 virus at concentrations as low as 10^6 copies/mL. AptaFlow costs <$1 per test to produce, provides results in < 1 hour, and detects SARS-CoV-2 at concentrations that indicate higher viral loads and high probability of contagious transmission. In chapter 3, I will describe another new aptamer, SARS-CoV-2 Omicron RBD-binding aptamer (SCORe) which binds Omicron BA.1 and BA.2 RBD with nanomolar K_{D1}. We employed aptamers SCORe.50 and SNAP4.74 in a multiplexed lateral flow assay (LFA) to distinguish between Omicron and wild-type spike protein at concentrations as low as 100 pM. Finally, we show that SCORe.50 and its dimerized form SCOReD can neutralize Omicron spike-pseudotyped virus infection of ACE2-overexpressing cells by >70%. Taken together, the aptamers SNAP1, SNAP4, and SCORe demonstrate great potential in low-cost, convenient, and rapid COVID-19 diagnostics.

Table of Contents

Executive Summary

The coronavirus disease 2019 (COVID-19) pandemic, which emerged from the Hubei Province of China in late-2019, has overwhelmed healthcare systems, devastated economies, and disrupted social behavior worldwide[1–5]. Effective disease control requires both disease prevention and early detection of SARS-CoV-2, the coronavirus that causes COVID-19. Despite the authorization of vaccines, the COVID-19 pandemic remains uncontrolled and at the forefront of health and socioeconomic concerns. As of the writing of this document, variants of SARS-CoV-2 with multiple mutations have emerged and drive new infections and hospitalizations[6]. In fact, the original strain that entered the US in early 2020 is no longer in circulation[7]. The delicate balance of infection prevent measures emphasizes the critical need for COVID-19 diagnostic tools. Furthermore, advances in rapid diagnostics are necessary to be better prepared for the next pandemic[8].

There are two major categories of COVID-19 diagnostic tests for active infections: 1) molecular tests that detect viral RNA, and 2) rapid antigen tests that detect viral proteins. Molecular tests use methods such as quantitative PCR to amplify viral genetic material, and are therefore extremely sensitive and specific[9]. However, molecular tests take time to process since they require trained personnel and specialized machinery and reagents, which are not readily available in developing countries and can be severely limited by supply chain issues[10,11]. On the other hand, rapid antigen tests are simple to administer, provide point-of-care results within 30 minutes, and are less expensive than molecular tests[12,13]. While existing rapid antigen tests are not as sensitive as molecular tests[14–16], they are useful as high-throughput screens that can mitigate transmission in an emergent pandemic. In fact, rapid antigen testing has been shown to reduce COVID-19 prevalence by an estimated 70% compared to unmitigated growth[7].

A major SARS-CoV-2 antigen detected by COVID-19 diagnostics is the spike (S) protein, a transmembrane glycoprotein that protrudes from the viral envelope[17,18]. Antibodies against SARS-CoV-2 S protein have been isolated[19–21], and mRNA encoding the S protein is the basis of FDA-authorized mRNA vaccines[22,23]. SARS-CoV-2, a betacoronavirus, is closely related to SARS-CoV, which caused the 2002-2003 Severe Acute Respiratory Syndrome epidemic, and more distantly related to the MERS-CoV responsible for the 2012 Middle East Respiratory Syndrome outbreak, sharing ~72% and ~35% sequence similarity, respectively, with the S proteins of these viruses[18]. The SARS-CoV-2 S protein is composed of three identical monomers with two distinct subunits[24,25]. Subunit 1 (S1) contains a receptor binding domain (RBD), which binds to human angiotensin-converting enzyme 2 (ACE2) and mediates host cell recognition, and an N-terminal domain (NTD[17,24]. Recently, an antigenic supersite on the NTD was found to be frequently targeted by NTD-binding antibodies[19], indicating that binders to this site may play a role in specific recognition of and immunity to SARS-CoV-2.

Nucleic acid aptamers are short sequences of RNA or DNA that specifically bind target molecules and offer unique advantages as molecular recognition agents for SARS-CoV-2. Aptamers not only achieve specific binding with affinities on par with antibodies, but also are less expensive to synthesize, more stable, and more scalable for production[26–28]. Due to these features, aptamers have been applied to medical applications ranging from therapeutics to diagnostics[29–32]. Novel aptamers are discovered through a library selection method coined systematic evolution of ligands by exponential enrichment (SELEX)[33–35], which can be applied to select aptamer sequences that bind to small molecules, proteins, and whole cells[36,37]. For detection of intact SARS-CoV-2 virus, aptamers that bind to accessible surface proteins such as S are needed.

In the introduction (chapter 0), I review the current landscape of aptamer selection and their applications in biosensing. I dive deep into SELEX and explore each stage in detail, discuss aptamer characterization methods, and new strategies for aptamer optimization. Then, I examine aptamer-based biosensors, including electrochemical sensors, paper-based diagnostics, and microfluidic sensors. Overall, I introduce aptamers and feature the latest innovations on aptamer discovery and biosensing applications.

In chapter 1, I report the discovery and optimization of DNA aptamers that bind the wild-type strain of SARS-CoV-2 S protein with high affinity and demonstrate the application of these aptamers in SARS-CoV-2 S protein detection. We performed 12 rounds of protein SELEX to identify two high-affinity DNA aptamers (SNAP1 and SNAP3) that specifically bind recombinant SARS-CoV-2 S1, but not SARS-CoV S1 or MERS-CoV S1. Then, we identified the binding epitope of the aptamers as the NTD of the SARS-CoV-2 S protein by biolayer interferometry (BLI) and cryogenic electron microscopy (Cryo-EM). As a proof of concept, we used SNAP1 to detect S protein by lateral flow assay and by ELISA. Together, the data demonstrate that DNA aptamers can effectively detect SARS-CoV-2 S protein and are promising tools for inexpensive, rapid diagnostics platforms.

As the COVID-19 pandemic progressed, variants of SARS-CoV-2 with multiple mutations have emerged and drive new infections and hospitalizations[6]. One variant of concern, the B.1.1.7 “alpha variant”, has 17 defining mutations, of which nine (Δ69-

70 HV, del144 Y, N501Y, A570D, D614G, P681H, T761I, S982A, D1118H) are on the S protein[6,38]. Most mutations are expected to not confer an evolutionary advantage due to carry-over or founder effect[39]. However, some mutations can give an evolutionary advantage, such as increasing infectivity or preventing immune detection[40,41]. For example, the N439K and Y453F mutations were reported to increase ACE2 receptor binding affinity, while the Δ69-70 HV was shown to increase infectivity [38,42].

The constantly changing landscape of SARS-CoV-2 variants not only threatens efficacy of treatment and vaccines, but also the accuracy of diagnostic tests[43,44]. A mutation at a critical area, like the complementary site for a PCR primer[45] or epitope of a detection antibody[46], have compromised detection assays. In fact, we observed that SNAP1 only tightly bound the original wild-type strain S protein compared to a stabilized original strain S protein named S-2P or alpha variant S protein. As a result, in chapter 2, I developed an antibody-free aptamer-based lateral flow assay ("AptaFlow") utilizing a newly identified aptamer. I implemented a new SELEX strategy using S-2P expressed on cells, S-2P protein, and alpha S protein as selection targets. I discovered a new sequence named SARS-CoV-2 NTD binding Aptamer 4 (SNAP4), which binds specifically to the NTD with < 30 nM affinity. I utilized both SNAP1 and SNAP4 in an aptamer sandwich lateral flow assay (AptaFlow), which detected SARS-CoV-2 UV-inactivated virus at concentrations as low as 10^6 copies/mL. AptaFlow costs <$1 per test to produce, provides results in <1 hour, and detects SARS-CoV-2 at concentrations that indicate higher viral loads and high probability of contagious transmission. AptaFlow is therefore a potential approach for a low-cost, convenient antigen test to aid the control of the COVID-19 pandemic.

SARS-CoV-2 continued to adapt and change during the progress of my thesis, and the Omicron variant became the most recent and abundant variant at the time of writing. The Omicron variant (B.1.1.529 AKA BA.1, BA.2, BA.2.12.1, BA.4, BA.5, etc.) dominated SARS-CoV-2 infections in the U.S. starting December 2021, accounting for virtually all new SARS-CoV-2 infections starting from 4/9/2022 to 7/9/2022 (the time of this writing).[7] During the beginning “wave” on infection, there was little opportunity for the average citizen to test whether they caught Delta or Omicron variant SARS-CoV-2, or if they caught another virus entirely. Therefore, it would be prudent to develop diagnostic tests that can reliably bind to and distinguish between specific mutations or variants of SARS-CoV-2, or even test for influenza virus or other viruses of interest. Genomic sequencing is used to monitor mutations and variants and is informative for epidemiological tracking and infection control policies[47]. However, sequencing is time- and resource-intensive and only feasible in well-equipped facilities and these factors limit its surveillance applications. In contrast, a rapid antigen test can deliver point-of-care results and cost less, which would allow wider adoption compared to sequencing.

To that end, in chapter 3, I discovered an Omicron-specific aptamer and applied it to a multiplex lateral flow assay as a proof-of-concept rapid test for distinguishing between two variants. First, I successfully enriched for a SARS-CoV-2 Omicron RBD binding aptamer (SCORe) that binds Omicron BA.1 and BA.2 RBD with nanomolar K_{D1}. I employed aptamers SCORe.50 and SNAP4.74 in a multiplexed lateral flow assay (LFA) to distinguish between Omicron and wild-type S at concentrations as low as 100 pM. Finally, we show that SCORe.50 and its dimerized form SCOReD can neutralize Omicron S-pseudotyped virus infection of ACE2-overexpressing cells by

>70%. SCORe therefore has potential applications in COVID-19 rapid diagnostics as well as in viral neutralization.

The COVID-19 pandemic not only spurred investigation into effective diagnostics for prevention, but also underscored the risks associated with existing diseases once infected. Many underlying conditions increase the risk of severe COVID-19, including diabetes, obesity, and chronic kidney disease (CKD)[48–50]. In CKD, the kidneys progressively lose function because of injury and fibrosis, leading to a decrease in the glomerular filtration rate (GFR). Although about 15% of U.S. adults have CKD[51], the disease often goes unnoticed until symptoms appear when kidney function is greatly impaired[52]. At that point, it leads to end-stage renal disease (ESRD) and the only therapies available are dialysis or kidney organ transplantation. However, chronic dialysis is costly and detrimental to daily life, and donor kidneys are in short supply[52]. Thus, more effective treatments for CKD are needed[53].

On a pathogenic level, CKD is caused by maladaptive injury response. Chronic or severe injuries corrupt repair pathways meant to heal, leading to inflammation and fibrosis. However, the cellular origins of renal myofibroblasts and collagen in fibrosis are not well understood[54]. Several cell types execute maladaptive injury responses, including epithelial cells, myofibroblasts, endothelial cells, and immune cells[55]. Recently, tubular epithelial cells (TECs) that undergo a epithelial to mesenchymal transition (EMT) are suspected as mediators of renal fibrosis[54,56]. During EMT, cells become mobile, lose epithelial markers, like e-cadherin and zonula occludens-1 (ZO-1), and gain mesenchymal markers, such as vimentin and alpha-SMA. TECs that undergo EMT no longer retain their regular functions and are suspected to become myofibroblasts[55]. These changes are orchestrated by EMT-inducing transcription factors like Snail1. Targeted downregulation of Snail1 can revert fibrosis[57] and is a potential method for inhibiting CKD. Epigallocatechin-3-gallate (EGCG) is the active compound in green tea and has anti-fibrotic properties effective in several diseases[58–64]. In relation to CKD, EGCG has been reported to inhibit EMT in renal tubular cells through two pathways, including one that uses Snail1[65]. Thus, delivering EGCG to TECs could be a strategy to attenuate fibrosis in CKD.

In chapter 4, I discuss preliminary findings on EGCG as a potential delivery cargo in boronic acid-based polymers for targeted delivery to renal TECs to treat CKD. Previously, we have demonstrated that highly anionic polymers ~25 kDa in size preferentially accumulate in kidney proximal tubule cells[66]. In addition, we have shown that boronic acid polymers can deliver catechol-containing drug Bis-T-23 into kidney cells[67]. EGCG contains two catechols and is therefore highly suitable for conjugation to a boronic acid polymer. In ongoing work, we confirm that EGCG given in solution inhibits TGFB-1 induced EMT in human tubular epithelial cells by measuring gene and protein expression of vimentin, alpha-SMA, ZO-1, and Snail1. We design and characterize boronic acid polymers with the size and charge properties previously shown to accumulate in proximal tubule cells. These polymers in efficacy and toxicity studies in cells and CKD model animals.

References

1. Zhou, P. *et al.* A pneumonia outbreak associated with a new coronavirus of probable bat origin. *Nature* **579**, 270–273 (2020).
2. Wu, F. *et al.* A new coronavirus associated with human respiratory disease in China. *Nature* **579**, 265–269 (2020).
3. Zhu, N. *et al.* A novel coronavirus from patients with pneumonia in China, 2019. *N. Engl. J. Med.* **382**, 727–733 (2020).
4. Ramelli, S. & Wagner, A. THE UNPRECEDENTED STOCK MARKET IMPACT OF COVID-19. *NBER Work. Pap. Ser.* (2020) doi:10.1093/rcfs/cfaa012.
5. Spinelli, A. & Pellino, G. COVID-19 pandemic: perspectives on an unfolding crisis. *Br. J. Surg.* **107**, 785–787 (2020).
6. Lauring, A. S. & Hodcroft, E. B. Genetic Variants of SARS-CoV-2—What Do They Mean? *JAMA* **325**, 529 (2021).
7. CDC. COVID Data Tracker. *Centers for Disease Control and Prevention* https://covid.cdc.gov/covid-data-tracker (2020).
8. Simpson, S., Kaufmann, M. C., Glozman, V. & Chakrabarti, A. Disease X: accelerating the development of medical countermeasures for the next pandemic. *Lancet Infect. Dis.* **20**, e108–e115 (2020).
9. Joung, J., Ladha, A. ,. Saito, M. ,. Kim, N. G. ,. Woolley, A. E. ,. Segel, M. ,. .. .. .. &. Zhang, F. Detection of SARS-CoV-2 with SHERLOCK One-Pot Testing. *N. Engl. J. Med.* (2020).
10. Freire-Paspuel, B. *et al.* Cotton-Tipped Plastic Swabs for SARS-CoV-2 RT-qPCR Diagnosis to Prevent Supply Shortages. *Front. Cell. Infect. Microbiol.* **10**, 356 (2020).

11. Comparison of Copan ESwab and FLOQSwab for COVID-19 Diagnosis: Working around a Supply Shortage | Journal of Clinical Microbiology. https://journals.asm.org/doi/full/10.1128/JCM.00669-20.
12. Dinnes, J. *et al.* Rapid, point-of-care antigen and molecular-based tests for diagnosis of SARS-CoV-2 infection. *Cochrane Database Syst. Rev.* (2021) doi:10.1002/14651858.CD013705.pub2.
13. Evaluation of a Rapid Diagnostic Assay for Detection of SARS-CoV-2 Antigen in Nasopharyngeal Swabs | Journal of Clinical Microbiology. https://journals.asm.org/doi/full/10.1128/JCM.00977-20.
14. Scohy, A. *et al.* Low performance of rapid antigen detection test as frontline testing for COVID-19 diagnosis. *J. Clin. Virol.* **129**, 104455 (2020).
15. Cerutti, F. *et al.* Urgent need of rapid tests for SARS CoV-2 antigen detection: Evaluation of the SD-Biosensor antigen test for SARS-CoV-2. *J. Clin. Virol.* **132**, 104654 (2020).
16. Mak, G. C. *et al.* Evaluation of rapid antigen test for detection of SARS-CoV-2 virus. *J. Clin. Virol.* **129**, 104500 (2020).
17. Walls, A. C. *et al.* Structure, Function, and Antigenicity of the SARS-CoV-2 Spike Glycoprotein. *Cell* **181**, 281-292.e6 (2020).
18. Zhang, Y. Z. & Holmes, E. C. A Genomic Perspective on the Origin and Emergence of SARS-CoV-2. *Cell* **181**, 223–227 (2020).
19. McCallum, M. *et al.* N-terminal domain antigenic mapping reveals a site of vulnerability for SARS-CoV-2. *Cell* 1–16 (2021) doi:10.1016/j.cell.2021.03.028.
20. Piccoli, L. *et al.* Mapping Neutralizing and Immunodominant Sites on the SARS-CoV-2 Spike Receptor-Binding Domain by Structure-Guided High-Resolution Serology. *Cell* **183**, 1024-1042.e21 (2020).

21. Tortorici, M. A. *et al.* Ultrapotent human antibodies protect against SARS-CoV-2 challenge via multiple mechanisms. *Science* **370**, 950–957 (2020).
22. Baden, L. R. *et al.* Efficacy and Safety of the mRNA-1273 SARS-CoV-2 Vaccine. *N. Engl. J. Med.* **384**, 403–416 (2021).
23. Jackson, L. A. *et al.* An mRNA Vaccine against SARS-CoV-2 — Preliminary Report. *N. Engl. J. Med.* **383**, 1920–1931 (2020).
24. Li, F. Structure, Function, and Evolution of Coronavirus Spike Proteins. *Annu. Rev. Virol.* **3**, 237–261 (2016).
25. Tortorici, M. A. & Veesler, D. Structural insights into coronavirus entry. *Adv. Virus Res.* **105**, 93–116 (2019).
26. Bunka, D. H. J. & Stockley, P. G. Aptamers come of age - At last. *Nat. Rev. Microbiol.* **4**, 588–596 (2006).
27. I. Hernandez, L., Machado, I., Schafer, T. & J. Hernandez, F. Aptamers Overview: Selection, Features and Applications. *Curr. Top. Med. Chem.* **15**, 1066–1081 (2015).
28. Aptamers as targeted therapeutics: current potential and challenges | Nature Reviews Drug Discovery. https://www.nature.com/articles/nrd.2016.199.
29. Nimjee, S. M., Rusconi, C. P. & Sullenger, B. A. Aptamers: An emerging class of therapeutics. *Annu. Rev. Med.* **56**, 555–583 (2005).
30. Tombelli, S., Minunni, M. & Mascini, M. Analytical applications of aptamers. *Biosens. Bioelectron.* **20**, 2424–2434 (2005).
31. Keefe, A. D., Pai, S. & Ellington, A. Aptamers as therapeutics. *Nat. Rev. Drug Discov.* **9**, 537–550 (2010).
32. Kacherovsky, N. *et al.* Traceless aptamer-mediated isolation of CD8+ T cells for chimeric antigen receptor T-cell therapy. *Nat. Biomed. Eng.* **3**, 783–795 (2019).

33. Robertson, D. L. & Joyce, G. F. Selection in vitro of an RNA enzyme that specifically cleaves single-stranded DNA. *Lett. Nat.* **344**, 467–468 (1990).

34. Tuerk, C. & Gold, L. Systematic evolution of ligands by exponential enrichment: RNA ligands to bacteriophage T4 DNA polymerase. *Science* **249**, 505–510 (1990).

35. Ellington, A. D. & Szostak, J. W. In vitro selection of RNA molecules that bind specific ligands. *Nature* **346**, 818–822 (1990).

36. Jarczewska, M., Rębiś, J., Górski, Ł. & Malinowska, E. Development of DNA aptamer-based sensor for electrochemical detection of C-reactive protein. *Talanta* **189**, 45–54 (2018).

37. Liu, J. *et al.* Recent Developments in Protein and Cell-Targeted Aptamer Selection and Applications. *Curr. Med. Chem.* **18**, 4117–4125 (2011).

38. Galloway, S. E. *et al.* Emergence of SARS-CoV-2 B.1.1.7 Lineage — United States, December 29, 2020–January 12, 2021. *MMWR Morb. Mortal. Wkly. Rep.* **70**, 95–99 (2021).

39. Harvey, W. T. *et al.* SARS-CoV-2 variants, spike mutations and immune escape. *Nat. Rev. Microbiol.* **19**, 409–424 (2021).

40. McCallum, M. *et al.* SARS-CoV-2 immune evasion by the B.1.427/B.1.429 variant of concern. *Science* eabi7994 (2021) doi:10.1126/science.abi7994.

41. Graham, C. *et al. Impact of the B.1.1.7 variant on neutralizing monoclonal antibodies recognizing diverse epitopes on SARS–CoV–2 Spike*. http://biorxiv.org/lookup/doi/10.1101/2021.02.03.429355 (2021) doi:10.1101/2021.02.03.429355.

42. Meng, B. *et al.* Recurrent emergence of SARS-CoV-2 spike deletion H69/V70 and its role in the Alpha variant B.1.1.7. *Cell Rep.* **35**, 109292 (2021).

43. Ascoli, C. A. Could mutations of SARS-CoV-2 suppress diagnostic detection? *Nat. Biotechnol.* **39**, 274–275 (2021).

44. Jain, A. *et al.* Analysis of the potential impact of genomic variants in global SARS-CoV-2 genomes on molecular diagnostic assays. *Int. J. Infect. Dis.* **102**, 460–462 (2021).

45. Yang, J.-R. *et al.* Newly Emerging Mutations in the Matrix Genes of the Human Influenza A(H1N1)pdm09 and A(H3N2) Viruses Reduce the Detection Sensitivity of Real-Time Reverse Transcription-PCR. *J. Clin. Microbiol.* **52**, 76–82 (2014).

46. Jongerius, J. *et al.* New hepatitis B virus mutant form in a blood donor that is undetectable in several hepatitis B surface antigen screening assays. *Transfusion (Paris)* **38**, 56–59 (1998).

47. Meredith, L. W. *et al.* Rapid implementation of SARS-CoV-2 sequencing to investigate cases of health-care associated COVID-19: a prospective genomic surveillance study. *Lancet Infect. Dis.* **20**, 1263–1271 (2020).

48. Clark, A. *et al.* Global, regional, and national estimates of the population at increased risk of severe COVID-19 due to underlying health conditions in 2020: a modelling study. *Lancet Glob. Health* **8**, e1003–e1017 (2020).

49. ERA-EDTA Council & ERACODA Working Group. Chronic kidney disease is a key risk factor for severe COVID-19: a call to action by the ERA-EDTA. *Nephrol. Dial. Transplant.* **36**, 87–94 (2021).

50. Henry, B. M. & Lippi, G. Chronic kidney disease is associated with severe coronavirus disease 2019 (COVID-19) infection. *Int. Urol. Nephrol.* **52**, 1193–1194 (2020).

51. Johansen, K. L. *et al.* US Renal Data System 2020 Annual Data Report: Epidemiology of Kidney Disease in the United States. *Am. J. Kidney Dis.* **77**, A7–A8 (2021).
52. Kalantar-Zadeh, K., Jafar, T. H., Nitsch, D., Neuen, B. L. & Perkovic, V. Chronic kidney disease. *The Lancet* (2021) doi:10.1016/S0140-6736(21)00519-5.
53. Carney, E. F. The impact of chronic kidney disease on global health. *Nat. Rev. Nephrol.* **16**, 251–251 (2020).
54. Huang, S. & Susztak, K. Epithelial Plasticity versus EMT in Kidney Fibrosis. *Trends Mol. Med.* **22**, 4–6 (2016).
55. Lovisa, S., Zeisberg, M. & Kalluri, R. Partial Epithelial-to-Mesenchymal Transition and Other New Mechanisms of Kidney Fibrosis. *Trends Endocrinol. Metab.* **27**, 681–695 (2016).
56. Qi, R. & Yang, C. Renal tubular epithelial cells: the neglected mediator of tubulointerstitial fibrosis after injury. *Cell Death Dis.* **9**, (2018).
57. Grande, M. T. *et al.* Snail1-induced partial epithelial-to-mesenchymal transition drives renal fibrosis in mice and can be targeted to reverse established disease. *Nat. Med.* **21**, 989–997 (2015).
58. Bai, Q. *et al.* Epigallocatechin-3-gallate promotes angiogenesis via up-regulation of Nfr2 signaling pathway in a mouse model of ischemic stroke. *Behav. Brain Res.* **321**, 79–86 (2017).
59. Bose, M. *et al.* The Major Green Tea Polyphenol, (-)-Epigallocatechin-3-Gallate, Inhibits Obesity, Metabolic Syndrome, and Fatty Liver Disease in High-Fat–Fed Mice. *J. Nutr.* **138**, 1677–1683 (2008).

60. Chen, J.-H. *et al.* Green tea polyphenols prevent toxin-induced hepatotoxicity in mice by down-regulating inducible nitric oxide–derived prooxidants. *Am. J. Clin. Nutr.* **80**, 742–751 (2004).
61. Chyu, K.-Y. *et al.* Differential Effects of Green Tea–Derived Catechin on Developing Versus Established Atherosclerosis in Apolipoprotein E–Null Mice. *Circulation* **109**, 2448–2453 (2004).
62. Rezai-Zadeh, K. *et al.* Green tea epigallocatechin-3-gallate (EGCG) reduces β-amyloid mediated cognitive impairment and modulates tau pathology in Alzheimer transgenic mice. *Brain Res.* **1214**, 177–187 (2008).
63. Rezai-Zadeh, K. *et al.* Green Tea Epigallocatechin-3-Gallate (EGCG) Modulates Amyloid Precursor Protein Cleavage and Reduces Cerebral Amyloidosis in Alzheimer Transgenic Mice. *J. Neurosci.* **25**, 8807–8814 (2005).
64. Tipoe, G. L. *et al.* Epigallocatechin-3-gallate (EGCG) reduces liver inflammation, oxidative stress and fibrosis in carbon tetrachloride (CCl4)-induced liver injury in mice. *Toxicology* **273**, 45–52 (2010).
65. Kanlaya, R. *et al.* Epigallocatechin-3-gallate prevents TGF-β1-induced epithelial-mesenchymal transition and fibrotic changes of renal cells via GSK-3β/β-catenin/Snail1 and Nrf2 pathways. *J. Nutr. Biochem.* **76**, 108266–108266 (2020).
66. Liu, G. W. *et al.* Glomerular disease augments kidney accumulation of synthetic anionic polymers. *Biomaterials* **178**, 317–325 (2018).
67. Boronic Acid Copolymers for Direct Loading and Acid-Triggered Release of Bis-T-23 in Cultured Podocytes | ACS Biomaterials Science & Engineering. https://pubs.acs.org/doi/10.1021/acsbiomaterials.8b01163.

Introduction

Aptamer discovery, characterization, and *in vitro* applications: a modern foundation

Adapted from draft of Invited Review for Chemical Science

Lucy F. Yang

Introduction

Aptamers are nucleic acid molecular recognition agents that specifically bind to targets like proteins, drugs, peptides, metal ions, and more. Aptamers are typically single-stranded, short (10^1 ~10^2 nt) DNA or RNA strands that fold into secondary structures and adopt conformations that allow binding to targets. Most aptamers are discovered through an *in vitro* library selection process called systematic evolution of ligands by exponential enrichment (SELEX), which uses a desired target to enrich for binders among many random sequences. Utilized in research fields from biosensing to therapeutics, aptamers have versatile applications but have yet to reach their full potential.

One hurdle in aptamer development is the similarity in use-cases between aptamers to antibodies (Table 1). Both aptamers and antibodies can have very high affinity (low picomolar) and specificity (single AA point mutation sensitivity) for their targets. However, aptamers unlike antibodies, are chemically synthesized and thus are less expensive and faster to produce, very homogenous with minimal batch-to-batch variation, and easier to chemically modify with control. Moreover, DNA aptamers are more stable at a range of ionic conditions, pH, temperatures, and other storage conditions compared to protein antibodies. Despite these advantages, aptamers currently lag behind in diversity of discovered sequences because most are artificially selected for via SELEX, which and not easily isolated from natural selection methods like antibodies.

Table 1. Aptamers vs antibodies.

		Aptamer	**Antibody**
Intrinsic Qualities	**Affinity**	1 pM ~ 10 uM	1 pM ~ 10 uM
	Specificity	Highly specific	Highly specific
	Molecular Weight	10~20 kDa	150 kDa (IgG)
	Synthesis Method	Chemical	Biological
	Stability	pH 5 ~ 9 -80 ~ 100^{o}C liquid or dry	pH 5 ~ 8, sequence specific, empirically determined -80 ~ 4^{o}C requires trehalose for dry
Application-related Qualities	**Selection Speed**	days ~ weeks *in vitro*	weeks *in vivo*
	Variability	very uniform	batch to batch
	Cost of 1 mg from Commercial Vendor	~$50	~$2000-5000
	Chemical Modifications	5’ end, 3’ end, internal; controlled	Primary amine, carboxylic acid, thiol

			chemistries; difficult to control
	Elution Method	complementary strand	pH, ions, denaturants

Preceding aptamer research as we know today, the discovery of RNA enzymes in the 1980s kickstarted interest in nucleic acids that could fold into complex structures and catalyze reactions[1–4]. Then, in 1990, three research groups independently described iterative *in vitro* selection methods for RNA enzymes[5–7], which Tuerk and Gold coined SELEX[6]. Ellington and Szostak expanded on the previous work and named the nucleic acids that were output of selections “aptamers”: ‘apta’ from *aptus* meaning ‘fitting’ in Latin[8]. Many other major milestones in aptamer history occurred in quick succession: In 1992, the first DNA aptamers, thrombin-binding aptamer and specific dye-binding aptamers, were discovered[9,10]. The first aptamers isolated by cell SELEX were reported in 1999 and bound to the parasite *Trypanosoma brucei*[11]. In 2004, the first aptamer therapeutic drug, Macugen, was approved by the FDA to treat macular degeneration[12]. Over time, technical advancements in DNA manipulation and sequencing, as well as new developments in selection strategies, have streamlined the selection progress and lowered the barrier to entry. However, the core of idea behind SELEX remains unchanged for over 30 years.

In this introduction, I will first describe aptamer selection and optimization strategies. Then I will examine biomedical applications of aptamers in *in vitro* settings such as biosensing and partitioning. Overall, this will prepare readers for entering the world of aptamers as it stands today, especially in light of the COVID-19 pandemic.

Aptamer Sequence Discovery & Optimization

SELEX is the heart of aptamer research because it is the primary method for discovering new aptamer sequences. In SELEX, a starting library is incubated with desired targets, such as cells or proteins. Then bound sequences are recovered and PCR amplified to create a new pool of aptamer sequences, which can then be selected against the targets again. This cycle is one round of selection, and typically 5-20 rounds are necessary to enrich the aptamer pool to find target-binding aptamers. In this section, we will review basic concepts, considerations, and techniques of SELEX.

Starting library selection

Although early aptamer research focused on RNA aptamers, the majority of recently discovered and applied aptamers are DNA-based. DNA as compared to RNA is more stable, has a more streamlined process for replication[15,19], and has a similar capability to form secondary and tertiary structures.

Aptamer libraries typically consist of a random region flanked by two constant regions, which are used to amplify the aptamer with primers that are complementary to the constant regions. One concern is that the constant regions are not precluded from binding participation. A study conducted in 2008 found that most aptamers do not require their constant regions for binding[20], possibly due to primers requiring access to the constant regions for efficient amplification[19]. On the other hand, the random region is theoretically unique for each aptamer in a starting library. The longer the random region, the more candidate sequences. For example, a 40-nt random region would be 4^{40} or ~10^{24} unique sequences, which would weigh ~50 kg. Practically speaking, selection libraries are used on the order of 1 nmol for the initial round of selection, so typically 10^{14} ~10^{18} unique sequences are tested[21–23]. The choice for random region length may influence SELEX success, but aptamers have been discovered in libraries with random regions as large as 220-nt and as short as 22-nt[21].

One study compared the effect of six different random region lengths (16, 22, 26, 50, 70, 90) on target-binding sequence abundance and found that the target motif was most abundant in the 50-nt and 70-nt selections[24]. In recent publications, a random region of 36 to 52 nt in length have been the most common, which is about 70~90 nt in total aptamer length. DNA synthesis costs also play a factor, as longer syntheses become more expensive and less efficient. For example, if the efficiency of adding a nucleotide base is 99.5%, an 80-mer aptamer is produced with 69% yield but a 160-mer aptamer is produced at 45% yield.

Pre-structured libraries are one strategy for increasing the probability of enriching for binding aptamers. One library stabilizes the aptamer structure via C-G bonds in the constant region, allowing the random region's 5' and 3' end to meet. This predictable final structure also simplifies aptamer truncation designs[25]. Another library contains more guanidine bases to increase the probability of G quadruplexes[26], which are stable secondary structures formed by stacks of four guanidine units. Aside from their intriguing structure, G quadruplexes are of interest because they have important functions in DNA replication and repair, epigenetics, and other pivotal cellular processes[27]. G quadruplexes are also often found in high-affinity aptamers[28,29], therefore increasing their frequency in the starting library may lead to higher chances of success.

Non-natural or chemically-modified nucleic acids are also one way to increase aptamer library diversity, access potentially unreachable binding epitopes available on proteins, and improve binding affinities.[30] In one recent work, McCloskey et. al. used alpha-l-threofuranosyl nucleic acid (TNA) to make backbone- and base-altered aptamers capable of undergoing *in vitro* selection and binding target proteins.[31] These TNA aptamers contain traditional bases as well as modified bases containing phenylalanine and tryptophan, which are planar aromatic amino acids often found at the antibody-antigen interface. From TNA libraries with ~10^{14} unique instances of 40-nt random region, McCloskey et. al. enriched for threomers that bind SARS-CoV-2 S1 protein or TNFα, many with nanomolar affinities and sub-nanomolar affinities after optimization. However, some drawbacks include the need for lengthy chemical synthesis (14 to 29 steps per TNA nucleoside triphosphate) and optimization of TNA polymerases. Similarly, the "click-SELEX" strategy uses alkyne-modified uridine (EdU) that are functioned by azide-modified groups.[32] Unlike with TNAs, EdU is commercially available and therefore click-PCR can be performed using conventional PCR and enzymes. Another perk of click-SELEX is choosing an azide that contains a group also found on the target's natural binders in order to improve binding probability.

Another non-natural strategy is the use mirror image aptamers made from L-RNA or L-DNA, which are called spiegelmers[33]. Unrecognized by nucleases and DNA processing enzymes, spiegelmers are more stable *in vivo* but also are not easy to PCR amplify in selection. To circumvent the amplification problem, Vater et. al. conducted SELEX with the enantiomer of the target peptide and D-RNA then synthesized the spiegelmers based on the discovered D-RNA sequence.[34]

Selection targets

Incipient aptamer research identified binders of dyes on agarose beads, but today aptamer binding targets have expanded to include metal ions, small molecules, peptides, proteins, bacteria, human cells, and more.

A plethora of cell types have been used as selection targets[35], including cancer cells[29,36,37], T cells[23], and bacteria[38]. The protocol for cell SELEX is straightforward to perform and does not require many specialized tools.[39] Cells are easily to partition by centrifugation, leaving unbound aptamers in suspension while bound aptamers remain on the pelleted cells. The aptamers on cells are eluted off heating then centrifugation. Aside from its protocol simplicity, cell SELEX is advantageous because of its authentic target presentation on the cell surface and large variety of potential targets conducted in one process.[35] However, some challenges of cell SELEX include temperature and receptor identification. The SELEX must be conducted at 4°C to avoid aptamer internalization via phagocytosis, which would non-specifically remove candidates from the pool. Consequentially, aptamers discovered are optimized for performance at 4°C, and may not reflect its binding properties at room temperature or 37°C. The other major hurdle is identifying the aptamer binding target, which is usually a membrane protein. Co-staining or competitive binding studies are one way to elucidate which target the aptamer binds to. For example, Kacherovsky et. al. co-stained T cells with fluorescently-labeled aptamer and fluorescently-labeled antibody in order to determine the aptamer target as CD8 protein by flow cytometry[23]. However, this screening is potentially cost- and time-intensive if there are multiple potential targets and educated guesses are mistaken. Another technique is a target pull-down assay, where proteins in target cell lysate are pulled down by the aptamer and run on an SDS-PAGE gel. Then, the bands that more enriched in the aptamer pull-down samples compared to control samples are excised for further analysis by mass spectrometry. Lin et. al. identified fibronectin as a potential target for their glioma-targeting aptamer S6-1b by liquid chromatography with tandem mass spectrometry (LC-MS/MS).[37] Overall, there are limited success stories for receptor identification after cell SELEX and new strategies are needed for receptor identification.

Another prevalent selection target is purified protein. Unlike cell selection, no receptor identification step is needed. In fact, further studies, such as protein binding studies and cyro-EM[25], can precisely identify the binding epitope. However, the presentation of the protein may not be faithful to its native conformation, which may lead to aptamers that perform well in protein binding studies but not in its application. To circumvent this, hybrid cell and protein SELEX has been a successful approach. Pioneering this strategy, Hicke et. al. used tumor cells then protein for selecting aptamers against tenascin-C, a protein implicated in tumor growth.[36] Recent examples include C42-aptamer[40], which targets human programmed cell death protein 1 and was found after 13 rounds of protein then 3 rounds of cell SELEX, and SNAP4[41], which targets SARS-CoV-2 spike protein and was found after 6 rounds of cell then 4 rounds of protein SELEX. Using multiple protein targets within the same SELEX can also yield high affinity aptamers. Zhang et. al. completed 13 selection rounds with wild-type SARS-CoV-2 S1, but then conducted 5 separate selection rounds using different variants of SARS-CoV-2 S protein.[42]

Another issue with protein SELEX is that typically embedded or inward-facing portions of membrane proteins are exposed during selection, allowing aptamers to bind to an inaccessible location in the native state. One emerging technique that circumvents this issue as well as the issue of receptor identification in cell SELEX is “viro-SELEX”. The target membrane proteins are expressed on the viral envelope of a surrogate baculovirus, allowing native conformation expression. Via protein and viro-SELEX, Narayan et. al. isolated aptamers specifically binding the hemagglutinin (HA) protein of H1N1 influenza virus.[43]

Other than a positive selection target, negative selection or counter-selection is a common strategy to reduce enrichment of non-specific binders. During a round of selection, the aptamer pool is incubated with an undesired target, and those binders are depleted from the pool. For example, an aptamer library could be incubated with an off-target cell line, then after centrifugation the non-binding sequences in the supernatant are used in positive selection within the same round.

Partitioning bound and unbound aptamers

Separating binding and non-binding aptamers during selection is a key component of SELEX. With cell SELEX, the partitioning is conveniently performed by centrifugation. For protein SELEX, libraries are typically partitioned by two major methods. One method is capillary electrophoresis SELEX (CE-SELEX), which separates free aptamer, protein, and aptamer-protein complexes from each other due to varying electrophoretic mobility constants. CE-SELEX was first developed in 2004[44], and many variations exist today for improving certain aspects of the process: Single step CE-SELEX (ssCE-SELEX) streamlines the selection in a single run to save time and materials[45]; fraction collection CE-SELEX (FCE-SELEX) reduces contamination by loading directly into oil-sealed PCR mixtures[46]; and ideal-filter capillary electrophoresis (IFCE) tunes the ionic strength of the running buffer to migrate non-binding nucleotides in the opposite direction of nucleoprotein complexes, dramatically increasing the efficiency of separation by eliminating carry-over of non-binding aptamers[47]. Overall, CE-SELEX offers tunable, quantifiable partitioning, but is limited by several factors. CE-SELEX can only process a small volume, which limits the library size and diversity sampled. CE-SELEX also requires size and charge differences between the aptamer and its target in order to be separated, and this is challenging for small molecules and membrane proteins. Another approach for protein SELEX is immobilization of protein onto magnetic spheres for magnetic separation. This technique was first pioneered in 2005 as a less wasteful alternative to immobilization on columns,[48] and today many

SELEX strategies use magnetic spheres. Polyhistidine tags (His-Tag) on proteins are immobilized onto nickel-nitriloacetic acid (Ni-NTA) or cobalt-based magnetic spheres [22,25,49]. Since this method only requires cheap, commercially available components like magnetic spheres and magnetic rack, protein SELEX with magnetic spheres is very accessible. Some drawbacks of magnetic selection include labor-intensive manual pipetting and dead volume during washing that may carry over non-binding aptamers. Other less frequently used methods also exist, such as repurposing surface plasmon resonance (SPR) chips[50,51] and biolayer interferometry (BLI) biosensors[52,53] for selection.

Recently, more efficient and accurate separation have emerged to improve the affinity and specificity of final aptamer candidates.[54] One of these strategies is particle display, where emulsion PCR allows amplification and immobilization of each unique aptamer sequence to a particle, which is easily analyzed and collected by fluorescence-activated cell sorting (FACS).[55] This technology also enables simultaneous screening for both affinity and specificity by labeling target and non-target, respectively, with different fluorescent colors.

Altogether, aptamer researchers today can choose from a diverse cast of SELEX targets and partitioning methods, not to mention combinations of multiple approaches and emerging techniques.

Secondary library preparation (PCR & strand separation)

After collecting aptamers that bind the target, it’s necessary to amplify the pool and isolate the positive sense strand for further selection or binding analysis. The most common method for library preparation is PCR using a labeled reverse strand for pulldown. For example, PCR is conducted with a reverse primer with 3’ biotin label.

Then, the PCR product is bound to streptavidin agarose then flushed, breaking base pair bonds and eluting the positive sense strand. The remaining biotinylated nucleotides are eluted from the agarose by sodium hydroxide.[39] Because the components required are commercially available and inexpensive, the biotin pulldown method is very effective for new SELEX set-ups. Another method uses lambda nuclease, which preferentially digests DNA with 5' phosphorylation.[56] So, specific digestion of the negative sense strand can be performed if 5' phosphorylated reverse primer is used to amplify the aptamer library. A third method for library preparation is asymmetric PCR. Forward and reverse primers are used in unequal molar ratios in order to preferentially amplify the sense strand. Then, the PCR product is separated by gel electrophoresis and ssDNA is eluted from the gel in a labor-intensive, low-yield process.

Improving and evaluating library binding

Once a cycle of SELEX is completed, the resulting library can be used in another round of SELEX and evaluated for binding and sequences.

For each selection iteration, "knobs" can be adjusted to tune the stringency and desired results. For example, the stringency can be increased through: a decrease of aptamer library concentration; a decrease incubation time or concentration of target; addition or increased concentration of competitors, such as bovine serum albumin (BSA), yeast tRNA, and salmon sperm DNA; addition or increased concentration of surfactants, such as Tween-20 and dextran sulfate; an increase in wash steps; addition or increased concentration of counterselection target; a change in target, for instance to a smaller portion of the target protein or alternative cell line. Generally, these selection conditions are empirically determined. If conditions are too stringent, the amplification of the aptamer pool could be unviable or take a large number of PCR cycles. If conditions were too relaxed, the number of PCR cycles may be very small and successive pools may not increase binding signal. Because the first round of selection contains only unique aptamers, it is better to start with gentle conditions to avoid loss of potential binding candidates.

The aptamer library can also be evaluated for binding. Before modern methods, radioactive isotopes were used to label aptamers for binding studies. Today, many SELEX protocols use labeled forward primers to amplify sense strands for binding assays, such as FITC[57] or Cy5[22] fluorescent dyes. Thanks to these tags, apparent K_D binding can be measured by methods like cell flow cytometry[41,49], dot blot assay[42], and direct ELISAs[41,58]. Techniques that directly measure binding kinetics include surface plasmon resonance (SPR)[22,59] and biolayer interferometry (BLI)[25,41].

Binding assessment is important for adjusting the SELEX strategy if no binding is observed and choosing when to stop SELEX and sequence the libraries. However, amplification of aptamer library to conduct binding studies requires significant time and materials investment, which can be more effectively spent on performing more SELEX rounds.

Lastly, the aptamer library can be sequenced in order to retrieve aptamer sequences for further characterization. Next generation sequencing (NGS) is the primary tool for sequencing because it is commercially available, requires very little aptamer library relative to binding studies, and accurately outputs sequences. In NGS, the nucleotides are immobilized onto a surface, then cyclically extended with a nucleotide labeled with fluorescent dye and imaged to record the nucleotide identity.[60] The data can be filtered to only include sequences containing the constant region and known length of random region. The previously mentioned techniques for assessing aptamer library binding are also used to evaluate individual sequence binding.

Other Considerations

Typically, SELEX is conducted by manual pipetting, but microfluidic and computational approaches are under investigation for automating the process. Initially prototyped in 2006[61], microfluidic SELEX platforms can precisely control fluids and temperature in order to mix, incubate, and partition SELEX reagents from aptamer library introduction to secondary library generation. Several microfluidic systems that automate part of the SELEX process have been proposed[62], including systems that utilize magnetic particles or a class of molecularly imprinted polymers (MIPs) called sol-gel. Recently, Sinha et. al. developed a microfluidic system capable of automating most of the process on-chip (negative selection, positive selection, PCR, competitive assay).[63] Despite these advances, microfluidic SELEX requires substantial technical know-how and investment to set up, such as master molds for pouring polydimethylsiloxane (PDMS) and controllers for air valves and temperature regulation. In contrast, traditional SELEX uses tools readily available in most molecular biology labs (thermocycler, magnetic rack, etc.) Therefore additional investigation is needed to commercialize the technology and disseminate it.

Computational approaches to SELEX have also been investigated. *In silico* design can save time and reagents by performing computational simulations instead of tedious benchwork. This concept has been readily applied to *de novo* protein switches and biosenors[64,65]. In addition, *in silico* SELEX can circumvent some inherent flaws in the process, such as avoiding the amplification of sequences that are preferentially PCR amplified or transcribed[66]. Computationally-aided[67] and combined computation and high-throughput array SELEX schematics[55] have been recently conducted. However, *in silico* methods are hampered by the difficulties in accurately predicting aptamer structure, especially as current tools can only predict 3D RNA structures.

In vitro Applications

Aptamers are being applied to biomedical problems in a multitude of use cases, from sensitive drug detection to being a drug itself. Here, we focus on recent *in vitro* applications in two main sections: biosensing and partitioning.

Biosensing

Biosensors are systems that take biological inputs and output electrical, electrochemical, or optical signals indicating detection or absence of an analyte. Biosensors function by using both biological recognition agents to recognize the analyte as well as transducers to for signal readout.[68] Biosensors typically produce results quickly (on the order of minutes to hours), in real-time, and sometimes continuously. Many biosensors are also easy to operate and inexpensive to produce, increasing the accessibility of the device. These key properties make biosensors suitable for applications such as point-of-care rapid diagnostics of diseases and monitoring of biomolecules in the environment.

Not only are aptamers capable of molecular recognition like antibodies, but also they are smaller in size, easier to chemically modify, and robust across various sample conditions. These properties uniquely position aptamers as the recognition agent of choice in biosensing. A compact size is essential to decrease the distance between an electrode and the binding event, allowing for sensitive detection of electrochemical signal changes. Addition of functional groups and molecules onto nucleic acids is more straightforward and controlled, and therefore less polydisperse and more consistent, than chemistries conducted on protein antibodies. Lastly, aptamers can withstand washing and reuse unlike antibodies, allowing for repeated measurements on the same device.

Thanks to the aforementioned advantages, aptamers have been used in biosensors across many fields of study, including microfluidics. Lab-on-a-chip systems featuring aptamers have been thoroughly reviewed recently[69], so we will focus our topics on basic examples split by detection method.

Electrochemical

Electrochemical aptamer-based (E-AB) sensors are one type of label-free biosensor that employs conformational change of the aptamer upon binding to produce an electrical signal change. Typically, E-ABs require 3 electrodes, one of which is the aptamer-modified gold working electrode. A region of the aptamer containing redox reactive molecules, such as methylene blue or ferrocene, moves relative to the electrode after target binding. A “signal-on” E-AB produces the signal after binding, while a “signal-off” E-AB interrupts the signal after binding. The electrical signal change can be a change in potential, current, or impedance depending on the set up.[70,71] Potential for high sensitivity, label- and sample processing-free prep, real-time detection of signal, and reusability give E-ABs distinct advantages over other options, such as qPCR, ELISA, and LFAs.

One of the most-cited E-AB platforms is a thrombin-detecting “signal-off” E-AB from the Plaxco research group.[72] Aptamer was conjugated to the gold working electrode surface via its 5’ thiol group, then the electrode was passivated with 6-mercaptohexanol. In combination with a counter electrode and reference electrode, the sensor detected electron transfer from the methylene blue on the 3’ end of the aptamer to the working electrode in the absence of thrombin. When the aptamer bound thrombin, its new conformation presumably shifted the methylene blue away from the electrode, reducing electron transfer and signal. This thrombin E-AB demonstrated rapid detection, nanomolar sensitivity, and reusability, igniting further research into E-ABs. Today, research groups have developed different electrode set ups and detection schemes, as well as expanded the menu of analytes, which now includes small molecule drugs (cocaine[73], ampicilin[74]), proteins (CRP[75], insulin[76]), and viruses (zika virus[77], avian flu[78], SARS-CoV-2[79,80]).

Two recent publications describe low-cost E-AB for detection of SARS-CoV-2. Lasserre et. al. conjugated SARS-CoV-2 spike protein-binding aptamers to a thin-film gold electrode (TFGE), which are the same electrodes used in blood glucose test strips[79]. The sensor was first incubated with the sample, then measured by electrochemical impedance spectroscopy (EIS) in buffer containing ferri/ferrocyanide. Aptamer binding of target reduces the charge transfer of the ferri/ferrocyanide to the electrode, increasing impedance. The system detected 80 ng/mL (~ 1 nM) of SARS-CoV-2 S1 protein and distinguished between SARS-CoV-2 positive and negative clinical samples. In a different report, Martínez-Roque et. al. described a E-AB that uses two non-competing aptamers to detect spike protein with sub-femtomolar sensitivity[53]. The gold electrode was functionalized with aptamer-thiol then PEG-thiol, and measurements were taken by differential pulse voltammetry (DPV) in ferri/ferrocyanide solution. When aptamer captures the spike protein and changes conformation, the ferrocyanide charge transfer is reduced and the change in current normalized to initial current increases. A dynamic range of 0.007 to ~700 fM was obtained, with a K_D of 1.04 fM.

Another recently reported E-AB system showed highly sensitive detection of luteinizing hormone (LH) in patient samples.[81] In order to overcome steric hinderance at the electrode interface by large analyte molecules, Li et. al. used additional DNA probes to indirectly measure aptamer-target binding in solution. When the analyte is absent from the solution, the aptamer and signal probe hybridize, producing no signal on the working electrode. In the presence of analyte, the more stable aptamer-analyte interaction outcompetes the aptamer-signal probe bond, releasing free signal probes in solution. The signal probes then hybridize with helper probes bonded to the electrode surface. The electroactive methylene blue on the signal probe facilitates electron transfer, which is measured by square wave voltammetry (SWV). This strategy was coined “biphasic replacement” E-AB (BRE-AB). Li et. al. demonstrate picomolar LOD of LH protein even in 50% whole blood, no significant loss in signal after 5 regeneration-reuse cycles, and stable storage over 21 days at 4^{o}C. Lastly, BRE-AB quantified LH concentrations in clinical blood samples and found a significant difference between female healthy and breast cancer samples. Overall, BRE-AB demonstrates the key advantages aptamers provide in E-ABs: rapid results without sample processing, storage stability, and reusability.

Recent innovations in E-AB include investigation of paper electrochemical devices (PEDs), which are lower cost to fabricate, less sophisticated to use, and more disposable than other sensing platforms. Yu et. al. fabricated PEDs using simple materials (filter paper, single-walled carbon nanotubes, and metal nanoparticles) and machines (vacuum filtration glassware, thermal laminator, and paper cutter)[82]. After immobilization with aptamer, the PEDs detected cocaine and methylenedioxypyrovalerone (MDPV) by alternating current voltammetry at similar detection limits as conventional E-ABs. The researchers also detected cocaine and MDPV at lower sensitivities in various complex buffers, such as 50% saliva and 50% urine. Another recent publication from the same group showcased an aptamer-modified multiplex PED (mPED). Fabricated in a similar method as the PEDs from Yu et. al., the mPEDs contained three working electrodes, which can each be functionalized with a different aptamer.[83] When mPEDs were immobilized with AF-32, MDPV-34, and ADE-25 aptamers on electrodes 1-3 respectively, Liu et. al. measured micromolar concentrations of acetyl fentanyl, MDPV, and adenosine, respectively, on electrode 1-3, in any combination. The mPEDs also detected analytes in 50% saliva and 50% urine at about 2-5-fold lower sensitivities, and with a PDMS containment chamber for precious samples. Overall, these aptamer PEDs demonstrate great potential as a cost-effective, easily manufactured point-of-care detection device.

The urgent need for rapid SARS-CoV-2 diagnostics during the pandemic accelerated development of novel E-AB sensor schemes. Also a paper-based biosensor, the SARS-CoV-2 biosensor chip developed by Alafeef et. al. used anti-sense oligonucleotides-conjugated gold nanoparticles to detect viral nucleocapsid gene.[84] The sensor was constructed from graphene, filter paper, and a homemade circuit that is simpler than conventional techniques. The sensor achieved extraordinary sensitivity without amplification (limit of detection of 6.9 copies/uL) and distinguished between 48 positive and negative patient samples with 100% accuracy and specificity. One drawback of this method is need for RNA extraction and the lack of aptamers. However, the system demonstrate the great potential it could have by substituting the anti-sense oligonucleotides for aptamers.

In another recent report, Ban et. al. recently reported a DNA aptamer-conjugated graphene field-effect transistor (GFET) platform for detecting SARS-CoV-2 proteins and intact inactivated virus[85]. PBASE-functionalized GFETs were immobilized with amine-modified aptamers, baselined, incubated with sample, washed, and measured. Baseline and measurements were taken by performing voltage sweeps to calculate the Dirac voltage, which quantifies the relative charge on the GFET surface. An increase in the Dirac voltage reflected an increase in binding of analyte to aptamers. Functionalized with spike (S)- or nucleocapsid (N)-targeting aptamers, the GFETs could detect sub-nanomolar concentrations of SARS-CoV-2 S or N protein, respectively. Additionally, the aptamer-functionalized GFET detected Delta variant heat-inactivated SARS-CoV-2 with estimated limits of detection (LODs) 1.28 PFU/mL for S and 1.45 PFU/mL and N protein. Lastly, aptamer-functionalized GFETs were able to accurately distinguish between 10 positive and negative wild-type SARS-CoV-2 patient samples with no misclassifications after determining threshold with 20 samples. A similar result was achieved for Delta/Omicron samples. Overall, the aptamer-functionalized GFET shows great promise in becoming a point-of-care rapid diagnostic test.

A different group reported an E-AB for detecting SARS-CoV-2 virus using a dual recognition strategy using both aptamers and molecular imprinting polymers (MIPs).[86] MIPs provide a cavity for virus binding as well as high durability, chemical stability, and thermal stability. To increase surface area and biocompatibility, Rahmati et. al. also incorporated metal-organic frameworks (MOFs), which are hybrid materials characterized by their porous crystalline structure and diverse compositions. The biosensor was synthesized by modifying screen printed carbon electrodes (SPCEs) with nickel-benzene tricarboxylic acid MOF ($Ni_3(BTC)_2$ MOF), conjugating aptamers pre-incubated with virus, forming MIPs, and washing off virus. Electrochemical impedance spectroscopy (EIS) detected intact SARS-CoV-2 virus with a detection limit of 3.3 PFU/mL. In addition, the biosensor correctly identified 15 positive and 15 negative patient samples in agreement with PCR tests. Rahmati et. al. also demonstrated reusability by washing and measuring sample repeatedly five times.

One drawback of this system is the need for imprinting the polymer using virus, which a process that may not scale up appropriately. In any case, the dual-recognition biosensor demonstrated key E-AB properties such as high sensitivity, reusability, and stability.

E-ABs have also expanded beyond *in vitro* use: Arroyo-Curras et. al. conducted real-time measurements of four different antibiotics using an E-AB[88]. These applications are beyond the scope of this Review but show the expansive use cases for aptamer biosensors. The potential applications of and opportunities for E-ABs continue to grow as researchers discover more aptamer sequences and develop new detection strategies.

Colorimetric

Colorimetric sensors are another type of aptamer biosensors that rely on color change to indicate detection. The most well-known example is the **lateral flow assay (LFA)**, which were first pioneered in urine pregnancy tests[89] and recently in COVID-19 rapid tests. LFAs are portable, single-use paper devices containing detection agents activated by the liquid sample and rapidly return qualitative results. Two main types of LFA strategies exist: sandwich and competitive LFAs.

In a typical sandwich-type LFA, a liquid sample containing analyte is applied to a sample pad, which also contains dried detection agents, such as antibody-conjugated gold nanoparticles. (Sometimes the detection agents are dried in the sample tube instead.) As capillary action of the strip wicks up the sample, the liquid rehydrates the recognition agents and passes through test lines on the strip. These test lines have capture agents that isolate the analyte-detection agent complex (“test”) or isolate only the detection agent (“control”). At the terminal of the strip, an absorbent pad soaks liquid to maintain the flow. The results can be observed by the untrained eye and gives a semi-binary result (the band intensity may correlate with analyte concentration.) A test band is formed by the detection agent, analyte, and capture agent “sandwich”. A control band is formed by the detection agent, indicating a valid test. Similarly, a competitive LFA contains two probes, one starting on the test band and another on the control band. After analyte sample is applied, the analyte displaces the test band probes but not the control band probes. As a result, the absence of the test band indicates presence of the analyte.[90,91]

Most available LFAs rely on antibodies as the detection agent and are therefore also known as lateral flow immunoassays. However, aptamers are alternatives to antibodies that are lower cost to produce, more shelf stable, and less variable batch-to-batch. Minimizing production cost, lengthening shelf life, and increasing consistency between production runs are qualities necessary for commercializing LFAs. As a result, aptamers can address some of the shortcomings of LFAs by substituting for antibodies[91–93]. A recent review article evaluated aptamer LFAs extensively[93], so we will highlight select publications to showcase aptamer LFAs and demonstrate how aptamers provide a unique advantage.

Several aptamer LFAs have been developed for SARS-CoV-2 detection. Zhang et. al. produced an aptamer-antibody sandwich LFA using antibodies to capture and two different aptamer sequences on gold nanoparticles to detect as low as 20 pM SARS-CoV-2 nucleocapsid protein[59]. Yang et. al. created an antibody-free aptamer-aptamer sandwich LFA (AptaFlow) using two different SARS-CoV-2 spike protein binding aptamer sequences for detection and capture, respectively. The detection limit of

AptaFlow was 100 pM SARS-CoV-2 spike protein and 10^6 copies/mL of intact SARS-CoV-2 virus as seen by eye after using signal enhancement.[41]

Aptamers provide many advantages over antibodies for LFAs. Aptamers are easier to conjugate to gold nanoparticles than antibodies because they can be synthesized with a 5' or 3' end thiol group for conjugation to gold nanoparticles in a straightforward process.[41,94] On the other hand, antibodies can be covalently conjugated by functionalizing existing chemical groups, such as primary amines on lysine residues. However, thiol-based conjugation chemistry requires multiple steps using bifunctional linkers and may attach antibodies at different sites and orientations, and strategies that use adapter molecules like streptavidin/biotin prohibit adapter molecule use in the LFA itself. [95] In addition, antibodies have batch-to-batch variation due to being produced in animals, while aptamers are chemically synthesized and can be more consistent for LFA production. Some drawbacks of aptamer LFA compared to other biosensors include lower sensitivity and qualitative results. These properties can be improved by signal amplification or quantitative image analysis. However, the ease of use, rapid results, portability, and inexpensive production cost are distinctive benefits of aptamer LFAs.

Another colorimetric assay compatible with aptamer substitution is enzyme-linked immunosorbent assay (ELISA). Aptamers instead of antibodies can be used as molecular recognition agents and therefore the assay can be renamed enzyme-linked apta-sorbent assay (ELASA). Much like LFAs, there are several different ELASA detection strategies including direct, sandwich, and competitive. In a typical direct ELASA, the analyte is immobilized onto a surface and detected by biotinylated aptamers and streptavidin-conjugated horseradish peroxidase (HRP). Due to ease of set up, direct ELASAs are useful for screening SELEX aptamer pools and candidate aptamer sequences[41,58]. In sandwich ELASAs, one molecular recognition agent captures the analyte onto the surface, and another molecular recognition agent detects it. Sandwich ELASAs are the most common type of ELASA and has many permutations (capture antibody or aptamer, detection aptamer or antibody, additional detection antibody). For competitive ELASAs, the addition of unlabeled analyte from sample removes labeled analyte from the aptamer, resulting in a decrease in signal. The substrate often used for read-out is 3,3′ ,5,5′ -tetramethylbenzidine (TMB), which changes from colorless to blue in the presence of HRP. The color change is visible by eye and quantified by microplate readers[96]. Chemiluminescent substrates like luminol can also be used in ELASAs and are more sensitive than color-changing ones.

Sandwich ELASAs with picomolar or lower detection limits for SARS-CoV-2 proteins[25,97], C-reactive protein[98], and amyloid beta oligomer[99] have recently been reported. Although they require trained personnel and lab equipment to complete, ELASAs take advantage of established techniques and materials to apply aptamers to biosensing.

Apart from LFA and ELISA, many other colorimetric aptamer assays exist and use unique strategies. One mainstay strategy utilizes gold nanoparticles (AuNPs) and their interparticle distance-dependent color-changing property for detection. Dispersed, small (10-50 nm diameter) AuNPs appear red due to light-induced surface electron oscillation. As the size of the particle increases (via larger diameter or aggregation of small particles), the particles combine surface plasmons and become blue in color.[100] When aptamer-functionalized AuNPs are mixed with analyte, the aptamer binds the analyte and AuNPs aggregate, shifting the solution color from red to blue.

A recent and representative aptamer-AuNP example, Gupta et. al. synthesized dual-functionalized AuNPs for detecting *E. coli* responsible for foodborne illnesses. AuNPs were coated with graphene oxide (GO) then immobilized with amine-functionalized aptamers[101]. In the presence of *E. coli* cells, the AuNPs aggregate, and the solution becomes bluer. The limit of detection was 100 cells/mL by eye and 10 cells/mL by UV-vis spectroscopy. In addition, Gupta et. al. showed specificity for *E. coli* among other non-target bacteria and detection of *E. coli* in diluted coconut water. Overall, the GO- and aptamer-functionalized AuNPs show promise as way to detect foodborne *E. coli*. However, the AuNPs are sensitive to salt and ion concentrations in solution, and colored or opaque samples interfere with observing color change.

Similarly, Tian et. al. produced a multicolored aptamer- and gold nanorod-based platform for ochratoxin A (OTA), a mycotoxin found in spoiled food[102]. Initially, the biotinylated aptamer remains bound to streptavidin magnetic beads, and biotinylated complementary DNA remains bound to alkaline phosphatase streptavidin. After incubation with OTA, the aptamer binds OTA and releases the complementary DNA-alkaline phosphatase complex. The complex is magnetically separated from the aptamer-bound beads, and the remaining alkaline phosphatase catalyzes the dephosphorylation of ascorbic acid 2-phosphate to ascorbic acid. The ascorbic acid deposits silver ions onto the gold nanorod, producing vibrant color changes (pink to yellow, green, and violet) dependent on the initial concentration of OTA. The biosensor had a limit of detection of 9 nM of OTA as determined by UV-vis spectroscopy, and could also detect 250 nM of OTA in 2% grape juice. Akin to other AuNP strategies, the system would not be effective when measuring samples with reducing agents that can also deposit silver ions, hence testing 50-fold dilutions, or samples with inherent color.

In addition, the magnetic separation step requires sample processing and equipment, which may pose a challenge to translation.

Another colorimetric strategy, Tang et. al. designed an aptamer biosensor based on the peroxidase-mimicking material tungsten disulfide (WS_2)[103]. Aptamers adsorbed onto WS_2 nanosheets increase the material's peroxidase activity, which drives the conversion of TMB substrate to blue products. In the presence of kanamycin, aptamers bind kanamycin and no longer enhance peroxidase activity, leaving a light blue or colorless TMB product. The calculated limit of detection for the biosensor was 60 nM kanamycin by absorbance reader, and about 400 nM showed a color difference discernible by eye (0.1 OD). The aptamer WS_2 system was also able to detect kanamycin spiked into food samples, such as honey, milk, and pork. The biosensor has catalytic activity in a wide range of temperatures (-20 to 80^{o}C), which is superior to natural enzymes that perform optimally within a narrow temperature range. Taken together, Tang et. al. present a colorimetric sensor that cleverly uses aptamer properties to enhance peroxidase activity for signal, detect in a wide variety of sample types, and augment thermal stability.

As a whole, colorimetric aptamer biosensors have excellent potential for single-use, point-of-care detection, which is needed in healthcare and food safety applications. As evident in the COVID-19 pandemic, LFAs are a powerful tool for home diagnostics as healthcare shifts focus to mobile care instead of facility-based care. Aptamer-based LFAs can retain the sensitivity of antibody-based ones while also reducing production costs and increasing shelf life. Similarly, aptamers applied to other single-use tests provide those advantages. However, challenges still remain for colorimetric aptamer biosensors.

Fluorescence

Fluorescence-based detection also a key investigation area for aptamer biosensors. Although aptamers can be simply substituted in for antibodies in fluorescence read-out assays similar to ELASA[80], many recent publications also leverage aptamer's other properties. For example, they may take advantage of the aptamer's DNA composition in order to specifically amplify signal via PCR or inhibit signal via DNase.

Liu et. al. designed an aptamer-based proximity ligation assay (Apt-PLA) that fluoresces during qPCR amplification.[104] When two aptamer probes bind to the target protein, the ligation region of both probes are brought together, allowing ligase to connect the two probes. This completed stretch of DNA is amplified during real-time PCR, resulting in signal via a fluorescent reporter molecule. Apt-PLA detects SARS-CoV-2 nucleocapsid protein with a limit of detection of 37.5 pg/mL, which is on par with commercial ELISA tests, and performs similarly with 100% human serum. Liu et. al. also configured the PLA system with proteins instead of aptamers. One potential drawback is that generating the protein-based system is not cost effective due to high production costs to produce proteins and conjugate DNA probes.

In another fluorescence biosensor, aptamer-functionalized carbon dots were used to detect protein tyrosine kinase 7 (PTK 7), which is overexpressed in several cancers.[105] PTK 7-binding aptamer was immobilized onto carbon dots, and its fluorescence is quenched by complementary DNA (cDNA) immobilized on magnetic nanoparticles (MNPs). In the presence of PTK 7, the aptamer binds PTK 7 instead of base-pairing with its cDNA, allowing separation of the yellow carbon dots from MNPs by magnet. DNAse I was also used to free PTK 7 and amplify the signal in a positive feedback loop. Using this platform, Ma et. al. were able to detect PTK 7 with a limit of detection of 0.015 ng/mL, as well as detect PTK 7 on cells and in human serum.

As a whole, fluorescence-based aptamer biosensors show great potential for highly sensitive and cost-effective detection. They often have sensitivities on par with commercially available kits that rely on antibodies instead of aptamers. However, fluorescence-based biosensors are often not point-of-care devices and require training and equipment to process and analyze. Ongoing investigation into these biosensors will need to improve their cost effectiveness and ease of use for clinical translation.

Gravimetric

Mass-sensitive detection is another label-free application avenue for aptamers. Microcantilevers are regularly used in microfluidic platforms for real-time, label-free mass measurements. When conjugated to the surfaces of microcantilevers, aptamers can immobilize their targets and cause a signal change in the microcantilever. In stress mode, the additional mass on the cantilever surface causes the microcantilever to bend, which can be measured by a laser and detector.[106] Aptamer-functionalized microcantilevers have recently been applied to detect liver toxin microcystin-leucine-arginine (MC-LR)[107], epithelial tumor marker Mucin 1[108], and tumor biomarkers (carcinoembryonic antigen and alpha-fetoprotein).[109]

References

1 B. C. Stark, R. Kole, E. J. Bowman and S. Altman, *Proceedings of the National Academy of Sciences*, 1978, **75**, 3717–3721.

2 K. Kruger, P. J. Grabowski, A. J. Zaug, J. Sands, D. E. Gottschling and T. R. Cech, *Cell*, 1982, **31**, 147–157.

3 C. Guerrier-Takada, K. Gardiner, T. Marsh, N. Pace and S. Altman, *Cell*, 1983, **35**, 849–857.

4 B. R. Cullen and W. C. Greene, *Cell*, 1989, **58**, 423–426.

5 D. L. Robertson and G. F. Joyce, *Letters to nature*, 1990, **344**, 467–468.

6 C. Tuerk and L. Gold, *Science*, 1990, **249**, 505–510.

7 R. Green, A. D. Ellington and J. W. Szostak, *Nature*, 1990, **347**, 406–408.

8 C. Wilson and J. W. Szostak, 1995, **374**, 6.

9 L. C. Bock, L. C. Griffin, J. A. Latham, E. H. Vermaas and J. J. Toole, *Nature*, 1992, **355**, 564–566.

10 A. D. Ellington and J. W. Szostak, *Nature*, 1992, **355**, 850–852.

11 M. Homann and H. U. Göringer, *Nucleic Acids Research*, 1999, **27**, 2006–2014.

12 J.-H. Lee, M. D. Canny, A. De Erkenez, D. Krilleke, Y.-S. Ng, D. T. Shima, A. Pardi and F. Jucker, *Proceedings of the National Academy of Sciences*, 2005, **102**, 18902–18907.

13 D. H. J. Bunka and P. G. Stockley, *Nature Reviews Microbiology*, 2006, **4**, 588–596.

14 L. I. Hernandez, I. Machado, T. Schafer and F. J. Hernandez, *Current Topics in Medicinal Chemistry*, 2015, **15**, 1066–1081.

15 A. V. Lakhin, V. Z. Tarantul and L. V. Gening, *Acta Naturae*, 2013, **5**, 34–43.

16 M. R. Gotrik, T. A. Feagin, A. T. Csordas, M. A. Nakamoto and H. T. Soh, *Accounts of Chemical Research*, 2016, **49**, 1903–1910.

17 A. D. Keefe, S. Pai and A. Ellington, *Nature Reviews Drug Discovery*, 2010, **9**, 537–550.

18 S. Tombelli, M. Minunni and M. Mascini, *Biosensors and Bioelectronics*, 2005, **20**, 2424–2434.

19 T. Wang, C. Chen, L. M. Larcher, R. A. Barrero and R. N. Veedu, *Biotechnology Advances*, 2019, **37**, 28–50.

20 M. C. Cowperthwaite and A. D. Ellington, *J Mol Evol*, 2008, **67**, 95–102.

21 K. Pobanz and A. Lupták, *Methods*, 2016, **106**, 14–20.

22 A. Schmitz, A. Weber, M. Bayin, S. Breuers, V. Fieberg, M. Famulok and G. Mayer, *Angewandte Chemie - International Edition*, 2021, 2–9.

23 N. Kacherovsky, I. I. Cardle, E. L. Cheng, J. L. Yu, M. L. Baldwin, S. J. Salipante, M. C. Jensen and S. H. Pun, *Nature Biomedical Engineering*, 2019, **3**, 783–795.

24 M. Legiewicz, C. Lozupone, R. Knight and M. Yarus, *RNA*, 2005, **11**, 1701–1709.

25 N. Kacherovsky, L. F. Yang, H. V. Dang, E. L. Cheng, I. I. Cardle, A. C. Walls, M. McCallum, D. L. Sellers, F. DiMaio, S. J. Salipante, D. Corti, D. Veesler and S. Pun, *Angew. Chem. Int. Ed.*, 2021, anie.202107730.

26 M. I. Umar, C.-Y. Chan and C. K. Kwok, *Nat Protoc*, 2022, **17**, 1385–1414.

27 M. L. Bochman, K. Paeschke and V. A. Zakian, *Nat Rev Genet*, 2012, **13**, 770–780.

28 C. Roxo, W. Kotkowiak and A. Pasternak, *Molecules*, 2019, **24**, 3781.

29 P. J. Bates, D. A. Laber, D. M. Miller, S. D. Thomas and J. O. Trent, *Experimental and Molecular Pathology*, 2009, **86**, 151–164.

30 J. P. Elskens, J. M. Elskens and A. Madder, *International Journal of Molecular Sciences*, 2020, **21**, 4522.

31 C. M. McCloskey, Q. Li, E. J. Yik, N. Chim, A. K. Ngor, E. Medina, I. Grubisic, L. Co Ting Keh, R. Poplin and J. C. Chaput, *ACS Synth. Biol.*, 2021, **10**, 3190–3199.

32 F. Pfeiffer, F. Tolle, M. Rosenthal, G. M. Brändle, J. Ewers and G. Mayer, *Nat Protoc*, 2018, **13**, 1153–1180.

33 D. Eulberg and S. Klussmann, *ChemBioChem*, 2003, **4**, 979–983.

34 A. Vater, F. Jarosch, K. Buchner and S. Klussmann, *Nucleic Acids Research*, 2003, **31**, e130.

35 T. Bing, N. Zhang and D. Shangguan, *Advanced Biosystems*, 2019, **3**, 1900193.

36 B. J. Hicke, C. Marion, Y.-F. Chang, T. Gould, C. K. Lynott, D. Parma, P. G. Schmidt and S. Warren, *Journal of Biological Chemistry*, 2001, **276**, 48644–48654.

37 N. Lin, L. Wu, X. Xu, Q. Wu, Y. Wang, H. Shen, Y. Song, H. Wang, Z. Zhu, D. Kang and C. Yang, *ACS Appl. Mater. Interfaces*, 2021, **13**, 9306–9315.

38 C. Kolm, I. Cervenka, U. J. Aschl, N. Baumann, S. Jakwerth, R. Krska, R. L. Mach, R. Sommer, M. C. DeRosa, A. K. T. Kirschner, A. H. Farnleitner and G. H. Reischer, *Sci Rep*, 2020, **10**, 20917.

39 K. Sefah, D. Shangguan, X. Xiong, M. B. O’Donoghue and W. Tan, *Nature Protocols*, 2010, **5**, 1169–1185.

40 M. Khedri, K. Abnous, H. Rafatpanah, M. S. Nabavinia, S. M. Taghdisi and M. Ramezani, *Immunological Investigations*, 2020, **49**, 535–554.

41 L. F. Yang, N. Kacherovsky, N. Panpradist, R. Wan, J. Liang, B. Zhang, S. J. Salipante, B. R. Lutz and S. H. Pun, *Anal. Chem.*, , DOI:10.1021/acs.analchem.2c00554.

42 Z. Zhang, J. Li, J. Gu, R. Amini, H. D. Stacey, J. C. Ang, D. White, C. D. M. Filipe, K. Mossman, M. S. Miller, B. J. Salena, D. Yamamura, P. Sen, L. Soleymani, J. D. Brennan and Y. Li, *Chemistry – A European Journal*, 2022, **28**, e202200078.

43 C. Narayan, J. Kwon, C. Kim, S.-J. Kim and S. Key Jang, *Analyst*, 2020, **145**, 1473–1482.

44 S. D. Mendonsa and M. T. Bowser, *J. Am. Chem. Soc.*, 2004, **126**, 20–21.

45 C. Zhu, X. Wang, L. Li, C. Hao, Y. Hu, A. S. Rizvi and F. Qu, *Biochemical and Biophysical Research Communications*, 2018, **506**, 169–175.

46 Z. Luo, H. Zhou, H. Jiang, H. Ou, X. Li and L. Zhang, *Analyst*, 2015, **140**, 2664–2670.

47 A. T. H. Le, S. M. Krylova, M. Kanoatov, S. Desai and S. N. Krylov, *Angewandte Chemie*, 2019, **131**, 2765–2769.

48 R. Stoltenburg, C. Reinemann and B. Strehlitz, *Anal Bioanal Chem*, 2005, **383**, 83–91.

49 Y. Song, Z. Zhu, Y. An, W. Zhang, H. Zhang, D. Liu, C. Yu, W. Duan and C. J. Yang, *Anal. Chem.*, 2013, **85**, 4141–4149.

50 M. Khati, M. Schüman, J. Ibrahim, Q. Sattentau, S. Gordon and W. James, *Journal of Virology*, 2003, **77**, 12692–12698.

51 T. S. Misono and P. K. R. Kumar, *Analytical Biochemistry*, 2005, **342**, 312–317.

52 H. Kaur, M. Shorie and P. Sabherwal, *Biosensors and Bioelectronics*, 2020, **167**, 112498.

53 M. Mukherjee, P. Appaiah, S. Sistla, B. Bk and P. Bhatt, *J. Agric. Food Chem.*, 2022, **70**, 6239–6246.

54 S. Saito, *Anal. Sci.*, 2021, **37**, 17–26.

55 D. Wu, C. K. L. Gordon, J. H. Shin, M. Eisenstein and H. T. Soh, *Acc. Chem. Res.*, 2022, **55**, 685–695.

56 M. Avci-Adali, A. Paul, N. Wilhelm, G. Ziemer and H. P. Wendel, *Molecules*, 2010, **15**, 1–11.

57 K. Sefah, D. Shangguan, X. Xiong, M. B. O'Donoghue and W. Tan, *Nat Protoc*, 2010, **5**, 1169–1185.

58 J. G. Bruno, M. P. Carrillo, A. M. Richarte, T. Phillips, C. Andrews and J. S. Lee, *BMC Research Notes*, 2012, **5**, 633.

59 L. Zhang, X. Fang, X. Liu, H. Ou, H. Zhang, J. Wang, Q. Li, H. Cheng, W. Zhang and Z. Luo, *Chemical Communications*, 2020, **56**, 10235–10238.

60 M. L. Metzker, *Nat Rev Genet*, 2010, **11**, 31–46.

61 G. Hybarger, J. Bynum, R. F. Williams, J. J. Valdes and J. P. Chambers, *Anal Bioanal Chem*, 2006, **384**, 191–198.

62 H. Jiang, X.-F. Lv and K.-X. Zhao, *Chinese Journal of Analytical Chemistry*, 2020, **48**, 590–600.

63 A. Sinha, P. Gopinathan, Y.-D. Chung, H.-Y. Lin, K.-H. Li, H.-P. Ma, P.-C. Huang, S.-C. Shiesh and G.-B. Lee, *Biosensors and Bioelectronics*, 2018, **122**, 104–112.

64 R. A. Langan, S. E. Boyken, A. H. Ng, J. A. Samson, G. Dods, A. M. Westbrook, T. H. Nguyen, M. J. Lajoie, Z. Chen, S. Berger, V. K. Mulligan, J. E. Dueber, W. R. P. Novak, H. El-Samad and D. Baker, *Nature*, 2019, **572**, 205–210.

65 A. Quijano-Rubio, H.-W. Yeh, J. Park, H. Lee, R. A. Langan, S. E. Boyken, M. J. Lajoie, L. Cao, C. M. Chow, M. C. Miranda, J. Wi, H. J. Hong, L. Stewart, B.-H. Oh and D. Baker, *Nature*, 2021, **591**, 482–487.

66 O. Rabal, F. Pastor, H. Villanueva, M. M. Soldevilla, S. Hervas-Stubbs and J. Oyarzabal, *Molecular Therapy - Nucleic Acids*, 2016, **5**, e376.

67 Y. Song, J. Song, X. Wei, M. Huang, M. Sun, L. Zhu, B. Lin, H. Shen, Z. Zhu and C. Yang, *Analytical Chemistry*, 2020, **92**, 9895–9900.

68 A. B. Iliuk, L. Hu and W. A. Tao, *Anal. Chem.*, 2011, **83**, 4440–4452.

69 N. I. Khan and E. Song, *Micromachines*, 2020, **11**, 220.

70 R. J. White, A. A. Rowe and K. W. Plaxco, *Analyst*, 2010, **135**, 589–594.

71 L. R. Schoukroun-Barnes, F. C. Macazo, B. Gutierrez, J. Lottermoser, J. Liu and R. J. White, *Annual Review of Analytical Chemistry*, 2016, **9**, 163–181.

72 Y. Xiao, A. A. Lubin, A. J. Heeger and K. W. Plaxco, *Angewandte Chemie*, 2005, **117**, 5592–5595.

73 B. R. Baker, R. Y. Lai, M. S. Wood, E. H. Doctor, A. J. Heeger and K. W. Plaxco, *Journal of the American Chemical Society*, 2006, **128**, 3138–3139.

74 Z. gang Yu, A. L. Sutlief and R. Y. Lai, *Sensors and Actuators, B: Chemical*, 2018, **258**, 722–729.

75 M. Jarczewska, J. Rębiś, Ł. Górski and E. Malinowska, *Talanta*, 2018, **189**, 45–54.

76 Y. Wu, B. Midinov and R. J. White, *ACS Sensors*, 2019, **4**, 498–503.

77 S. Dolai and M. Tabib-Azar, *Medical Devices & Sensors*, 2020, **3**, 1–9.

78 J. Kwon, Y. Lee, T. Lee and J. H. Ahn, *Analytical Chemistry*, 2020, **92**, 5524–5531.

79 P. Lasserre, B. Balansethupathy, V. J. Vezza, A. Butterworth, A. Macdonald, E. O. Blair, L. McAteer, S. Hannah, A. C. Ward, P. A. Hoskisson, A. Longmuir, S. Setford, E. C. W. Farmer, M. E. Murphy, H. Flynn and D. K. Corrigan, *Anal. Chem.*, 2022, **94**, 2126–2133.

80 M. A. Martínez-Roque, P. A. Franco-Urquijo, V. M. García-Velásquez, M. Choukeife, G. Mayer, S. R. Molina-Ramírez, G. Figueroa-Miranda, D. Mayer and L. M. Alvarez-Salas, *Analytical Biochemistry*, 2022, **645**, 114633.

81 F. Li, W. Yang, B. Zhao, S. Yang, Q. Tang, X. Chen, H. Dai and P. Liu, *Advanced Science*, 2022, **9**, 2102804.

82 H. Yu, Z. Chen, Y. Liu, O. Alkhamis, Z. Song and Y. Xiao, *Angewandte Chemie*, 2021, **133**, 3030–3037.

83 Y. Liu, O. Alkhamis, X. Liu, H. Yu, J. Canoura and Y. Xiao, *ACS Appl. Mater. Interfaces*, 2021, **13**, 17330–17339.

84 M. Alafeef, K. Dighe, P. Moitra and D. Pan, *ACS Nano*, 2020, **14**, 17028–17045.

85 D. K. Ban, T. Bodily, A. G. Karkisaval, Y. Dong, S. Natani, A. Ramanathan, A. Ramil, S. Srivastava, P. Bandaru, G. Glinsky and R. Lal, *Proceedings of the National Academy of Sciences*, 2022, **119**, e2206521119.

86 Z. Rahmati and M. Roushani, *Microchim Acta*, 2022, **189**, 287.

87 F. Curti, S. Fortunati, W. Knoll, M. Giannetto, R. Corradini, A. Bertucci and M. Careri, *ACS Appl. Mater. Interfaces*, 2022, **14**, 19204–19211.

88 N. Arroyo-Currás, J. Somerson, P. A. Vieira, K. L. Ploense, T. E. Kippin and K. W. Plaxco, *Proc Natl Acad Sci U S A*, 2017, **114**, 645–650.

89 L. Wide and C. A. Gemzell, *European Journal of Endocrinology*, 1960, **XXXV**, 261–267.

90 G. A. Posthuma-Trumpie, J. Korf and A. van Amerongen, *Anal Bioanal Chem*, 2009, **393**, 569–582.

91 Designs, formats and applications of lateral flow assay, https://reader.elsevier.com/reader/sd/pii/S131961031400129X?token=E2B37343540DAED88C8770C82405099755EECA91A4B55288D121F5DE8B954BB9DA50CD960E9C049A75F8F3F7CE97039F&originRegion=us-east-1&originCreation=20220721231036, (accessed July 21, 2022).

92 A. Chen and S. Yang, *Biosensors and Bioelectronics*, 2015, **71**, 230–242.

93 T. Wang, L. Chen, A. Chikkanna, S. Chen, I. Brusius, N. Sbuh and R. N. Veedu, *Theranostics*, 2021, **11**, 5174–5196.

94 J. Liu and Y. Lu, *Nat Protoc*, 2006, **1**, 246–252.

95 M. H. Jazayeri, H. Amani, A. A. Pourfatollah, H. Pazoki-Toroudi and B. Sedighimoghaddam, *Sensing and Bio-Sensing Research*, 2016, **9**, 17–22.

96 S. Y. Toh, M. Citartan, S. C. B. Gopinath and T.-H. Tang, *Biosensors and Bioelectronics*, 2015, **64**, 392–403.

97 Z. Chen, Q. Wu, J. Chen, X. Ni and J. Dai, *Virologica Sinica*, 2020, **35**, 351–354.

98 J. Xie, M.-Q. Tang, J. Chen, Y.-H. Zhu, C.-B. Lei, H.-W. He and X.-H. Xu, *Talanta*, 2020, **217**, 121070.

99 J. Zhao, W. Chang, L. Liu, X. Xing, C. Zhang, H. Meng, S. C. B. Gopinath, T. Lakshmipriya, Y. Chen and Y. Liu, *Journal of Immunological Methods*, 2021, **489**, 112942.

100 W. Zhao, M. A. Brook and Y. Li, *ChemBioChem*, 2008, **9**, 2363–2371.

101 R. Gupta, A. Kumar, S. Kumar, A. K. Pinnaka and N. K. Singhal, *Sensors and Actuators B: Chemical*, 2021, **329**, 129100.

102 F. Tian, J. Zhou, R. Fu, Y. Cui, Q. Zhao, B. Jiao and Y. He, *Food Chemistry*, 2020, **320**, 126607.

103 Y. Tang, Y. Hu, P. Zhou, C. Wang, H. Tao and Y. Wu, *J. Agric. Food Chem.*, 2021, **69**, 2884–2893.

104 R. Liu, L. He, Y. Hu, Z. Luo and J. Zhang, *Chemical Science*, 2020, **11**, 12157–12164.

105 Y. Ma, Y. Wang, Y. Liu, L. Shi and D. Yang, *Journal of Nanobiotechnology*, 2021, **19**, 47.

106 K. M. Hansen and T. Thundat, *Methods*, 2005, **37**, 57–64.

107 G. Zhang, C. Li, S. Wu and Q. Zhang, *Sensors and Actuators B: Chemical*, 2018, **260**, 42–47.

108 C. Li, M. Zhang, Z. Zhang, J. Tang and B. Zhang, *Sensors and Actuators B: Chemical*, 2019, **297**, 126759.

109 C. Li, X. Ma, Y. Guan, J. Tang and B. Zhang, *ACS Sens.*, 2019, **4**, 3034–3041.

110 Y. Zhao, K. Yavari and J. Liu, *TrAC Trends in Analytical Chemistry*, 2022, **146**, 116480.

Chapter 1

Discovery and characterization of spike N-terminal domain-binding aptamers for rapid SARS-CoV-2 detection

Adapted from publication in Angewandte Chemie

Nataly Kacherovsky*, Lucy F. Yang*, Ha V. Dang*, Emmeline L. Cheng, Ian I. Cardle, Alexandra C. Walls, Matthew McCallum, Drew L. Sellers, Frank DiMaio, Stephen J. Salipante, Davide Corti, David Veesler, Suzie H. Pun

Abstract

The coronavirus disease 2019 (COVID-19) pandemic has devastated families and disrupted healthcare, economies and societies across the globe. Molecular recognition agents that are specific for distinct viral proteins are critical components for rapid diagnostics and targeted therapeutics. In this work, we demonstrate the selection of novel DNA aptamers that bind to the SARS-CoV-2 spike glycoprotein with high specificity and affinity (< 80 nM). Through binding assays and high resolution cryo-EM, we demonstrate that SNAP1 (SARS-CoV-2 spike protein N-terminal domain-binding aptamer 1) binds to the S N-terminal domain. We applied SNAP1 in lateral flow assays (LFAs) and ELISAs to detect UV-inactivated SARS-CoV-2 at concentrations as low as 5 x 10^5 copies/mL. SNAP1 is therefore a promising molecular tool for SARS-CoV-2 diagnostics.

Introduction

Effective disease control of the COVID-19 pandemic, caused by severe acute respiratory syndrome coronavirus 2 (SARS-CoV-2)[1] includes early detection of SARS-CoV-2 infections[2]. Despite the deployment of COVID-19 vaccines[3], SARS-CoV-2 diagnostic tools remain critical for reducing virus spread. Furthermore, advances in rapid diagnostics enable better preparation for future pandemics[4].

COVID-19 diagnostic tests for active infections include molecular tests that detect viral RNA by nucleic acid amplification, and rapid antigen tests that detect viral proteins. While molecular tests are extremely sensitive and specific[5], rapid antigen tests are simpler to administer, provide point-of-care results, and are less expensive than molecular tests[6]. Rapid antigen testing reduces COVID-19 prevalence by an estimated 70% compared to unmitigated growth[7].

A major SARS-CoV-2 antigen detected by COVID-19 diagnostics is the spike (S) protein, a transmembrane glycoprotein that protrudes from the viral envelope[8]. Antibodies against SARS-CoV-2 S protein have been isolated[9], and mRNA encoding the S protein is the basis of FDA-authorized mRNA vaccines[10]. SARS-CoV-2, a betacoronavirus, is closely related to SARS-CoV, which caused the 2002-2003 Severe Acute Respiratory Syndrome epidemic, and more distantly related to the MERS-CoV responsible for the 2012 Middle East Respiratory Syndrome outbreak, sharing ~72% and ~35% sequence similarity, respectively, with the S proteins of these viruses[8b]. The SARS-CoV-2 S protein is composed of three identical monomers with two distinct subunits[11]. Subunit 1 (S1) contains a receptor binding domain (RBD), which binds to human angiotensin-converting enzyme 2 (ACE2) and mediates host cell recognition, and an N-terminal domain (NTD)[8a, 11a]. Recently, an antigenic supersite on the NTD was found to be frequently targeted by NTD-binding antibodies[9a], indicating that binders to this site may play a role in specific recognition of and immunity to SARS-CoV-2.

Aptamers are short nucleic acid sequences that bind target molecules. Aptamers not only achieve specific binding with affinities on par with antibodies, but also are cheaper and easier to produce[12]. Novel aptamers are discovered through a library selection method coined systematic evolution of ligands by exponential enrichment (SELEX)[13]. For detection of intact SARS-CoV-2 virus, aptamers that bind to accessible surface proteins such as S are needed.

In this study, we report the discovery and optimization of DNA aptamers that bind SARS-CoV-2 S protein with high affinity and specificity. We identified the aptamers' binding epitope as the NTD of the SARS-CoV-2 S protein by biolayer interferometry (BLI) and cryogenic electron microscopy (Cryo-EM). Currently, there are reports of aptamers binding to RBD of SARS-CoV-2[14]. To our knowledge, the aptamers reported here are the first to bind the NTD of SARS-CoV-2 S. In addition, we present the first cryo-EM map of SARS-CoV-2 S in complex with a DNA aptamer. We then used SNAP1 to detect both S protein and UV-inactivated SARS-CoV-2 by lateral flow assay (LFA) and by ELISA.

Results & Discussion

SELEX Strategy

We designed a protein SELEX strategy using the SARS-CoV-2 S protein as the binding target (Figure 1.1). To minimize selection of non-specific aptamers, we alternated the protein tag (His- and Fc-tag) and corresponding partitioning platforms and increased selective pressure by adding multiple competitors including MERS-CoV S1 and SARS-CoV S1 (Table S1.1). Using an ELISA-like plate binding assay, we detected a 15-fold increase in aptamer binding in the round 11 aptamer pool without a further increase in binding for round 12, indicating that selection was complete (Fig. S1.1). We sequenced the selection rounds (Table S1.2) and analyzed results by FASTAptamer[15]. By round 12, the library had shrunk considerably, and our top aptamer motif (motif 1) accounted for 64.3% of all sequences (Table S1.3, Fig. S1.2). A closely related motif (motif 3) was also present in two of the top 100 ranking aptamers. We characterized the aptamers containing motif 1 (later named SNAP1) and motif 3 (later named SNAP3) (Table S1.4). The predicted secondary structures of the aptamers SNAP1 and SNAP3 and their sequence similarities are shown in Fig. S1.3A-B.

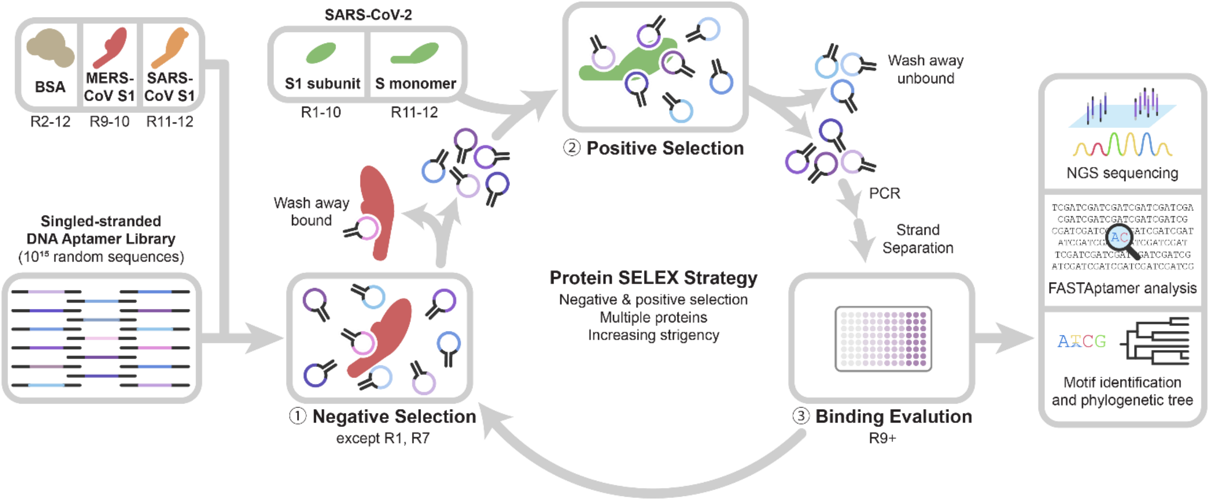

Figure 1.1. Schematic of protein-SELEX strategy using a DNA aptamer library. After an initial round of positive selection, subsequent rounds consisted of negative and positive selection with increasingly stringent conditions (Table S1.1). Negative selection included control proteins (BSA, MERS-CoV S1, or SARS-CoV S1) and protein immobilization platforms.

Aptamer and S protein binding characterization

We demonstrated that Cy5-labeled SNAP1 and SNAP3 bind specifically to SARS-CoV-2 S1 but not SARS-CoV and MERS-CoV S1 proteins using flow cytometry binding studies (Fig. S1.4 and S1.5A). No SNAP1 or SNAP3 binding was observed to a control protein (CD71), and a non-specific (NS) aptamer sequence did not show binding to S1. We further confirmed specificity using biolayer interferometry (BLI) to monitor protein association to immobilized aptamers. We observed that SNAP1 and SNAP3 bind SARS-CoV-2 S1 at < 10 nM protein (Fig. 2A). In addition, SNAP1 did not bind to SARS-CoV S1 or MERS-CoV S1 even at 200 nM protein (Fig. S1.5B). Thus, both aptamers target SARS-CoV-2 S1 with high specificity.

We investigated whether SNAP1 and SNAP3 bind the RBD by ACE2 competition studies but observed no change in binding constants between SARS-CoV-2 S1 and ACE2 in the presence of large excesses of aptamer either by BLI (Fig. S1.6A) or flow cytometry (Fig. S1.6B). We then used BLI to characterize binding of SNAP1 and SNAP3 to SARS-CoV-2 S1 and S1 NTD. Using aptamer-functionalized (SNAP1, SNAP3, and NS) sensors, we determined that the K_D of S1 binding to SNAP1 (39.32 ± 0.12 nM) was about 2-fold lower than that of SNAP3 (76.59 ± 0.45 nM) (Fig 1.2A, Table S5). NS aptamer did not bind to SARS-CoV-2 S1 (Fig. S1.5B). We observed similar equilibrium constants of aptamer binding to S1 NTD as that of S1 (SNAP1 K_D = 60.35 ± 1.61 nM, and SNAP3 K_D = 53.25 ± 2.49 nM for NTD binding) (Fig. 1.2A), indicating that aptamer binding is localized to the NTD on SARS-CoV-2 S1 protein. Accordingly, the aptamers were named SARS-CoV-2 Spike protein NTD-binding APtamers 1 and 3, or SNAP1 and SNAP3, respectively.

We investigated whether SNAP1 and SNAP3 bind to the same NTD site through competition studies. We observed that SNAP3 binding to S1 was reduced to about

50% of maximum binding in the presence of equal amount of SNAP1 (Fig. S1.7), suggesting that SNAP1 and SNAP3 bind to an overlapping epitope on NTD. We therefore used SNAP1 for Cryo-EM characterization.

Cryo-EM characterization of SNAP1 bound to S protein

We determined a Cryo-EM structure of SARS-CoV-2 S bound to SNAP1 in the presence of the S2M11 neutralizing antibody, which overcame preferential specimen orientation in vitreous ice and limited S conformational variability[9e] (Fig. S1.8A-B). We obtained a cryo-EM map at an overall 3.3 Å resolution applying three-fold symmetry (Fig. 1.2B, Fig. S1.8C). The map was best resolved at the SARS-CoV-2 S core, whereas SNAP1 showed a high degree of flexibility outside of its binding contact region with SARS-CoV-2 S (Fig. S1.8D). SNAP1 adopted an overall double-stranded helical shape, extending outwards from the SARS-CoV-2 S trimer. Our map unambiguously identifies that SNAP1 interacts exclusively with the NTD of SARS-CoV-2 S (Fig. 1.2B), in agreement with the results from BLI.

We obtained a 3.6Å reconstruction for the region encompassing SNAP1 and part of SARS-CoV-2 S NTD (Fig. S1.8D inset) through focused 3D classification and local refinement (Fig. S1.8E). SNAP1 contacts residues 68-70, the NTD hairpin formed by residues 140-158, and a loop containing residues 253-257. These latter two regions are part of an antigenic supersite recognized by neutralizing NTD mAbs[9a, 16]. Comparison of the structures of NTD in complex with S2L28, S2M28 or S2X333 Fabs (PDB: 7LXZ, 7LY2, 7LXY) and with SNAP1 shows that these regions on SARS-CoV-2 S NTD are highly dynamic and adopt different conformations upon binding to different molecules[9a]. We likely discovered two NTD-binding aptamers because the NTD antigenic supersite is exposed and differs the most compared to SARS-CoV and MERS-CoV S1. Our SELEX and immune systems of multiple individuals selected for binders to the NTD supersite, which highlights the importance of the NTD in immunity, vaccine design, and diagnostics applications.

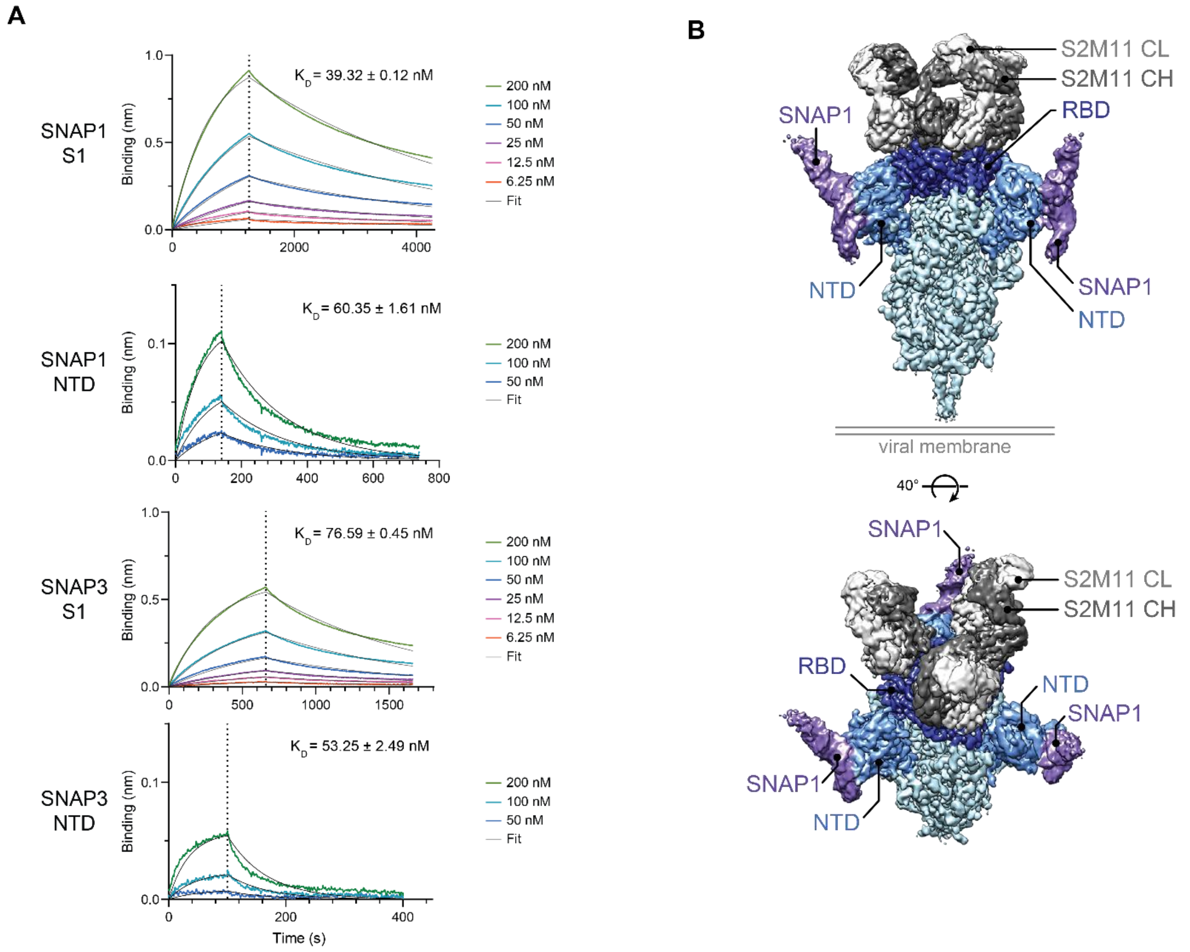

Figure 1.2. SNAP1 and SNAP3 aptamers bind to the NTD of SARS-CoV-2 S protein. A) Kinetic and binding equilibrium constants were measured by BLI. Biotinylated aptamer loaded on streptavidin biosensors was associated with SARS-CoV-2 S1 or NTD. Dotted lines indicate switch from analyte association to dissociation. KD values (mean±s.d., n=5-6) were determined from a global fit of the kinetic data for a 1:1 binding model. B) Two views of the S/SNAP1/S2M11 complex cryo-EM unsharpened map. SNAP1: purple, NTD: light blue, RBD: dark blue, rest of SARS-CoV-2 S: cyan, S2M11 CH (Fab fragment heavy chain): dark gray, S2M11 CL (Fab fragment light chain): light gray.

SNAP1 and mutant S protein binding characterization

Next, we investigated whether SNAP1 can bind to S protein variants. S-2P is a stabilized mutant that contains two proline mutations K986P and V987P[17] and recapitulates the native state of S on SARS-CoV-2[8a, 18] (Fig. S1.9A). We observed striking differences in binding kinetics between trimeric proteins S and S-2P (Fig. S1.9B). SNAP1 bound to S with an on-rate 125-fold higher than that of S-2 (Table S1.5).

We also evaluated SNAP1 binding to the S protein from the B.1.1.7 virus variant (Table S1.6) which contains several deletions in the NTD that affect antibody neutralization (Fig. S91.B). The on-rate of S-B.1.1.7 association to SNAP1 immobilized on the biosensor was in between that of SARS-CoV-2 S and S-2P (S>S-B.1.1.7>S-2P) (Table S1.5). However, we measured a very fast off-rate despite using a trimer, suggesting reduced affinity of SNAP1 to this variant.

Truncated SNAP1 binding characterization

Aptamer truncation has, in some cases, improved binding affinity while reducing synthesis cost[19]. Deleting 10 or 18 nucleotides (nt) of the constant region from each end of SNAP1 did not perturb predicted structures of the random region (Fig. S1.10A). The truncated SNAP1.66 (20 nt deletion, 66 nt total length) and SNAP1.50 (50 nt total length) aptamers have similar equilibrium binding constants as untruncated SNAP1 to both SARS-CoV-2 S1 and NTD (Fig. S1.10B, Table S1.5).

S Protein and UV-inactivated SARS-CoV-2 virus detection by SNAP1

Finally, we applied SNAP1 in LFA and ELISA for aptamer-based detection of SARS-CoV-2 S protein and UV-inactivated SARS-CoV-2. Capitalizing on the trimeric nature of the S protein, we used SNAP1.50 as both the capture and detection agent in the HybriDetect LFA (Fig. 1.3A). We also performed a modified ELISA using SNAP1 to capture SARS-CoV-2 S protein (Fig. 1.3B). We were able to detect as low as 250 pM of SARS-CoV-2 S with LFA (Fig. S11A) and 10 pM S protein with ELISA (Fig. 1.S11B). The LFA detected UV-inactivated SARS-CoV-2 virus but not lentivirus at 2.5 x 10^7 copies/mL (Fig 1.3C). The ELISA detected UV-inactivated SARS-CoV-2 at concentrations as low as 5 x 10^5 copies/mL (Fig. 1.3D). The concentration of SARS-CoV-2 RNA detected in saliva and nasopharyngeal samples from COVID-19 positive patients by RT-qPCR in the first two weeks after onset of symptoms ranged from 10^4 to 10^{10} copies/mL[20]. Therefore, SNAP1 can potentially detect SARS-CoV-2 in patient samples in a clinically relevant scenario. Potential approaches for further improving sensitivity in future diagnostic designs using SNAP1 include multimerizing the aptamer, including an amplification step, or using alternative detection modalities[6a, 21].

In summary, we discovered novel SARS-CoV-2-binding aptamers, characterized binding through real-time kinetics measurements and high resolution cryo-EM, and detected SARS-CoV-2 by LFA and ELISA. Due to the relatively short time frame required for selection, aptamer SELEX can be a first response platform for creating diagnostic agents for emerging diseases.

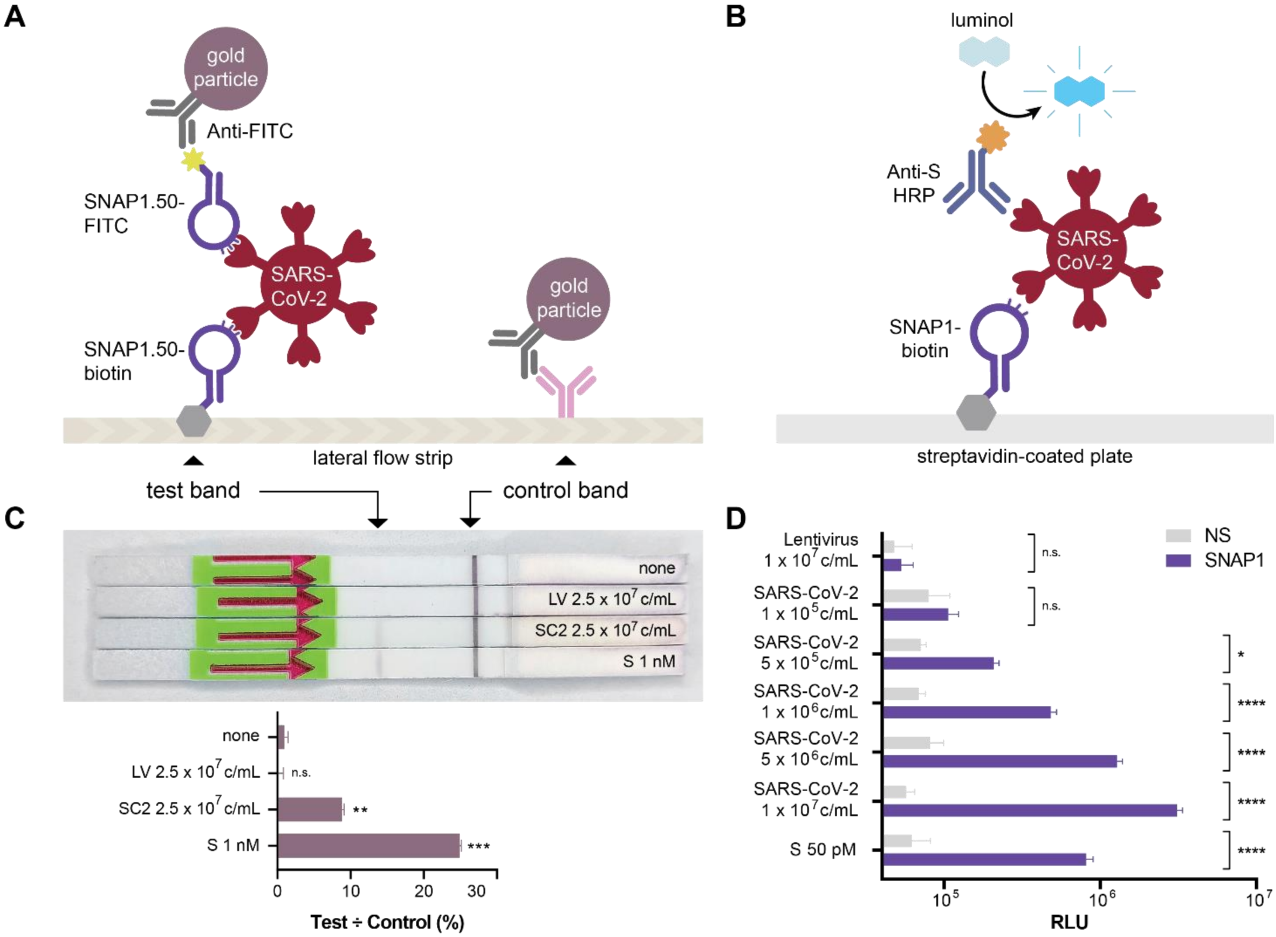

Figure 1.3. Aptamer-based detection of UV-inactivated SARS-CoV-2 virus. A) Schematic of HybriDetect LFA. B) Schematic of aptamer-antibody sandwich ELISA. C-D) c/mL = copies per mL of virus. C) HybriDetect LFA strips were dipped in solutions of S protein (S), control lentivirus (LV), or UV-inactivated SARS-CoV-2 virus (SC2) incubated with SNAP1.50. Top: representative image of developed strips. Bottom: quantification of band intensity. Bar graph shows mean and standard deviation of three replicates. Statistical comparison of LV, SC2, and S to none was determined by one-way ANOVA with Bonferroni correction, *** denotes $p < 0.001$, ** denotes $p < 0.01$, and n.s. denotes no significance. D) ELISA using NS-biotin or SNAP1-biotin as capture agents to detect UV-inactivated SARS-CoV-2 using anti-S HRP antibody for detection. Bar graph shows mean and standard deviation of three replicates. Statistical comparison of NS to SNAP1 was determined by two-way ANOVA with Fisher's LSD test, **** denotes $p < 0.0001$, * denotes $p < 0.05$, and n.s. denotes no significance.

Acknowledgements

This work was supported by a University of Washington Population Health Initiative grant and NIH 1U01AA029316. CryoEM studies were supported by the NIH (R01GM120553, DP1AI158186 and HHSN272201700059C to D.V.), a Pew Biomedical Scholars Award (D.V.), Investigators in the Patho-genesis of Infectious Disease Awards from the Burroughs Wellcome Fund (D.V.), Fast Grants (D.V.), the University of Washington Arnold and Mabel Beckman Center for Cryo-EM, and the Natural Sciences and Engineering Research Council of Canada (M.M.) We thank NIH RADx-Radical Data Coordination Center (DCC) at University of California San Diego (funded under NIH grant # 1U24LM013755-01) for the SARS-Related Coronavirus 2, Isolate USA-WA1/2020, NR-52281 deposited by the Centers for Disease Control and Prevention and obtained through BEI Resources, NIAID. We thank Lauren Carter from the Institute of Protein Design (IPD) who kindly produced S-2P protein through support from the Bill and Melinda Gates Foundation.

Contributions

These authors contributed equally: N.K., L.F.Y., H.V.D.; N.K., L.F.Y., H.V.D., I.C., A.C.W., D.V., and S.H.P. designed research; L.F.Y., N.K., H.V.D, E.L.C., I.I.C., A.C.W., and F.D. performed research. N.K., L.F.Y., and E.L.C. conducted SELEX and round binding studies; E.L.C. and S.J.S. performed NGS; L.F.Y., N.K., and E.L.C. processed and analyzed NGS data; N.K. and I.C.C. generated predicted secondary structures; L.F.Y. and N.K. performed flow cytometry studies; H.V.D. and M.M. produced recombinant proteins; L.F.Y., I.I.C., and H.V.D. performed BLI studies; H.V.D. conducted TEM and Cryo-EM characterization; N.K. and L.F.Y. performed LFA studies; L.F.Y. performed ELISA studies; D.L.S. provided lentivirus; F.D. provided input for Cryo-EM modeling; D.C. provided the S2M11 antibody; L.F.Y. designed the figures; L.F.Y., N.K., H.V.D., D.V., and S.H.P. wrote the paper with input from all authors.

References

[1] aF. Wu, S. Zhao, B. Yu, Y.-M. Chen, W. Wang, Z.-G. Song, Y. Hu, Z.-W. Tao, J.-H. Tian, Y.-Y. Pei, *Nature* **2020**, *579*, 265-269; bP. Zhou, X.-L. Yang, X.-G. Wang, B. Hu, L. Zhang, W. Zhang, H.-R. Si, Y. Zhu, B. Li, C.-L. Huang, *nature* **2020**, *579*, 270-273; cN. Zhu, D. Zhang, W. Wang, X. Li, B. Yang, J. Song, X. Zhao, B. Huang, W. Shi, R. Lu, *New England journal of medicine* **2020**.

[2] A. Spinelli, G. Pellino, *Journal of British Surgery* **2020**, *107*, 785-787.

[3] J. H. Kim, F. Marks, J. D. Clemens, *Nature medicine* **2021**, *27*, 205-211.

[4] S. Simpson, M. C. Kaufmann, V. Glozman, A. Chakrabarti, *The Lancet Infectious Diseases* **2020**, *20*, e108-e115.

[5] J. Joung, A. Ladha, M. Saito, N.-G. Kim, A. E. Woolley, M. Segel, R. P. Barretto, A. Ranu, R. K. Macrae, G. Faure, *New England Journal of Medicine* **2020**, *383*, 1492-1494.

[6] aJ. Dinnes, J. J. Deeks, S. Berhane, M. Taylor, A. Adriano, C. Davenport, S. Dittrich, D. Emperador, Y. Takwoingi, J. Cunningham, *Cochrane Database of Systematic Reviews* **2021**; bS. Lambert-Niclot, A. Cuffel, S. Le Pape, C. Vauloup-Fellous, L. Morand-Joubert, A.-M. Roque-Afonso, J. Le Goff, C. Delaugerre, *Journal of clinical microbiology* **2020**, *58*, e00977-00920.

[7] M. Pavelka, K. Van-Zandvoort, S. Abbott, K. Sherratt, M. Majdan, C. COVID, I. Z. Analýz, P. Jarčuška, M. Krajčí, S. Flasche, *Science* **2021**, *372*, 635-641.

[8] aA. C. Walls, Y.-J. Park, M. A. Tortorici, A. Wall, A. T. McGuire, D. Veesler, *Cell* **2020**, *181*, 281-292. e286; bY.-Z. Zhang, E. C. Holmes, *Cell* **2020**, *181*, 223-227.

[9] aM. McCallum, A. De Marco, F. A. Lempp, M. A. Tortorici, D. Pinto, A. C. Walls, M. Beltramello, A. Chen, Z. Liu, F. Zatta, *Cell* **2021**, *184*, 2332-2347. e2316; bM. A. Tortorici, N. Czudnochowski, T. N. Starr, R. Marzi, A. C. Walls, F. Zatta, J. E. Bowen, S. Jaconi, Z. Wang, A. De Marco, *bioRxiv* **2021**; cT. N. Starr, N. Czudnochowski, F. Zatta, Y.-J. Park, Z. Liu, A. Addetia, D. Pinto, M. Beltramello, P. Hernandez, A. J. Greaney, *bioRxiv* **2021**; dL. Piccoli, Y.-J. Park, M. A. Tortorici, N. Czudnochowski, A. C. Walls, M. Beltramello, C. Silacci-Fregni, D. Pinto, L. E. Rosen, J. E. Bowen, *Cell* **2020**, *183*, 1024-1042. e1021; eM. A. Tortorici, M. Beltramello, F. A. Lempp, D. Pinto, H. V. Dang, L. E. Rosen, M. McCallum, J. Bowen, A. Minola, S. Jaconi, *Science* **2020**, *370*, 950-957; fD. Pinto, Y.-J. Park, M. Beltramello, A. C. Walls, M. A. Tortorici, S. Bianchi, S. Jaconi, K. Culap, F. Zatta, A. De Marco, *Nature* **2020**, *583*, 290-295.

[10] aL. R. Baden, H. M. El Sahly, B. Essink, K. Kotloff, S. Frey, R. Novak, D. Diemert, S. A. Spector, N. Rouphael, C. B. Creech, *New England Journal of Medicine* **2021**, *384*, 403-416; bL. A. Jackson, E. J. Anderson, N. G. Rouphael, P. C. Roberts, M. Makhene, R. N. Coler, M. P. McCullough, J. D. Chappell, M. R. Denison, L. J. Stevens, *New England Journal of Medicine* **2020**.

[11] aF. Li, *Annual review of virology* **2016**, *3*, 237-261; bM. A. Tortorici, D. Veesler, *Advances in virus research* **2019**, *105*, 93-116.

[12] aD. H. Bunka, P. G. Stockley, *Nature Reviews Microbiology* **2006**, *4*, 588-596; bL. I Hernandez, I. Machado, T. Schafer, F. J Hernandez, *Current topics in medicinal chemistry* **2015**, *15*, 1066-1081; cJ. Zhou, J. Rossi, *Nature reviews Drug discovery* **2017**, *16*, 181-202.

[13] aD. L. Robertson, G. F. Joyce, *Nature* **1990**, *344*, 467-468; bA. D. Ellington, J. W. Szostak, *nature* **1990**, *346*, 818-822; cC. Tuerk, L. Gold, *science* **1990**, *249*, 505-510; dK. Sefah, D. Shangguan, X. Xiong, M. B. O'donoghue, W. Tan, *Nature protocols* **2010**, *5*, 1169-1185; eM. R. Gotrik, T. A. Feagin, A. T. Csordas, M. A. Nakamoto, H. T. Soh, *Accounts of chemical research* **2016**, *49*, 1903-1910; fJ. Liu, M. You, Y. Pu, H. Liu, M. Ye, W. Tan, *Current medicinal chemistry* **2011**, *18*, 4117-4125.

[14] aY. Song, J. Song, X. Wei, M. Huang, M. Sun, L. Zhu, B. Lin, H. Shen, Z. Zhu, C. Yang, *Analytical Chemistry* **2020**, *92*, 9895-9900; bM. Sun, S. Liu, X. Wei, S. Wan, M. Huang, T. Song, Y. Lu, X. Weng, Z. Lin, H. Chen, *Angewandte Chemie* **2021**, *133*, 10354-10360.

[15] K. K. Alam, J. L. Chang, D. H. Burke, *Molecular Therapy-Nucleic Acids* **2015**, *4*, e230.

[16] aY. Chi, J. Remsik, V. Kiseliovas, C. Derderian, U. Sener, M. Alghader, F. Saadeh, K. Nikishina, T. Bale, C. Iacobuzio-Donahue, *Science* **2020**, *369*, 276-282; bL. Zhang, L. Cao, X. Gao, B. Zheng, Y. Deng, J.-X. Li, R. Feng, Q. Bian, X.-L. Guo, N. Wang, *bioRxiv* **2020**; cW. N. Voss, Y. J. Hou, N. V. Johnson, G. Delidakis, J. E. Kim, K. Javanmardi, A. P. Horton, F. Bartzoka, C. J. Paresi, Y. Tanno, *Science* **2021**, *372*, 1108-1112.

[17] aR. N. Kirchdoerfer, N. Wang, J. Pallesen, D. Wrapp, H. L. Turner, C. A. Cottrell, K. S. Corbett, B. S. Graham, J. S. McLellan, A. B. Ward, *Scientific reports* **2018**, *8*, 1-11; bJ. Pallesen, N. Wang, K. S. Corbett, D. Wrapp, R. N. Kirchdoerfer, H. L.

Turner, C. A. Cottrell, M. M. Becker, L. Wang, W. Shi, *Proceedings of the National Academy of Sciences* **2017**, *114*, E7348-E7357.

[18] Z. Ke, J. Oton, K. Qu, M. Cortese, V. Zila, L. McKeane, T. Nakane, J. Zivanov, C. J. Neufeldt, B. Cerikan, *Nature* **2020**, *588*, 498-502.

[19] aN. Kacherovsky, I. I. Cardle, E. L. Cheng, L. Y. Jonathan, M. L. Baldwin, S. J. Salipante, M. C. Jensen, S. H. Pun, *Nature biomedical engineering* **2019**, *3*, 783-795; bA. Schmitz, A. Weber, M. Bayin, S. Breuers, V. Fieberg, M. Famulok, G. Mayer, *Angewandte Chemie International Edition* **2021**, *60*, 10279-10285.

[20] A. L. Wyllie, J. Fournier, A. Casanovas-Massana, M. Campbell, M. Tokuyama, P. Vijayakumar, J. L. Warren, B. Geng, M. C. Muenker, A. J. Moore, *New England Journal of Medicine* **2020**, *383*, 1283-1286.

[21] aH. Kuai, Z. Zhao, L. Mo, H. Liu, X. Hu, T. Fu, X. Zhang, W. Tan, *Journal of the American Chemical Society* **2017**, *139*, 9128-9131; bP. Dauphin-Ducharme, K. Yang, N. Arroyo-Currás, K. L. Ploense, Y. Zhang, J. Gerson, M. Kurnik, T. E. Kippin, M. N. Stojanovic, K. W. Plaxco, *ACS sensors* **2019**, *4*, 2832-2837; cN. K. Singh, P. Ray, A. F. Carlin, C. Magallanes, S. C. Morgan, L. C. Laurent, E. S. Aronoff-Spencer, D. A. Hall, *Biosensors and Bioelectronics* **2021**, *180*, 113111; dJ. Deng, F. Tian, C. Liu, Y. Liu, S. Zhao, T. Fu, J. Sun, W. Tan, *Journal of the American Chemical Society* **2021**, *143*, 7261-7266.

Supplementary Information

Materials and Methods

Oligonucleotides. All oligonucleotides were synthesized by Integrated DNA Technologies. The ssDNA library used in the protein SELEX process was TCGCTCTTTCCGCTTCTTCGCGG-N40-CCGCGTAAGTCCGTGTGTGCGAA. The forward primer for amplification was FAM-TCGCTCTTTCCGCTTCTTCG, and the reverse primer for amplification was Biotin-TTCGCACACACGGACTTACG. Oligonucleotide sequences are listed in Table S4. Modifications to oligonucleotides included: FITC (5'- FITC - sequence - 3'), biotin (5'- biotin - iSp18 - sequence - 3'), and Cy5 (5' - Cy5 - sequence - 3'). All aptamer pools and aptamers were annealed before use in SELEX, binding, characterization, and other studies. Aptamers were annealed by diluting to 1 µM in SELEX WB (see buffers below), heating at 95ºC for 5 min, and snap-cooling on ice.

Buffers. The composition of SELEX wash buffer (SELEX WB) is 4.5 g/L glucose, 0.1 g/L $CaCl_2$, 0.2 g/L KCl, 0.2 g/L KH_2PO_4, 0.1 g/L $MgCl_2$ $6H_2O$, 8 g/L NaCl, 2.1716 g/L Na_2HPO_4, and 5mM $MgCl_2$. 2.25g glucose (Sigma) and 2.5 mL 1M $MgCl_2$ is added to 497.5 mL Dulbecco's phosphate-buffered saline (DPBS) with $CaCl_2$ and $MgCl_2$ (Corning). The buffer is filtered through a 0.22µm sterile filter and stored at 4ºC. For binding buffers, yeast tRNA (Invitrogen) (tRNA) and salmon sperm DNA (Invitrogen) (SS DNA) are added to a final concentration of 0.1 mg/mL. Additionally, MACS BSA 10% stock solution (Miltenyi Biotec) is added to 0.1-5% final concentration depending on the assay.

Recombinant proteins. SARS-CoV-2 S protein S1 domain (ACROBiosystems S1N-C5255), SARS-CoV-2 S protein monomer (ACROBiosystems SPN-C52H4), SARS-CoV-2 S protein trimer (ACROBiosystems SPN-C52H8), SARS-CoV-2 S protein S1 NTD (ACROBiosystems S1D-C52H6), SARS-CoV-2 S protein RBD (ACROBiosystems SPD-C5255) were purchased in lyophilized form. SARS-CoV S protein S1 domain (ACROBiosystems S1N-S52H5) and MERS-CoV S protein S1 domain (Sino Biologics 40069-V08H) were also purchased in lyophilized form. The aforementioned proteins were reconstituted, aliquoted, and stored according to manufacturer's recommendations. SARS-CoV-2 S protein trimer "S-2P" was kindly provided by the Institute of Protein Design (IPD) at the University of Washington.

Viruses. Inactivated SARS-CoV-2 virus samples at known concentrations were kindly provided by the NIH RADx-Radical Data Coordination Center (DCC) at University of California San Diego and BEI Resources. Lentivirus was kindly provided by Prof. Drew L. Sellers. Lentivirus concentration was measured by qPCR Lentivirus Titer Kit (Applied Biological Materials).

Protein-SELEX. The protocol was based on the guidelines outlined by Wang et al[1] and is outlined in Figure 1. Experimental conditions for 12 rounds of SELEX are summarized in Table S1. Briefly, partitioning of bound aptamers was achieved by either Dynabeads His-tag isolation & Pulldown (Novex by Life Technologies) or Nab™ protein G Spin Kit (Thermo Scientific), with the exception of round 7. In this round, the aptamer pool bound to SARS-CoV-2 S1-Fc was incubated with magnetic anti-biotin microbeads and applied onto an MS column (Miltenyi Biotec). The flow through fraction was collected and bound to protein G agarose. Aptamers were amplified with Phusion® High-Fidelity DNA

Polymerase (NEB). Annealing, strand separation, and composition of buffers were described previously[2].

Aptamer round pool binding assay. We quantified the binding of the aptamer round pools (Round 9, 10, 11, and 12) to S protein variants using an ELISA-like plate binding assay. Nunc MaxiSorp™ flat-bottom 96-well plates (Thermo Fisher Scientific) were coated with 4.2 µg/mL SARS-CoV-2 spike protein monomer (Acro Biosystems SPN-C52H4) at 4^oC overnight. Then wells were washed four times with wash buffer (0.5% BSA, 0.01% Tween-20 SELEX WB.) Next, wells were incubated with blocking buffer (5% BSA, 0.1 mg/mL tRNA, 0.1 mg/mL SS DNA, 0.01% Tween-20 SELEX WB) for 1.5 hr at room temperature. After blocking buffer removal via flick and tap, 100 nM FAM-labeled aptamer pools or random sequence aptamer (RAN) in binding buffer were incubated for 30min at room temperature. Then the plate was washed four times with wash buffer and stained with HRP anti-fluorescein antibody (1:2000, Abcam cat. no. ab6656) for 1 h at room temperature. Lastly, the plate was washed four times with wash buffer. Pierce TMB substrate kit (Thermo Scientific 1854050) was mixed at 1:1 according to manufacturer's protocol, then added to wells and incubated at room temperature until desired blue color was developed (5-30 min.) 2M sulfuric acid was added to each well to terminate the HRP reaction. All steps use 100 µL of solution, except blocking and washing which use 200 µL. For wash steps, the plate is flicked over a sink then blotted dry. The absorbance of the solution (yellow) was measured using the Infinite 200 PRO plate reader (Tecan) at 450 nm with 550 nm as reference. The absorbance values of the groups were deducted from wells without aptamer and values normalized to the RAN negative control were plotted.

NGS and data analysis. The DNA pools from SELEX rounds were PCR amplified with barcoded primers described in Table S3 using the MiSeq Reagent Kit v2 (300-cycles) (Illumina) and MiSeq System (Illumina) per manufacture's protocol. Exported FASTA files were analyzed with FASTAptamer v1.0.3[3]. The count function was used to calculate rank and reads per million for each sequence, then the compare function was used pair-wise to compare sequences within subsequent SELEX round pools, generating the fold enrichment value. Neighbor joining trees for the top 100 sequences for rounds 9 through 12 were constructed using Simple Phylogeny (https://www.ebi.ac.uk/Tools/phylogeny/simple_phylogeny/), and visualized using FigTree v1.4.4 (http://tree.bio.ed.ac.uk/software/figtree/). In combination with the phylogenetic tree, MEME Suite v5.1.1 was used for motif prediction.

Aptamer binding assay with magnetic spheres. Streptavidin or Protein G Sphero™ magnetic spheres (Spherotech) were used in binding assays. Streptavidin spheres were further modified with biotin anti-6-His epitope tag antibody (Biolegend cat. no. 906103). These spheres were used to immobilize SARS-CoV-2 S1-His and SARS-CoV-2 S1-Fc proteins, respectively. Individual Cy5 labeled aptamers were incubated with SARS-CoV-2 S1 spheres in binding buffer for 30 min at room temperature, washed twice with wash buffer (0.1% BSA, 0.01% Tween-20 SELEX WB) and analyzed by flow cytometry (Attune NxT, Invitrogen).

Biolayer interferometry (BLI). Studies were performed with an Octet Red96 machine (Sartorius) at 25°C and 1,000 rpm sample agitation. Pre-soaked streptavidin (SA) sensors were rinsed in 1% BSA, 0.1 mg/mL tRNA, 0.1 mg/mL SS DNA, 0.01% Tween-20 SELEX WB ("diluent") for 100s. Next, tips were loaded with 50 nM biotinylated aptamer until reaching a 0.5 nm signal threshold. Subsequently, tips were rinsed in diluent for 100s then baselined in diluent for another 100s. After association with protein of interest diluted to the desired concentration, sensor tips were returned to the baseline diluent well for dissociation. Data was analyzed with Octet Data Analysis 9.0 (Sartorius). Kinetic values were determined from a global fit of several curves generated from serial dilutions of the protein in a 1:1 binding model. The quality of the fit was calculated with R^2 and χ^2 values. See Table S5 for the estimated kinetics parameters from these assays.

Cryo-EM specimen preparation and data collection. SARS-CoV-2 S protein (Acro Biosystems: SPN-C52H8) was reconstituted according to manufacturer's protocol and concentrated and buffer-exchanged into TBS pH 8.0 using a 30 kDa MWCO Amicon Ultra centrifugal filter (EMD Millipore). SARS-CoV-2 S protein was incubated with annealed SNAP1 with or without S2M11 Fab fragment at 1:3:2 molar ratio of Spike protomer:SNAP1:S2M11 Fab for 1 hour at room temperature. For the Spike:SNAP1 complex without S2M11, 3 µL of the complex at a concentration of 0.3 mg/mL SARS-CoV-2 S was applied onto glow-discharged C-flat, Cu 200 mesh, CF-1.2/1.3 grids. For the Spike:SNAP1:S2M11 complex, 3 µL of the complex at a concentration of 0.3 mg/mL SARS-CoV-2 S was mixed with 0.3 µL 1% octyl-glucoside (OG) immediately before application onto glow-discharged C-flat, Cu 200 mesh, CF-1.2/1.3 grids. The grids were plunge-frozen frozen in liquid ethane and cooled with liquid nitrogen, using an FEI MK4 Vitrobot with a 6.5 or 7 s blot time. The chamber was kept at 20°C and 100% humidity during the blotting process.

Data acquisition was carried out with the Leginon data collection software[4] on a 200 kV FEI Glacios electron microscope and equipped with a Gatan BioQuantum energy filter (slit width of 20 eV) and a Gatan K2 Summit camera. The nominal magnification was 36,000x and the pixel size was 1.16 Å. The dose rate was adjusted to 8 counts/pixel/s and each movie was acquired in super-resolution mode fractionated in 50 frames of 200 ms each.

Cryo-EM data processing.

For the dataset of Spike in complex with SNAP1 without S2M11, Warp[5] was used to perform motion correction, CTF estimation, particle picking and particle extraction. 25,758 extracted particles with a box size of 400 pixels were exported to cryoSPARC[6] for reference-free 2D classification.

For the Spike:SNAP1:S2M11 dataset, movies were motion-corrected using Warp and exported to cryoSPARC for CTF estimation using CTFFIND4. A set of manually picked particles were used to generate 2D class averages that were subsequently low pass-filtered to 20 Å for Template Picker in cryoSPARC on the whole dataset. All particles from the whole dataset were extracted with a box size of 400 pixels and underwent 2 rounds of reference-free 2D classification in cryoSPARC. 41,071 particles were selected for *ab initio* reconstruction (no symmetry) and non-uniform refinement (NUR) (C3 symmetry)[6], followed by CTF refinement and another round of NUR in cryoSPARC. The particles were exported to RELION v3.0[7] for Bayesian polishing and then uploaded to cryoSPARC for NUR. To improve the density around the SARS-CoV-2 S NTD/SNAP1 interface, the particles were C3-symmetry-expanded and subjected to focus 3D classification without refining angles and shifts using a soft mask encompassing SNAP1 and part of the NTD in RELION. 55,369 particles belonging to the best-resolved classes with the aptamer bound were selected and underwent local refinement in cryoSPARC. Local resolution estimation, local filtering and map sharpening were performed in cryoSPARC. Reported resolutions are based on the gold-standard Fourier shell correlation (GS-FSC) at 0.143 criterion and FSC curve was corrected for the effects of soft masking by high-resolution noise substitution[8]. See Figure S8E for detailed data processing workflow.

Lateral flow assay (HybriDetect). HybriDetect universal lateral flow dipsticks (Milenia Biotec) were used in combination with biotinylated SNAP1.50 aptamer and FITC-labeled SNAP1.50 aptamer. 100µL of 25 nM of both aptamers were incubated with S protein, UV-inactivated SARS-CoV-2 virus, or lentivirus in binding buffer for 20 minutes at room temperature. Then, the lateral flow strip is dipped in the solution and results were interpreted in 10-30 minutes. Images were quantified with ImageJ.

ELISA. Wells of a white streptavidin-coated 96-well plate (Thermo Fisher Scientific) were washed and blotted three times with SELEX WB then incubated with 50 nM biotinylated NS or SNAP1 aptamer at 4ºC for 30 min. After three washes with wash buffer (0.1% Tween-20 2% BSA SELEX), wells were incubated with blocking buffer (5% BSA, 1:100 biotin blocking solution (Vector Laboratories), 0.1 mg/mL tRNA, 0.1 mg/mL SS DNA, 0.1% Tween-20 SELEX WB) for 1.5 hr at room temperature. Subsequently, the wells were incubated with S protein, UV-inactivated SARS-CoV-2 virus, or lentivirus in binding buffer (2% BSA, 0.1 mg/mL tRNA, 0.1 mg/mL SS DNA, 0.1% Tween-20 SELEX WB) for 30 min at room temperature. Then wells were washed four times before incubation with anti-SARS-CoV-2 antibody with HRP (Novus Biologicals cat. no. NBP2-90980H). Lastly, wells were washed six times. All steps use 100 µL of solution, except washing (200 µL of solution.) For wash steps, the plate is flicked over a sink then blotted dry. Ice-cold ELISA Femto Substrate (Thermo Fisher Scientific) was added and the plate luminescence was immediately measured by Infinite 200 PRO plate reader (Tecan) with 250 nm integration time and automatic attenuation.

1. Wang, T., Yin, W., AlShamaileh, H., Zhang, Y., Tran, P. H. L., Nguyen, T. N. G., ... & Duan, W. (2019). A detailed protein-SELEX protocol allowing visual assessments of individual steps for a high success rate. *Human gene therapy methods*, *30*(1), 1-16.
2. Sefah, K., Shangguan, D., Xiong, X., O'donoghue, M. B., & Tan, W. (2010). Development of DNA aptamers using Cell-SELEX. *Nature protocols*, *5*(6), 1169.
3. Alam, K. K., Chang, J. L., & Burke, D. H. (2015). FASTAptamer: a bioinformatic toolkit for high-throughput sequence analysis of combinatorial selections. *Molecular Therapy-Nucleic Acids*, *4*, e230.
4. Suloway, C., Pulokas, J., Fellmann, D., Cheng, A., Guerra, F., Quispe, J., ... & Carragher, B. (2005). Automated molecular microscopy: the new Leginon system. *Journal of structural biology*, *151*(1), 41-60.
5. Tegunov, D., & Cramer, P. (2019). Real-time cryo-electron microscopy data preprocessing with Warp. Nature methods, 16(11), 1146-1152.
6. Punjani, A., Rubinstein, J. L., Fleet, D. J., & Brubaker, M. A. (2017). cryoSPARC: algorithms for rapid unsupervised cryo-EM structure determination. *Nature methods*, *14*(3), 290-296.
7. Zivanov, J., Nakane, T., Forsberg, B. O., Kimanius, D., Hagen, W. J., Lindahl, E., & Scheres, S. H. (2018). New tools for automated high-resolution cryo-EM structure determination in RELION-3. *eLife*, *7*, e42166.

8. Chen, S., McMullan, G., Faruqi, A. R., Murshudov, G. N., Short, J. M., Scheres, S. H., & Henderson, R. (2013). High-resolution noise substitution to measure overfitting and validate resolution in 3D structure determination by single particle electron cryomicroscopy. *Ultramicroscopy*, *135*, 24-35.

Supplementary Tables

Table S1.1. SELEX conditions for 12 rounds of selection. T indicates 0.1 mg/mL yeast tRNA; S indicates 0.1 mg/mL salmon sperm DNA; HTID indicates His-Tag Isolation Dynabeads™.

Round	Aptamer pool (nM)	Binding conditions	Negative Selection	Time (min)	Positive Selection	Time (min)
1	5000	0.1% BSA, T	-	-	50 nM SARS-CoV-2 S1-His; 50 µL HTID	60
2	500	0.1% BSA, T	50 µL HTID	30	20 nM SARS-CoV-2 S1-His; 50 µL HTID	30
3	250	0.5% BSA, T	100 µL HTID	30	5 nM SARS-CoV-2 S1-His; 10 µL HTID	30
4	250	1% BSA, T	100 µL protein G agarose	30	2.5 nM SARS-CoV-2 S1-Fc; 10 µL protein G agarose	30
5	100	1% BSA, T	100 µL protein G agarose-	30	1 nM SARS-CoV-2 S1-Fc; 10 µL protein G agarose	30
6	100	2% BSA, T, S	100 µL protein G agarose	30	1 nM SARS-CoV-2 S1-Fc; 10 µL protein G agarose	30
7	100	2% BSA, T, S	Anti-Biotin magnetic beads; MS column	-	5 nM SARS-CoV-2 S1-Fc; 10 µL protein G agarose	30
8	100	2% BSA, T, S	100 µL HTID	20	2.5 nM SARS-CoV-2 S1-His; 10 µL HTID	20
9	100	2% BSA, T, S	2.5 nM MERS-CoV S1; 10 µL HTID	20	2.5 nM SARS-CoV-2 S1-His; 10 µL HTID	20
10	100	2% BSA, T, S	25 nM MERS-CoV S1; 100 µL HTID	20	2.5 nM SARS-CoV-2 S1-His; 10 µL HTID	20
11	100	2% BSA, T, S	25 nM SARS-CoV S1; 100 µL HTID	20	2.5 nM SARS-CoV-2 S-His; 10 µL HTID	20
12	100	2% BSA, T, S	10nM SARS-CoV S1; 100 µL HTID	20	1 nM SARS-CoV-2 S-His; 10 µL HTID	20

Table S1.2. Next generation sequencing primers. Barcodes are in lowercase.

Name	Sequence
Aptamer_F_v2	AATGATACGGCGACCACCGAGATCTACACACAGACCGTCGTCGCTCTTTCCGCTTCTTCG
Aptamer_R_30v2	CAAGCAGAAGACGGCATACGAGATtggtcagccaCGAGGAGATACCTTCGCACACACGGACTTACG
Aptamer_R_31v2	CAAGCAGAAGACGGCATACGAGATactatgcaatCGAGGAGATACCTTCGCACACACGGACTTACG
Aptamer_R_32v2	CAAGCAGAAGACGGCATACGAGATcgacgcgactCGAGGAGATACCTTCGCACACACGGACTTACG
Aptamer_R_33v2	CAAGCAGAAGACGGCATACGAGATgatacggaacCGAGGAGATACCTTCGCACACACGGACTTACG
Aptamer_R_34v2	CAAGCAGAAGACGGCATACGAGATttatccggatCGAGGAGATACCTTCGCACACACGGACTTACG
Aptamer_R_35v2	CAAGCAGAAGACGGCATACGAGATtagagtaataCGAGGAGATACCTTCGCACACACGGACTTACG
Aptamer_R_36v2	CAAGCAGAAGACGGCATACGAGATgcaggtccgtCGAGGAGATACCTTCGCACACACGGACTTACG
Aptamer_R_37v2	CAAGCAGAAGACGGCATACGAGATtcggccttacCGAGGAGATACCTTCGCACACACGGACTTACG
Aptamer_R_38v2	CAAGCAGAAGACGGCATACGAGATagaacgtctcCGAGGAGATACCTTCGCACACACGGACTTACG
Aptamer_R_39v2	CAAGCAGAAGACGGCATACGAGATccagttccaaCGAGGAGATACCTTCGCACACACGGACTTACG
Aptamer_R_40v2	CAAGCAGAAGACGGCATACGAGATggcgttaaggCGAGGAGATACCTTCGCACACACGGACTTACG
Aptamer_R_41v2	CAAGCAGAAGACGGCATACGAGATacttaaccttCGAGGAGATACCTTCGCACACACGGACTTACG
Aptamer_R_42v2	CAAGCAGAAGACGGCATACGAGATcaaccgctaaCGAGGAGATACCTTCGCACACACGGACTTACG
Aptamer_R_43v2	CAAGCAGAAGACGGCATACGAGATgaccttgataCGAGGAGATACCTTCGCACACACGGACTTACG
Aptamer_R_44v2	CAAGCAGAAGACGGCATACGAGATtctgataccaCGAGGAGATACCTTCGCACACACGGACTTACG

Table S1.3. Motif sequences enriched via SELEX in rounds 9 through 12. Hits are motifs found by MEME Suite within the top 100 sequences. Percent Representation is reads per million of the motif divided by total reads per million. Fold enrichment is the fold enrichment in % representation over previous round. Motifs 1 (purple) and 3 (gold) are underlined. The following letters represent ambiguous base identities: R = AG, Y = CT, K = GT, M = AC, S = CG, W = AT, B = CGT, D = GAT, H = ACT, V = ACG.

Round and hit ranking	Sequence	% Representation	Fold enrichment
R9 Hit 1 (motif 1)	CATTGTGCAYCCTGACTGACCCTAAGGTGCGAACATCGC	0.09%	-
R9 Hit 2 (motif 2)	KCGCAAYAAMYARACARHARWHTDGVSTR	0.017%	-
R9 Hit 3 (motif 3)	SMAASMTCACMGK	0.031%	-
R10 Hit 1 (motif 4)	AAACTYTTGATHMW	0.14%	-
R10 Hit 2 (motif 1)	CATTGTGCAYCCTGACTGACCCTAAGGTGCGAACATCGC	0.03%	0.33
R10 Hit 3 (motif 3)	TTAGBTACAKMGYBTWHATTWCTMAAARTCWTTGTCTA	0.009%	0.29
R11 Hit 1 (motif 3)	TTAGGTACATCGTCTTCATTTCTCAAAGTCATTGTCTACA	0.46%	51
R11 Hit 2 (motif 5)	CAKTBAYCCACACTYTTGATTCAAATWCTCATTTAAATAC	0.18%	-
R11 Hit 3 (motif 1)	CATTGTGCAYCCTGACTGACCCTAAGGTGCGAACATCGC	0.13%	4.3
R12 Hit 1 (motif 1)	TCATTGTGCATCCTGACTGACCCTAAGGTGCGAACATCGC	64.3%	495
R12 Hit 2 (motif 3)	TTAGKTACATCGTCTTCATTTCTCAAAGTCATTGTCTACA	0.18%	0.39
R12 Hit 3 (motif 6)	CAGTSAYCCASACTYTTGATWCAWA	0.12%	0.67

Table S1.4. Aptamer sequences. See methods for list of modifications.

Name	Sequence
RAN	5'-ATCCAGAGTGACGCAGCAAATTCCAAACTCGAGTAAGCGTAGAGCCTCTCATCGCCTCAATAATGGACACGGTGGCTTAGT-3'
SNAP1	5'-TCGCTCTTTCCGCTTCTTCGCGGTCATTGTGCATCCTGACTGACCCTAAGGTGCGAACATCGCCCGCGTAAGTCCGTGTGTGCGAA-3'
SNAP3	5'-TCGCTCTTTCCGCTTCTTCGCGGTTAGGTACATCGTCTTCATTTCTCAAAGTCATTGTCTACACCGCGTAAGTCCGTGTGTGCGAA-3'
NS	5'-CCAGAGTGACGCAGCAAATTCCAAACTCGAGTAAGCGTAGAGCCTCTCATCGCCTCAATAATGGACACGGTGG-3'
scrSNAP1	5’-TCGCTCTTTCCGCTTCTTCGCGGGATCGCGTGGCCTATCGACCAAGCGCATCTATCTTCGAATCCGCGTAAGTCCGTGTGTGCGAA-3’
SNAP1.66	5'-CGCTTCTTCGCGGTCATTGTGCATCCTGACTGACCCTAAGGTGCGAACATCGCCCGCGTAAGTCCG-3'
SNAP1.50	5'-CGCGGTCATTGTGCATCCTGACTGACCCTAAGGTGCGAACATCGCCCGCG-3'
CD8	5'-CACAGTGACGCAGCAACAGAGGTGTAGAAGTACACGTGAACAAGCTTG-3'

Table S1.5. SNAP1 and SNAP3 binding kinetic values and fit parameters.

Aptamer	SARS-CoV-2 Protein	K_{on} 1/nM•s • 10^{-5}	K_{off} 1/s • 10^{-5}	K_D nM	χ^2	R^2
SNAP1	S1-His	0.71 ± 0.00	27.88 ± 0.03	39.32 ± 0.12	2.5844	0.9978
SNAP1	NTD-His	8.64 ± 0.22	521.30 ± 3.20	60.35 ± 1.61	0.0299	0.9740
SNAP1	S	19.53 ± 0.01	-	-	5.6620	0.9981
SNAP1	S-2P	0.16 ± 0.00	-	-	5.4186	0.9914
SNAP1	S-B.1.1.7	4.71 ± 0.18	-	-	0.1741	0.9410
SNAP3	S1-His	1.26 ± 0.01	96.77 ± 0.17	76.59 ± 0.45	0.5248	0.9969
SNAP3	NTD-His	24.44 ± 1.09	1302.00 ± 18.00	53.25 ± 2.49	0.0094	0.9509
SNAP1.66	S1-His	0.90 ± 0.00	28.53 ± 0.02	31.70 ± 0.10	0.8597	0.9990
SNAP1.66	NTD-His	5.01 ± 0.10	527.20 ± 1.90	105.30 ± 2.17	0.0452	0.9888
SNAP1.50	S1-His	0.80 ± 0.00	28.63 ± 0.02	35.77 ± 0.16	0.5739	0.9986
SNAP1.50	NTD-His	3.74 ± 0.11	508.10 ± 1.70	135.70 ± 4.10	0.0179	0.9903

Table S1.6. SARS-CoV-2 spike protein variants. Ranges are based on the SARS-CoV-2 S protein sequence (GenBank ID: QHD43416.1, PDB: P0DTC2)

Name	Range	Furin Site Mutations	Other Mutations	Tags	Trimerization Domain	Source
S	Val 16 – Pro 1213	R683A, R685A	none	His	Yes: not disclosed	ACROBiosystems
S-2P	Gln 14 – Lys 1230	R682S, R683G, R685G	K986P, V987P	His	Yes: C-terminal foldon	PDB: 6VXX
S-B1.1.7	Val 16 – Pro 1213	R683A, R685A	F817P, A892P, A899P, A942P, K986P, V987P; HV69-70del, Y144del, N501Y, A570D, D614G, P681H, T716I, S982A, D1118H	His	Yes: T4 fibritin	ACROBiosystems

Supplementary Figures

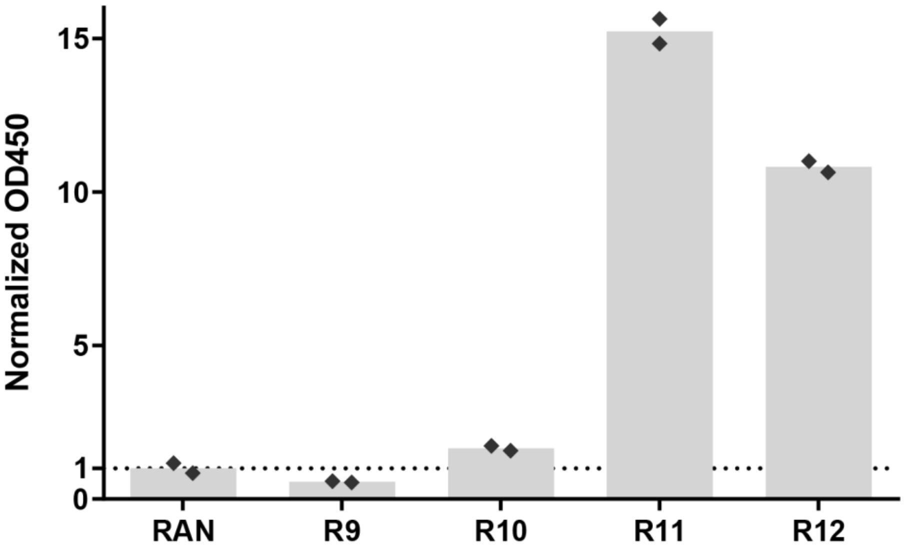

Figure S1.1. Binding of aptamer round pools to SARS-CoV-2 S monomer. Fluorescently-labeled aptamer pools (100 nM) were tested for binding to SARS-CoV-2 S monomer immobilized on high protein-binding plates. Background-subtracted data were normalized to the baseline OD450 value (dotted line) and two technical replicates were graphed (black diamonds).

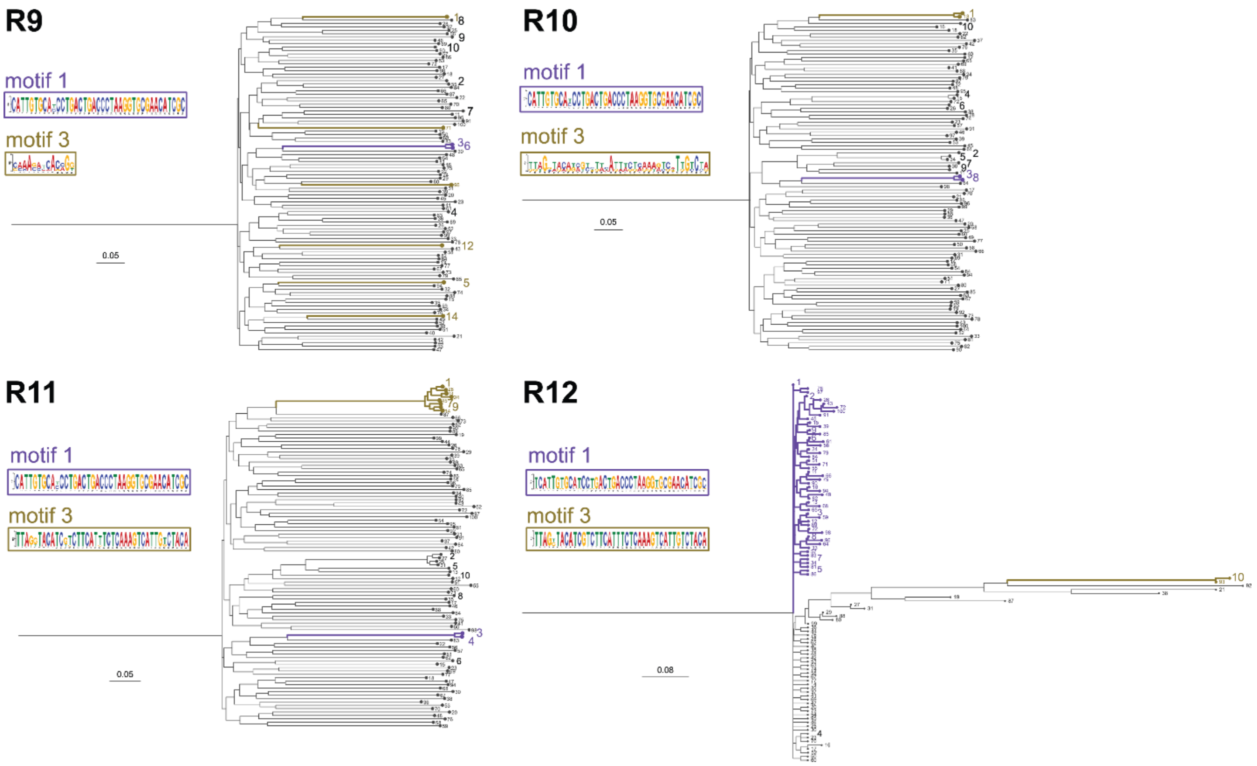

Figure S1.2. NGS of aptamer round pools reveals motifs enriched during SELEX. Each phylogenetic tree represents the top 100 sequences in each aptamer pool from round 9 to round 12. The number next to each node represents its rank in the top 100. Motif 1 (purple) and motif 3 (gold) are highlighted in each tree. Trees were generated with Simple Phylogeny (https://www.ebi.ac.uk/Tools/phylogeny/simple_phylogeny/) and FigTree (http://tree.bio.ed.ac.uk/software/figtree/) and binding motifs predicted with MEME analysis (MEME-suite.org).

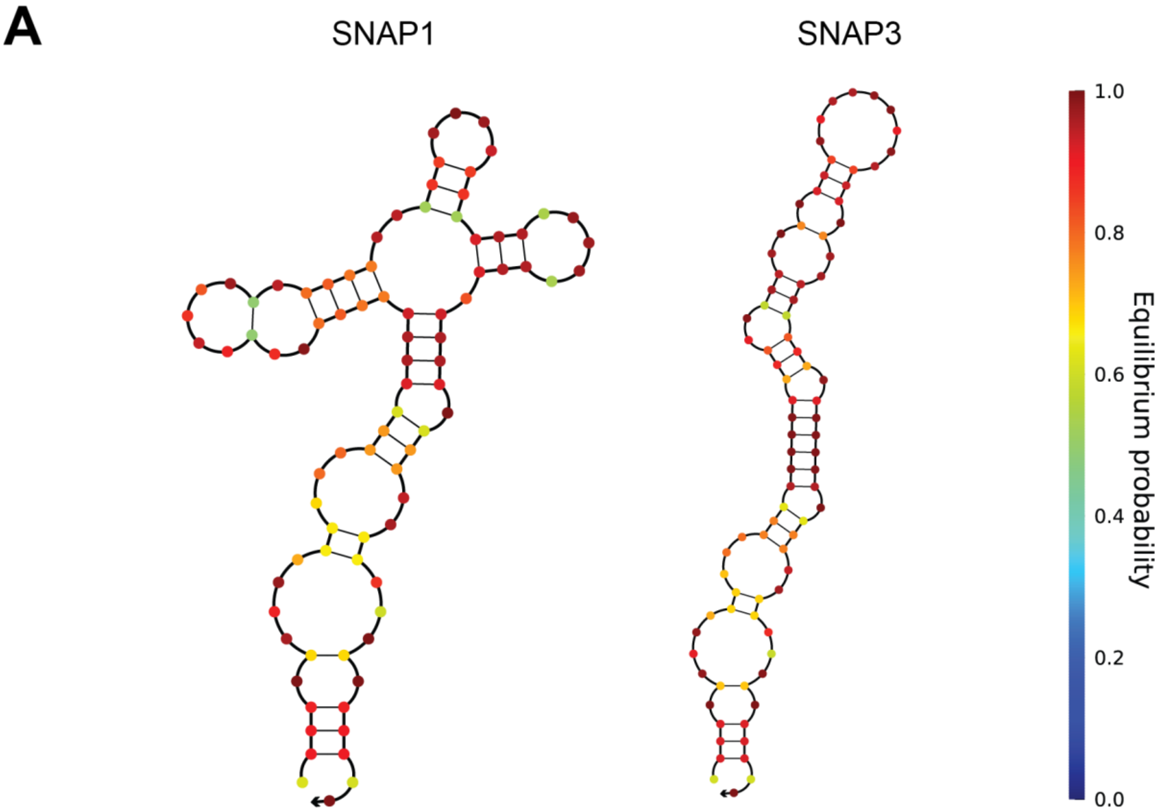

B

```
motif 1 (SNAP1)   TCATTGTGCATC--CTGACTGACCCTAAGGTGCGAACATCGC
                       ||.||||  ||...|..|.|.|||.......|..|
motif 3 (SNAP3)    TTAGGTACATCGTCTTCATTTCTCAAAGTCATTGTCTACA
```

Figure S1.3. Secondary structure prediction and alignment of SNAP1 and SNAP3 aptamers. A) Secondary structure was predicted using NUPACK (http://www.nupack.org/) for aptamers SNAP1 (left) and SNAP3 (right) with the following conditions: 4ºC, 0.137 M Na^+, 0.0055 M Mg^{++}. Arrows represent the 3' end of the aptamer. Nucleotides are color-coded by their equilibrium probability (see legend on right). **B)** Local alignment of motif 1 (40-bp random region of SNAP1) and motif 3 (40-bp random region of SNAP3) was conducted with EMBOSS Water (https://www.ebi.ac.uk/Tools/psa/).

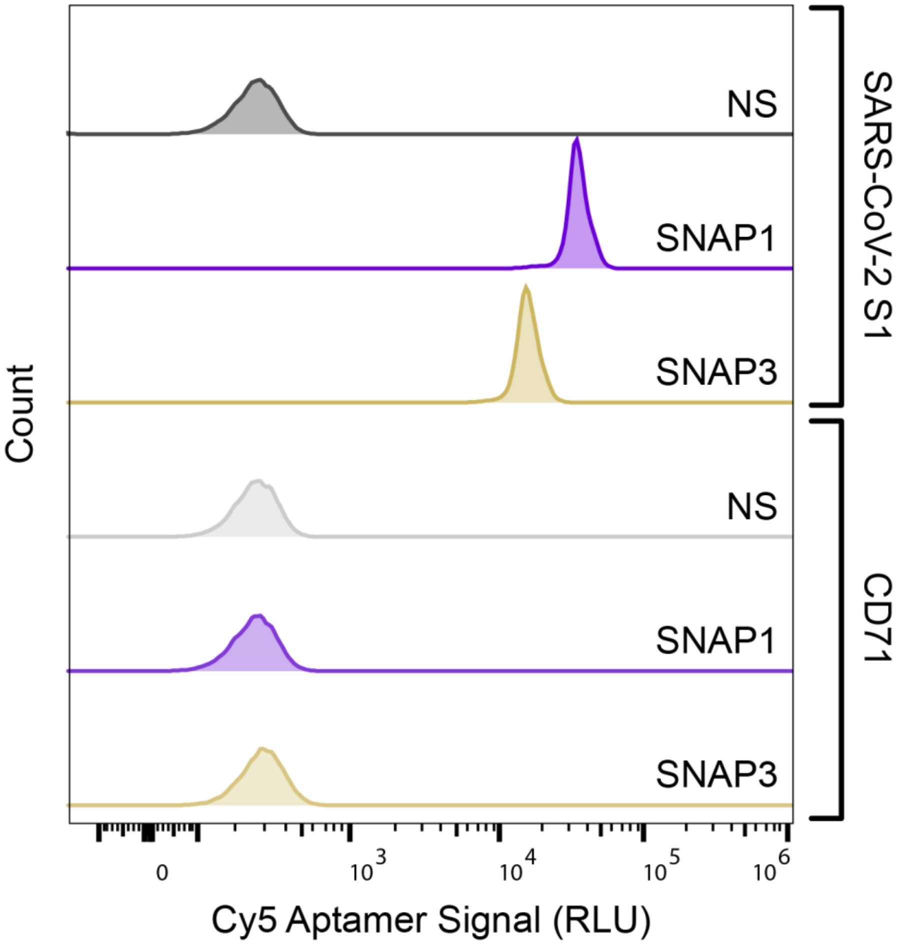

Figure S1.4. Aptamers SNAP1 and SNAP3 bind to SARS-CoV-2 S1. Protein G magnetic spheres coated with Fc-tagged SARS-CoV-2 S1 (400 nM) or human CD71 (200 nM) were incubated with 100 nM Cy5-labeled NS (gray), SNAP1 (purple), or SNAP3 (gold) aptamer. Fluorescence of spheres was measured by flow cytometry. Each histogram is one technical replicate.

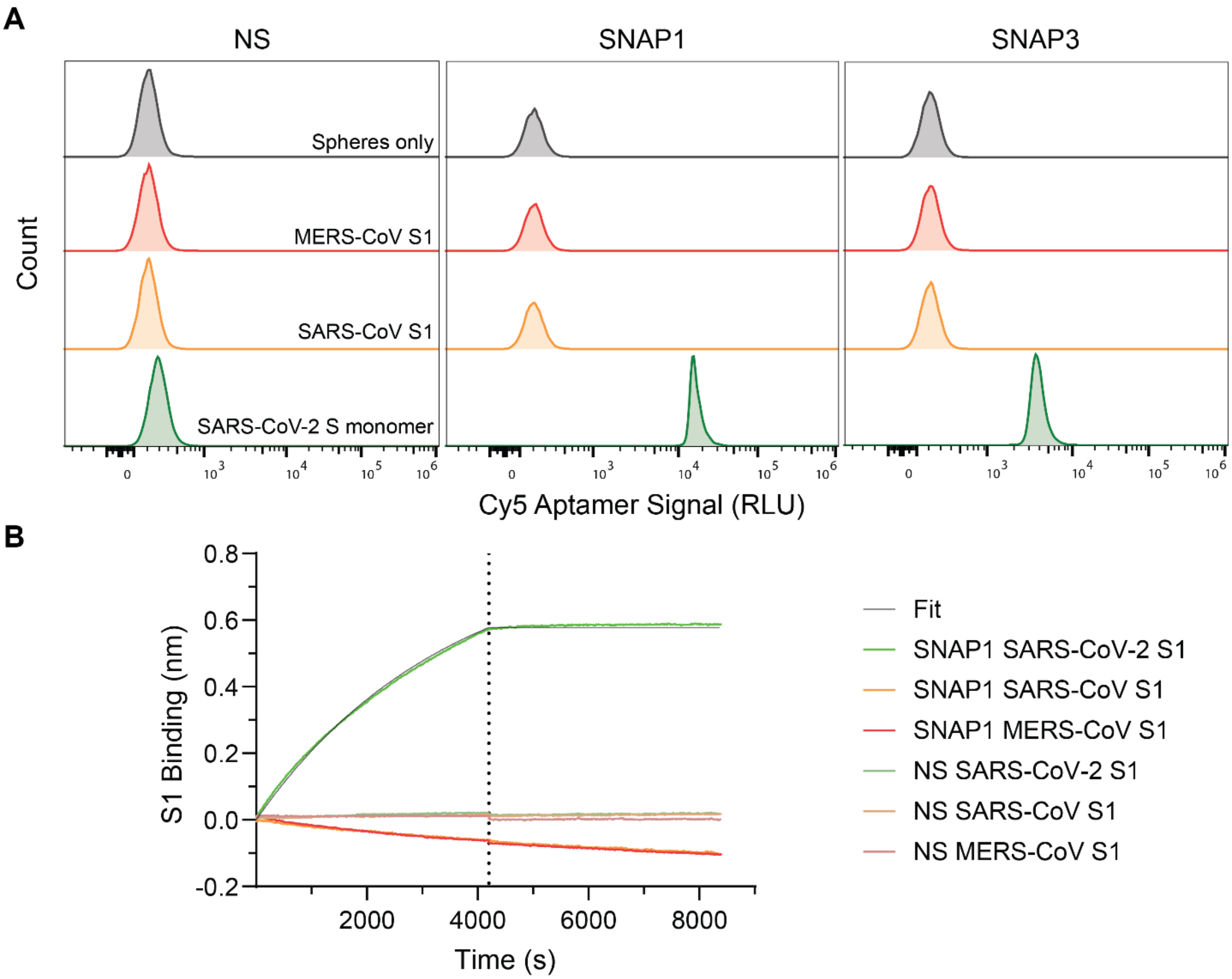

Figure S1.5. Aptamers SNAP1 and SNAP3 do not bind to SARS-CoV S1 or MERS-CoV S1. A) Magnetic spheres coated with 200 nM His-tagged proteins MERS-CoV S1 (red), SARS-CoV S1 (orange), or SARS-CoV-2 S monomer (dark green) were incubated with 100 nM Cy5-labeled NS (left), SNAP1 (center), or SNAP3 (right) aptamer. Fluorescence of spheres was measured by flow cytometry. Each histogram is one technical replicate. **B)** Kinetic parameters were measured through BLI. Biotinylated NS or SNAP1 aptamer were loaded on streptavidin biosensors, associated with 200 nM S1 of MERS-CoV (red), SARS-CoV (orange), or SARS-CoV-2 (light green) between 0-4200s, and then dissociation occurred between 4,200-8,400s.

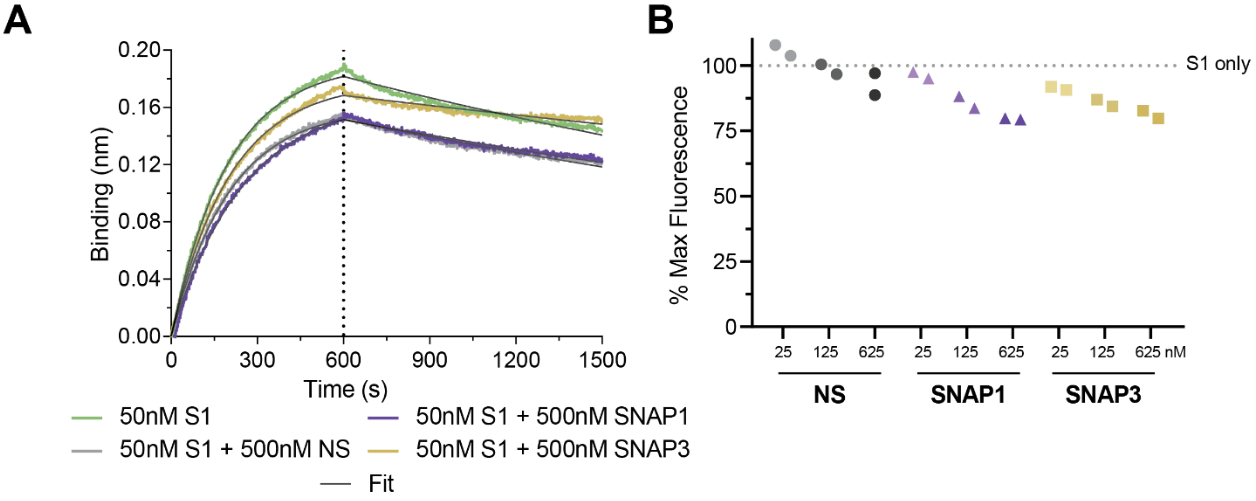

Figure S1.6. Aptamers SNAP1 and SNAP3 do not interfere with SARS CoV-2 S1 binding to ACE2. A) BLI experiment was conducted by loading His-tagged ACE2 onto Ni-NTA biosensors and testing association with 50 nM SARS-CoV-2 S1 alone and in the presence of 500 nM NS, SNAP1, or SNAP3 aptamer. Dotted line indicates switch from aptamer association (0-600s) to dissociation (600-1500s). Black lines indicate global fit of the kinetic data for a 1:1 binding model. **B)** Increasing concentrations of unlabeled NS, SNAP1, or SNAP3 aptamers were co-incubated with 25 nM Fc-labeled SARS-CoV-2 S1 for binding to ACE2-expressing HEK293T cells. Fluorescence of cells was measured by flow cytometry. Each point represents one technical replicate, with APC anti-Fc antibody fluorescence normalized to cells incubated only with 25 nM S1 (dotted line).

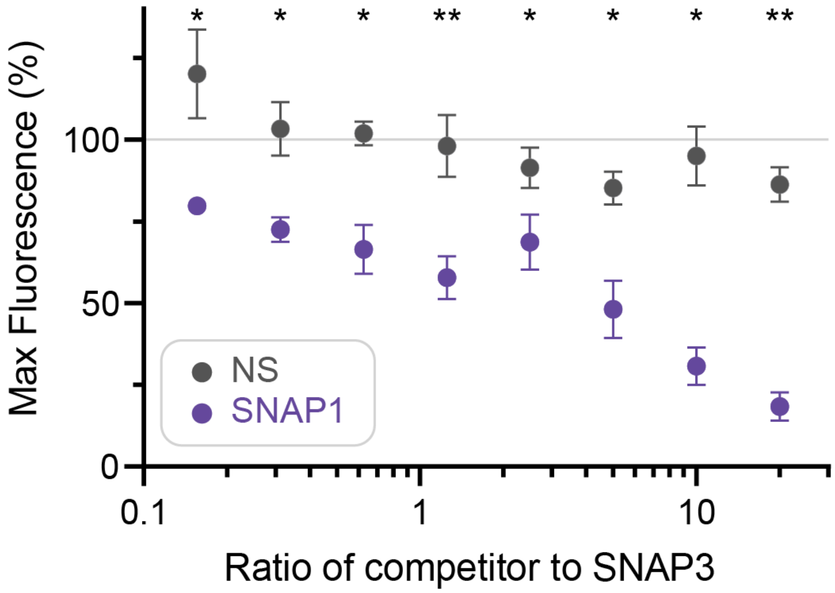

Figure S1.7. Aptamers SNAP1 and SNAP3 compete for the same binding site on SARS-CoV-2 S1. Protein G magnetic spheres immobilized with Fc-tagged SARS-CoV-2 S1 protein were incubated with 25 nM Cy5-labeled SNAP3 in the presence of increasing concentrations of unlabeled NS aptamer (dark gray) or SNAP1 (purple). Fluorescence of spheres was measured by flow cytometry. Each point is a mean calculated from three biological replicates normalized to no competitor (light gray), bars indicate s.d. Statistical comparison of NS to SNAP1 for each ratio was calculated by 2-way ANOVA, * denotes $p < 0.05$ and ** denotes $p < 0.01$.

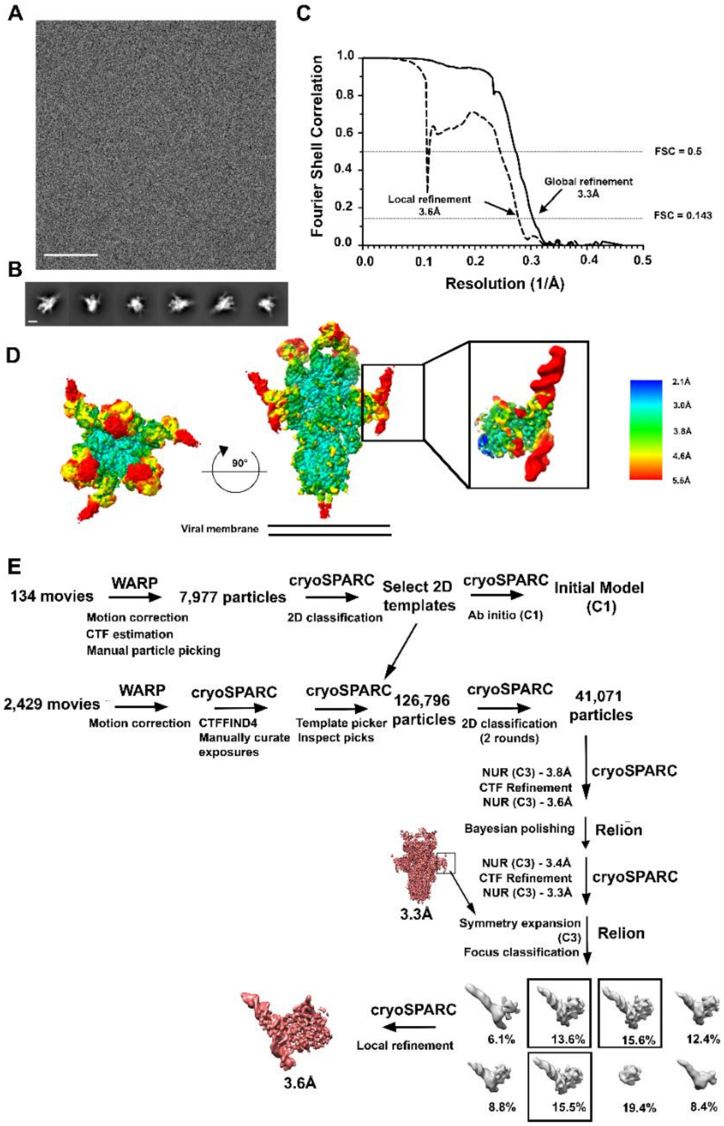

Figure S1.8. Cryo-EM characterization of the SNAP1/S/S2M11 complex. A) Representative micrograph. Scale bar, 100 nm. **B)** Reference-free 2D class averages. Scale bar, 100 Å. **C)** Gold-standard Fourier shell correlation (GSFSC) curves of the global map and the locally refined map of the NTD-bound aptamer. **D)** Unsharpened maps colored by local resolution in cryoSPARC of the SNAP1/S/S2M11 complex, as well as the locally-filtered map of the locally refined reconstruction of NTD and SNAP1 (inset). **E)** Cryo-EM data processing flow chart. Selected groups of particles at a given step are boxed.

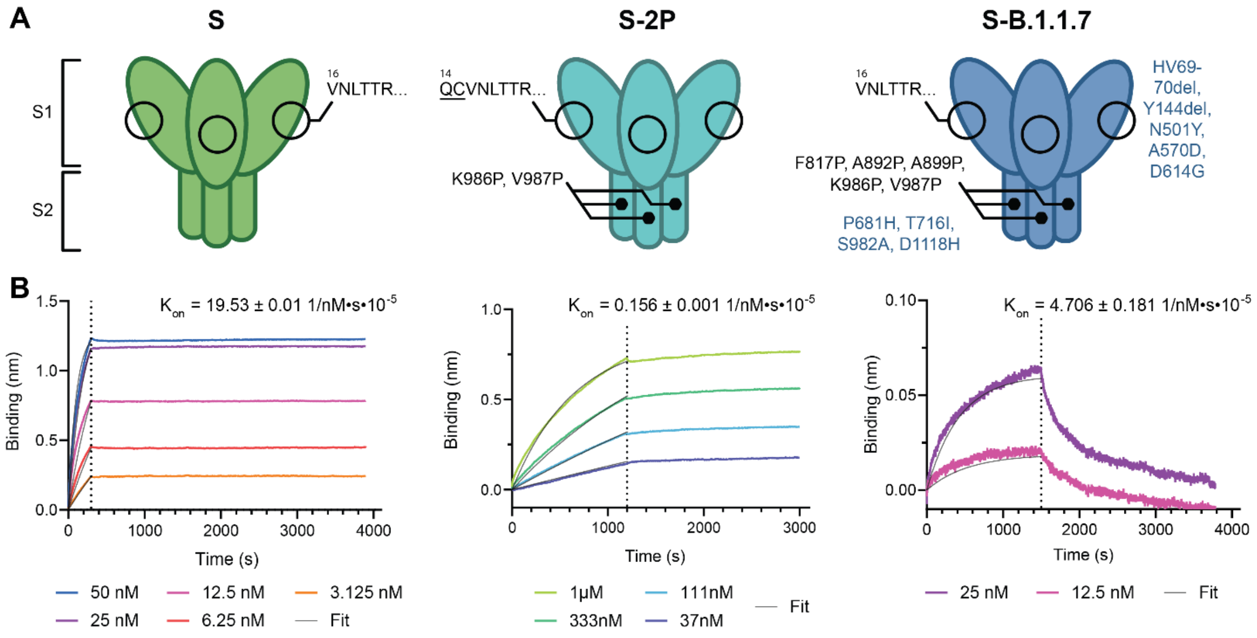

Figure S1.9. SNAP1 binds SARS-CoV-2 S trimer variants. A) Schematic that highlights important differences among S (left), S-2P (middle), and S-B.1.1.7 (right), including predicted N-terminal residue identities and mutations. **B)** Corresponding BLI measurements of binding kinetics. Biotinylated SNAP1 was loaded on streptavidin biosensors and associated with variants of SARS-CoV-2 S trimer. Each graph contains replicate experiments with different concentrations of proteins as denoted in the legend (bottom). Dotted lines indicate switch from analyte association to dissociation. K_{on} values (mean±s.d., n= 2-6) were determined from a global fit (dark gray line) of the kinetic data at various concentration of proteins for a 1:1 binding model.

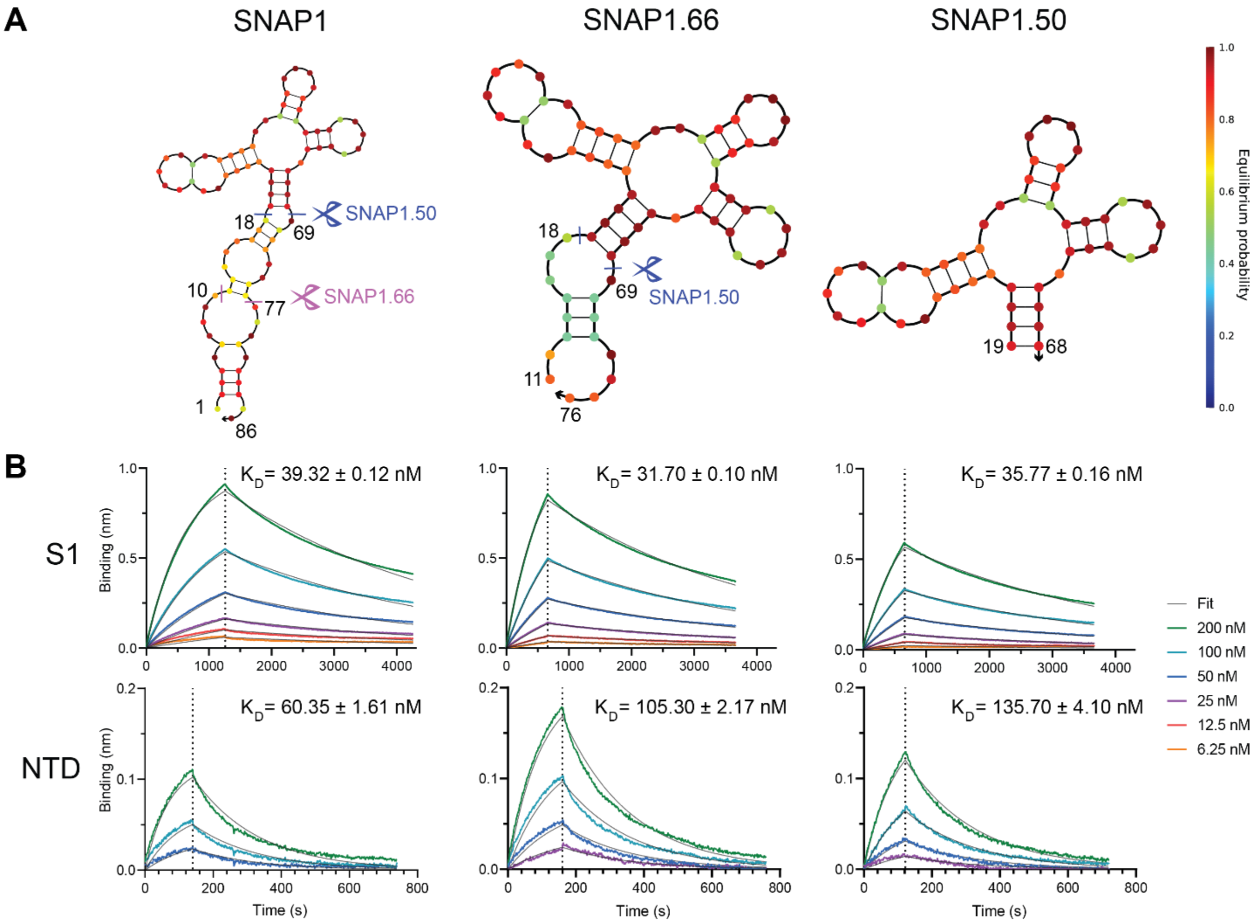

Figure S1.10. Truncations of SNAP1 have similar binding affinities as whole SNAP1. A) Secondary structure was predicted using NUPACK (http://www.nupack.org/) for SNAP1 (left), SNAP1.66 (center), and SNAP1.50 (right) with the following conditions: 4ºC, 0.137 M Na^+, 0.0055 M Mg^{++}. Arrows represent the 3' end of the aptamer. Nucleotides are color-coded by their equilibrium probability (see legend on right). **B)** Kinetic and binding equilibrium constants were measured by BLI. Biotinylated SNAP1 (left), SNAP1.66 (center) or SNAP1.50 (right) was loaded on streptavidin biosensors and associated with SARS-CoV-2 S1 domain (upper row) or NTD (lower row). Each graph contains different concentrations of proteins as denoted in the legend (right). Dotted lines indicate switch from analyte association to dissociation. K_D values (mean±s.d., n=6) were determined from a global fit (dark gray line) of the kinetic data at various concentration of proteins for a 1:1 binding model.

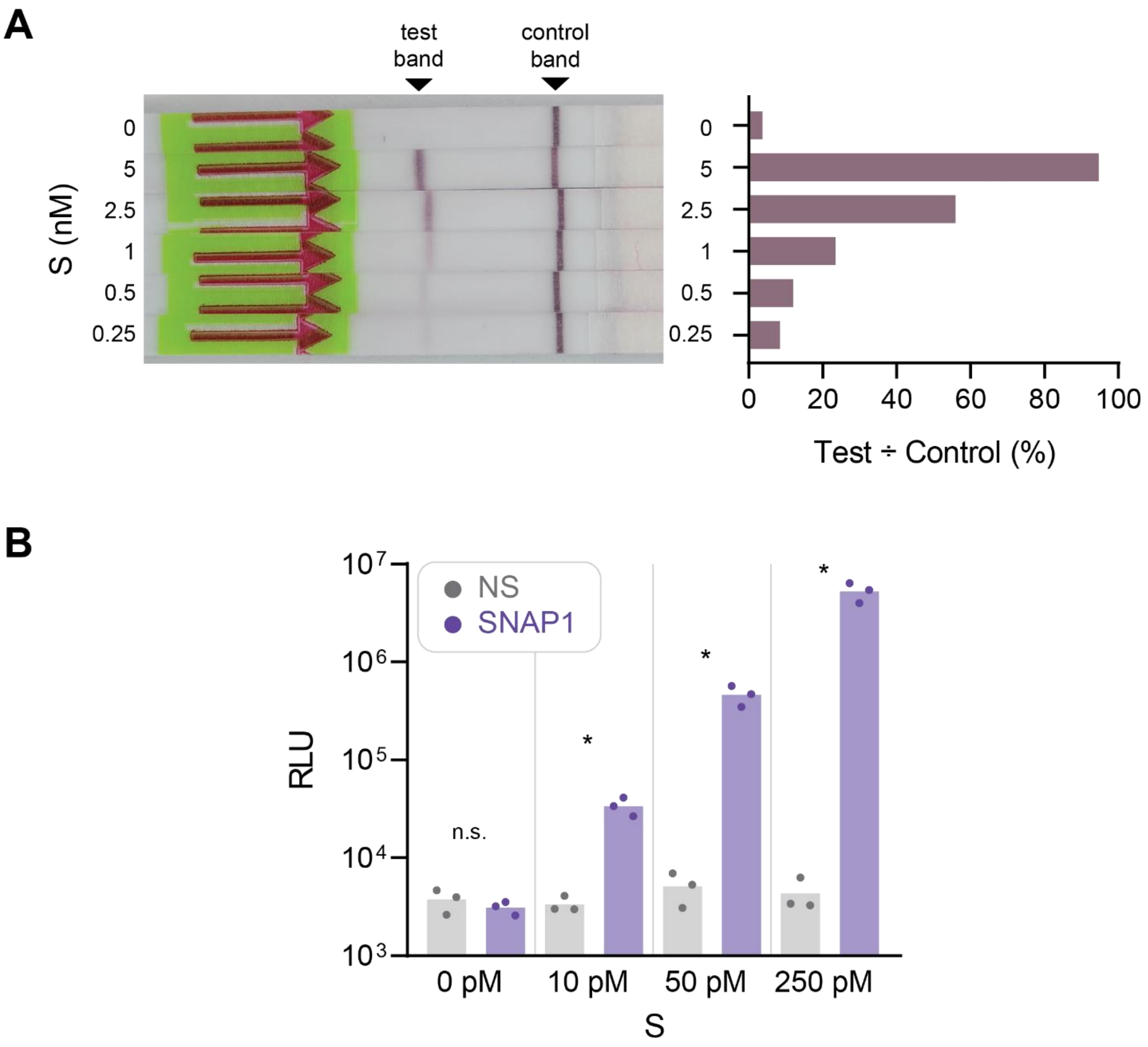

Figure S1.11. Aptamer-based detection of SARS-CoV-2 S protein. A) HybriDetect LFA strips were dipped in solutions of S protein incubated with SNAP1.50. Left: image of developed HybriDetect LFA test strips. Right: quantification of band intensity. B) ELISA assay using NS-biotin or SNAP1-biotin as capture agents to detect various concentrations of SARS-CoV-2 using anti-S HRP antibody for detection. Bar graph shows mean (bar) of three replicates. Statistical comparison of NS to SNAP1 was determined by two-way ANOVA, * denotes $p < 0.05$ and n.s. denotes no significance.

Chapter 2

Aptamer sandwich lateral flow assay (AptaFlow) for antibody-free SARS-CoV-2 detection

Adapted from publication in Analytical Chemistry

Lucy F. Yang, Nataly Kacherovsky, Nuttada Panpradist, Ruixuan Wan, Joey Liang, Stephen J. Salipante, Suzie H. Pun

Abstract

The COVID-19 pandemic is among the greatest health and socioeconomic crisis in recent history. Although COVID-19 vaccines are being distributed, there remains a need for rapid testing to limit viral spread from infected individuals. We previously identified SARS-CoV-2 spike protein N-terminal domain (NTD) binding DNA aptamer 1 (SNAP1) for detection of SARS-CoV-2 virus by aptamer-antibody sandwich enzyme-linked immunoassay (ELISA) and lateral flow assay (LFA). In this work, we identify a new aptamer that also binds at the NTD, named SARS-CoV-2 spike protein NTD-binding DNA aptamer 4 (SNAP4). SNAP4 binds with high affinity (< 30 nM) for SARS-CoV-2 spike protein, a 2-fold improvement over SNAP1. Furthermore, we utilized both SNAP1 and SNAP4 in an aptamer sandwich LFA (AptaFlow), which detected SARS-CoV-2 UV-inactivated virus at concentrations as low as 10^6 copies/mL. AptaFlow costs <\$1 per test to produce, provides results in <1 hour, and detects SARS-CoV-2 at concentrations that indicate higher viral loads and high probability of con-tagious transmission. AptaFlow is a potential approach for a low-cost, convenient antigen test to aid the control of the COVID-19 pandemic.

Introduction

The coronavirus disease 2019 (COVID-19) pandemic is one of the largest public health threats to date. Although COVID-19 vaccines have been authorized and administered to almost 4 billion people worldwide, vaccine dissemination remains a challenge[1] and new variants of concern (VOCs) with increased transmissibility, severity, or vaccine escape capabilities develop. Preventative measures, including frequent testing, are needed in addition to vaccines to control COVID-19.

Among COVID-19 diagnostics, rapid antigen tests for SARS-CoV-2 are important tools for curbing the pandemic[2]. Rapid antigen tests are inexpensive to produce and provide point-of-care results. Users can make better-informed risk decisions through more frequent testing, even if they are less sensitive[3,4]. In this manner, exposed individuals can perform point-of-care tests more frequently compared to molecular tests, which often require visiting a facility, time-consuming off-site processing, or high cost.

Nucleic acid aptamers are short sequences of RNA or DNA that specifically bind target molecules and offer unique advantages over antibodies as molecular recognition agents for SARS-CoV-2. Aptamers can achieve specific binding to target molecules with affinities similar to antibodies[5,6]. Compared to protein antibodies, DNA aptamers are less expensive to synthesize, more stable, and more scalable for production. Due to these features, nucleic acid aptamers have been applied to a variety of fields, including therapeutics[7] and diagnostics[8]. A library selection method called systematic evolution of ligands by exponential enrichment (SELEX) is used to discover aptamer sequences[9–11]. A wide variety of selection targets can be used in SELEX, including whole cells[12] and proteins[13], to yield highly specific and tight-binding aptamers. The spike (S) protein of

SARS-CoV-2 is displayed on the viral surface and is therefore an attractive detection target for intact virus. The S protein is a homotrimer, and each monomer contains subunit 1 (S1) and subunit 2 (S2). Within S1, there are two distinct regions: the receptor-binding domain (RBD) and the N-terminal domain (NTD)[14,15]. Several aptamers that bind SARS-CoV-2 S protein have been reported[16–18], including the SARS-CoV-2 spike protein NTD-binding DNA aptamer 1 (SNAP1)[16].

Lateral flow assays (LFAs) are one type of diagnostic device that can provide rapid, point-of-care results. LFAs are not only fast, user-friendly, and convenient to use, but also are inexpensive compared to lab tests. There are many commercial LFAs that test for diseases such as influenza, malaria, and HIV[19]. In addition to those applications, LFAs are also being applied to other areas, such as HIV drug resistance testing[20–22], cancer biomarker screening[23], and now COVID-19 testing[24,25]. Eight over-the-counter LFAs for COVID-19 were under emergency use authorization by the FDA as of November 2021[2]. These LFAs use protein antibodies to capture and detect nucleocapsid protein, which is highly conserved and abundant in samples[26]. However, nucleocapsid detection requires lysing the virus. Typically, patient swab samples are incubated in extraction buffer to release nucleocapsid, then used in testing assays. To streamline this process and eliminate this step, one strategy is to use a capture and detection agent that binds S protein instead of nucleocapsid protein. The S protein is also highly mutated among SARS-CoV-2 variants, so a multiplexed LFA that detects specific mutations in S protein can be used to identify variants. In addition, replacing the antibodies with DNA aptamers could expedite to-scale production and reduce the cost of manufacturing[27,28].

Previously, we demonstrated that SNAP1 binds to wild-type SARS-CoV-2 S protein with high affinity (< 80 nM) and can detect UV-inactivated SARS-CoV-2 virus in a proof-of-concept LFA[16]. However, SNAP1 did not bind very well to S-2P, a stabilized form of S protein. In this study, we implemented a hybrid SELEX strategy using S-2P expressed on cells and as purified proteins as selection targets. S-2P contains two stabilizing proline mutations and has been shown to better reflect its authentic topology in Cryo-EM studies. Therefore SELEX utilizing S-2P may yield aptamers that bind more tightly to SARS-CoV-2 virus[29,30]. We discovered a new sequence named SARS-CoV-2 spike protein NTD-binding DNA aptamer 4 (SNAP4), which binds specifically to the NTD of S protein with < 30 nM affinity. We employed SNAP4 and SNAP1 as capture and detection agents, respectively, in an aptamer sandwich LFA (AptaFlow). AptaFlow detected SARS-CoV-2 spike protein at 250 pM as well as UV-inactivated virus at 10^6 copies/mL, which recent findings suggest is sufficient to detect contagious users with high viral load [31–33]. AptaFlow takes <1 hour to use and costs under $1 per test, demonstrating its potential as an accessible COVID-19 rapid test for detecting infectious individuals.

Experimental Section

Oligonucleotides

All oligonucleotides were synthesized by Integrated DNA Technologies. The ssDNA library used in the protein SELEX process was 5’-ATCCAGAGTGACGCAGCA-N52-TGGACACGGTGGCTTAGT-3’. The forward primer for amplification was FAM-ATCCAGAGTGACGCAG, and the reverse primer for amplification was 5’-Biotin-GACACGGTGGCTTAGT-3’. Oligonucleotide sequences are listed in Table S2. Modifications to oligonucleotides included: FITC (5’- FITC – sequence – 3’), biotin (5’-

biotin – iSp18 spacer – sequence – 3’), Cy5 (5’ – Cy5 – sequence – 3’), and thiol (5’- thiol – sequence – 3’). All aptamer pools and aptamers were annealed before use in SELEX, binding, characterization, and other studies. Aptamers were annealed by diluting to 1 - 10 µM in SELEX WB (see buffers below), heating at 95°C for 5 min, and snap-cooling on ice for at least 10 min.

Buffers

SELEX wash buffer (SELEX WB) contains 4.5 g/L glucose, 0.1 g/L $CaCl_2$, 0.2 g/L KCl, 0.2 g/L KH_2PO_4, 0.1 g/L $MgCl_2{\bullet}6H_2O$, 8 g/L NaCl, 2.1716 g/L Na_2HPO_4, and 5mM $MgCl_2$. The buffer is filtered through a 0.22µm sterile filter and stored at 4°C. For binding buffers, yeast tRNA (Invitrogen) (tRNA) and salmon sperm DNA (Invitrogen) (SS DNA) are added to a final concentration of 0.1 mg/mL. Additionally, MACS BSA 10% stock solution (Miltenyi Biotec) is added to 0.1-2% final concentration depending on the experiment.

Generation of HEK293_S-2P and culturing conditions

The HEK293 cell line was cultured in 1X DMEM (Gibco) containing 10% FBS. To generate the S-2P expressing cell line, HEK293 cells were nucleofected with SpeI (NEB) linearized plasmid SARS-CoV-2-FL_pseudo_2P_pcDNA3.1[29] using Cell Line Nucleofector™ Kit V (Lonza) according to manufacturer’s instructions. After 24 hours, cells were subjected to G418 selection for 2 weeks to achieve stable integration. To enrich for high expressers, selected cells were incubated with 10 nM of biotinylated SNAP1 aptamer and anti-biotin magnetic beads for 20 min then applied onto an MS column (Miltenyi Biotec). Expression was monitored with SARS-CoV-2 Spike Human anti-SARS-CoV-2, Alexa Fluor 488 (Novus Biologicals cat. no. NBP290980AF488) by flow cytometry.

Recombinant proteins

SARS-CoV-2 S protein trimer S-2P was kindly provided by the Institute of Protein Design (IPD) at the University of Washington. SARS-CoV-2 S protein S1 domain (ACROBiosystems S1N-C5255), SARS-CoV-2 S protein trimer (ACROBiosystems SPN-C52H8), SARS-CoV-2 S protein S1 NTD (ACROBiosystems S1D-C52H6), SARS-CoV-2 S protein RBD (ACROBiosystems SPD-C5255), CD8 protein (Sino Biologic 10980-H08H) were purchased in lyophilized form. All proteins contained His-tag. These proteins were reconstituted, aliquoted, and stored according to manufacturer's recommendations. All proteins contained His-tag.

Viruses

Inactivated SARS-CoV-2 virus samples at known concentrations were kindly provided by the NIH RADx-Radical Data Coordination Center (DCC) at the University of California San Diego and BEI Resources. UV-inactivated SARS-CoV-2 Isolate USA-WA1/2020 was measured to be at 4.5 x 10^7 copies of ORF1a/mL, with a limit of detection of 10^{-7} on Roche Cobas 6800/8800 (qPCR) when tested immediately, of 10^{-2} on BD Veritor (antigen testing) when tested immediately. Heat-inactivated SARS-CoV-2 Isolate USA-WA1/2020 was measured to be at 4.9 x 10^9 copies of ORF1a/mL, with a limit of detection of 10^{-9} on Roche Cobas 6800/8800 (qPCR) when tested immediately, of 10^{-2} on BD Veritor (antigen testing) when tested immediately. Virus samples used in this study have undergone at least 1 freeze-thaw cycle.

Protein-SELEX

The protocol was based on the guidelines outlined by Wang et al.[34] and is outlined in Fig. 1. Experimental conditions for 10 rounds of SELEX are summarized in Table S1. For rounds 1-6, partitioning of bound and unbound aptamers was achieved by centrifugation of cells at 500 *x g* for 3 min. For rounds 7-10, aptamers were partitioned by Dynabeads His-tag isolation & Pulldown (Novex by Life Technologies) on a rack magnet. Aptamers were amplified with Phusion® High-Fidelity DNA Polymerase (NEB). Annealing, strand separation, and composition of buffers were described previously[12].

Next-generation sequencing (NGS) and data analysis

The DNA pools from SELEX rounds were PCR amplified with barcoded primers described in Table S3 using the MiSeq Reagent Kit v2 (300-cycles) (Illumina) and MiSeq System (Illumina) per manufacturer's protocol. Sequence reads were analyzed as previously described[16]. Secondary structure was predicted with NUPACK[35].

Aptamer binding assay with magnetic spheres

Streptavidin or Protein G Sphero™ magnetic spheres (Spherotech) were used in binding assays. Streptavidin spheres were further modified with biotin anti-6-His epitope tag antibody (Biolegend cat. no. 906103). These spheres were used to immobilize SARS-CoV-2 S1-His and SARS-CoV-2 S1-Fc proteins, respectively. Individual Cy5 labeled aptamers were incubated with SARS-CoV-2 S1 spheres in binding buffer for 30 min at room temperature, washed twice with wash buffer (0.1% BSA, 0.01% Tween-20 SELEX WB), and analyzed by flow cytometry (Attune NxT, Invitrogen).

Biolayer interferometry (BLI)

Studies were performed with an Octet Red96 machine (Sartorius) at 25^{o}C and 1,000 rpm sample agitation. Pre-soaked streptavidin (SA) sensors were rinsed in 1% BSA, 0.1 mg/mL tRNA, 0.1 mg/mL SS DNA, 0.01% Tween-20 SELEX WB (“diluent”) for 100s. Next, tips were loaded with 50 nM biotinylated aptamer until reaching a 0.5 nm signal threshold. Subsequently, tips were rinsed in diluent for 100 s then baselined in diluent for another 100 s. After association with protein of interest diluted to the desired concentration, sensor tips were returned to the baseline diluent well for dissociation. Data were analyzed with Octet Data Analysis 9.0 (Sartorius). Kinetic values were determined from a global fit of several curves generated from serial dilutions of the protein in a 1:1 or 1:2 binding model.

ELISA

Wells of a white streptavidin-coated 96-well plate (Thermo Fisher Scientific) were washed and blotted three times with SELEX WB then incubated with 50 nM biotinylated NS or SNAP1 aptamer at 4^{o}C for 30 min. After three washes with wash buffer (0.1% Tween-20 2% BSA SELEX), wells were incubated with blocking buffer (5% BSA, 1:100 biotin blocking solution (Vector Laboratories), 0.1 mg/mL tRNA, 0.1 mg/mL SS DNA, 0.1% Tween-20 SELEX WB) for 1.5 h at room temperature. Subsequently, the wells were incubated with S protein, UV-inactivated SARS-CoV-2 virus, or lentivirus in binding buffer (2% BSA, 0.1 mg/mL tRNA, 0.1 mg/mL SS DNA, 0.1% Tween-20 SELEX WB) for 30 min at room temperature. Then wells were washed four times before incubation with an anti-SARS-CoV-2 antibody with HRP (Novus Biologicals cat. no. NBP2-90980H). Lastly, wells were washed six times. All steps use 100 µL of the solution, except washing (200 µL of solution.) For wash steps, the plate is flicked over a sink then blotted dry. Ice-cold ELISA Femto Substrate (Thermo Fisher Scientific) was added, and the plate luminescence was immediately measured by Infinite 200 PRO plate reader (Tecan) with 250 nm integration time and automatic attenuation.

Gold nanoparticle synthesis

Glassware and stir bar were cleaned thoroughly with aqua regia, rinsed with deionized water, and incubated at 80^{o}C overnight. 50 mL 0.01% $HAuCl_4$ (Salt Lake Metals) was heated to boiling in a 3-neck round-bottom flask with condenser. Then, 1 mL 1% (34mM) trisodium citrate was added. The solution was incubated for 15 min, gradually cooled to RT over several hours, and stored at 4^{o}C shielded from light. Nanoparticles were not used until at least 24 h after completion of synthesis and always sonicated before use. Particle size was checked by dynamic light scattering (DLS).

Gold nanoparticle and aptamer conjugation

Protocol adapted from Liu and Lu[36]. Glass scintillation vials were incubated with 10 M NaOH for 1 h at RT and rinsed thoroughly with deionized water. 67.5 µL thiolated aptamers were annealed at 10 µM in SELEX WB, then incubated with 6.75 µL 500 mM acetate buffer (pH 5.2) and 10.13 µL 10 mM freshly prepared TCEP for 1 h at RT. 3 mL gold nanoparticles were added to the glass vial, then TCEP-treated aptamers were added dropwise. The solution was incubated at RT for at least 24 h with rocking shielded from light. Afterwards, 30 µL 500 mM Tris acetate (pH 8.2) and 300 µL 1M NaCl were added to the solution before incubation at RT for at least 24 h, shielded from light. Aptamer-conjugated gold nanoparticles were stored at 4^{o}C shielded from light.

LFA dipstick manufacturing

The protocol was adapted from previous work[21,22]. Nitrocellulose membrane (Sartorius, 1UN95ER050030—B) assembled to a backing card (DCN, MIBA-020- 60mm) were striped with test and control lines. Test line: 2 mg/mL polystreptavidin R (pSA) (Eagle Biosciences, # 10 120 030) in DPBS and control line: 0.6 mg/mL S-2P protein were striped at 1µL/cm (Biodot, ZX1010), incubated at 37^{o}C for 30 min, and stored in the desiccated overnight at RT. Then, the card was attached to the absorbent pad (GE, 8117-2250) and sliced into 45 mm-width strips by the strip cutter (Kinbio, ZQ2000). Ponceau stain was used to stain the immobilized proteins to verify successful striped proteins as described previously[20]. Strips were stored in foil bags with desiccant at 4^{o}C until use.

Antibody-free aptamer LFA

Binding buffer (1% BSA, 0.1 mg/mL tRNA, 0.1 mg/mL SS DNA, 0.01% Tween-20), 25 nM biotinylated aptamer, and 50 µL aptamer-functionalized gold nanoparticles were prepared, then analyte was added to a total volume of 100 µL. The solution was incubated at RT for 20 min with rocking. Then, a lateral flow device was dipped into the solution for 15-20 min (entire volume absorbed). Next, the lateral flow devices are dipped in 50 µL SELEX WB for 5 min (partial volume absorbed). Lastly, the lateral flow devices were dipped in 50 µL GoldEnhance (Nanoprobes) and developed over 10 min (entire volume absorbed). Test strips were photographed with a Galaxy S20 mobile phone (Samsung) and quantified on ImageJ. For each strip, the average pixel value in the control band, test band, and background (blank area between bands) was calculated. The control and test band values were background-subtracted, then the ratio of test band:control band value was used. The LOD was determined from the lowest concentration of sample that was significantly higher than the negative control.

Nasal swab samples

Nasal swabs were obtained from healthy human volunteers. Nylon flocked dry swabs (Copan cat no 1C058S01) were fully inserted into a nostril and rotated in a circle 10 times, then repeated with the other nostril. Next, the swab was dipped into 1 mL SELEX WB, swirled vigorously, and spun at 8000 x g for 10 min.

Results & Discussion

SELEX Strategy

We designed a selection strategy that combined cell and protein SELEX (Fig. 2.1). For the first six rounds, we performed cell SELEX using S-2P-expressing cell line (HEK293_S-2P) as the binding target. Wild-type HEK293 cells were used in negative selection to reduce the binding of non-specific sequences. We hypothesized that displaying S-2P on the cell membrane would provide a more authentic context for aptamer panning because S protein is expressed on a lipid bilayer in SARS-CoV-2 virus. The HEK293 cell line was chosen since it is commonly used for production of pseudovirus[34]. For rounds 7 to 10, we performed protein SELEX using S-2P recombinant protein as the target. We hypothesized that these rounds would select against aptamers that bind to proteins other than S-2P expressed on the cell surface. We increased selection pressure in sequential rounds of selection by tuning concentrations of aptamer pools, competitors, and ratios of cells and proteins used for positive and negative selection according to Table S1. After observing increased binding of libraries from rounds 5 and 6 to HEK293_S-2P cells, we sequenced libraries from these rounds and identified one enriched sequence, A1, that bound the S-2P-expressing cells (Fig. S2.1). We continued selection through protein SELEX, and characterized the resulting libraries by NGS analysis. We identified three additional candidate aptamers (A2, A3, and A4) as potential S-2P binders based on their prevalence (Table S2.2).

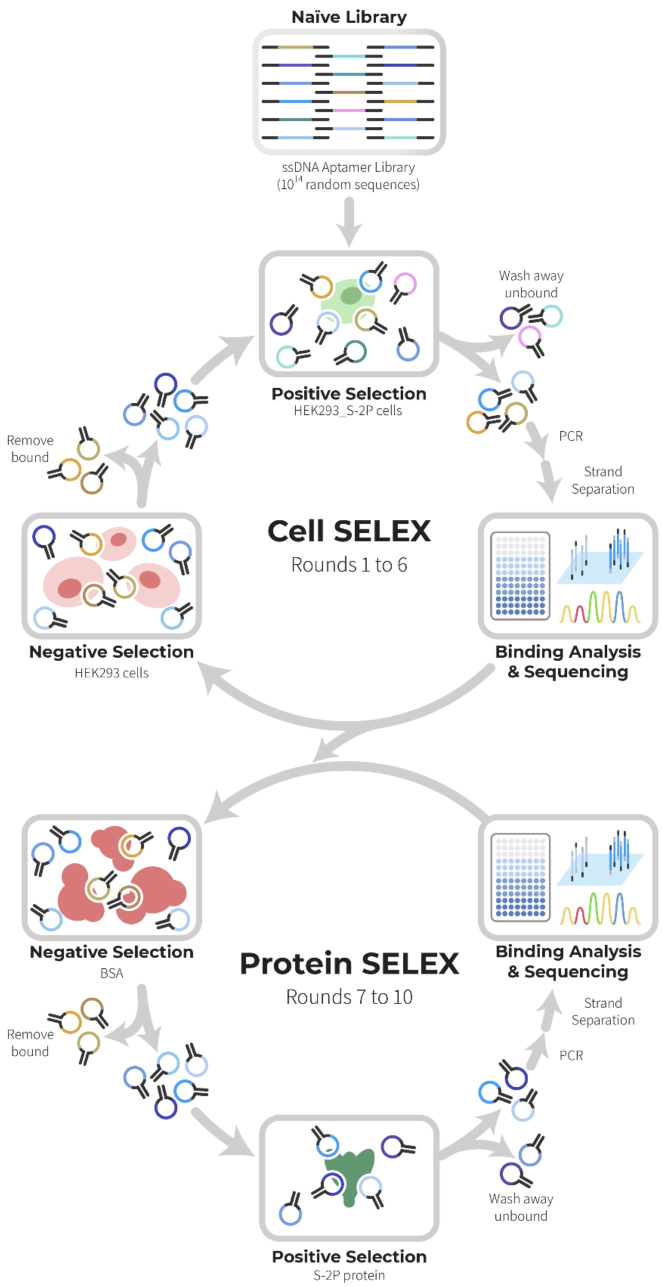

Figure 2.1. A naïve aptamer library is enriched for S-2P binders by cell SELEX then protein SELEX. In cell SELEX, HEK293_S-2P cells are used for positive selection and HEK293 cells are used for negative selection. In protein SELEX, S-2P recombinant protein is used for positive selection and bovine serum albumin (BSA) is used for negative selection. Aptamer pools are evaluated for binding to targets and sequenced.

Aptamer binding characterization

We screened the four candidate aptamers by aptamer-antibody sandwich ELISA and found that A4 aptamer bound S-2P recombinant protein with the highest signal (Fig. S2.2). To further characterize A4 aptamer, we used flow cytometry to quantify binding of the aptamer to HEK293_S-2P cells, which were used for positive selection in rounds 1-6 (Fig. 2A). We measured an apparent K_D of 7.87 nM by fitting a binding curve to fluorescence measured at different A4 concentrations. Next, we monitored binding of A4 aptamer to immobilized S-2P protein using biolayer interferometry (Fig. 2.2B). We measured an on-rate of $2.73 \pm 0.01 \times 10^{-5}$ nM^{-1} s^{-1} for A4 aptamer and S-2P. The off-rate was too low to measure, which may be due to multiple binding sites on trimeric S protein. Next, we narrowed down the binding location of A4 aptamer on S protein by measuring its binding affinity to S1 protein by BLI (Fig. 2.2C, top left). The data best fit a 1:2 heterogenous binding model, suggesting that A4 aptamer may bind to more than one site on the S protein. The K_{D1} was 21.2 ± 0.0 nM and the K_{D2} was 89.8 ± 0.1 nM for A4 binding to S1 protein. We also tested binding to SARS-CoV-2 RBD by ELISA (Fig. S2.2) and BLI (data not shown) and did not observe binding. Additionally, we measured the binding kinetics of A4 aptamer to the NTD of S protein (Fig. 2.2C, bottom left). A4 aptamer bound NTD in a 1:1 manner with K_D of 28.1 ± 0.2 nM. Notably, A4 aptamer's binding affinity for NTD is more than twice that of SNAP1 (K_D = 60.4 ± 1.6 nM)[16]. These data together demonstrate that A4 aptamer binds S-2P tightly at the NTD. Thus, we renamed A4 to SARS-CoV-2 spike protein NTD-binding DNA aptamer 4 (SNAP4).

Due to discovering several NTD-binding aptamers (SNAP1, SNAP3, and now SNAP4), we asked whether other S-binding aptamers also bound NTD[12], including SP6.51

aptamer. SP6.51 was previously reported to bind the S protein in an RBD-independent manner[17]. We found that SP6.51 binds to S1 and NTD by BLI (Fig. S2.3). We hypothesize that multiple independent SELEX processes have yielded NTD-binding aptamers because the NTD is the most exposed part of the S protein. The NTD is the outermost region and exposed on all three monomers, unlike the RBD that can switch between a closed and open conformation and only 1 or 2 RBDs per spike protein are open[14,35].

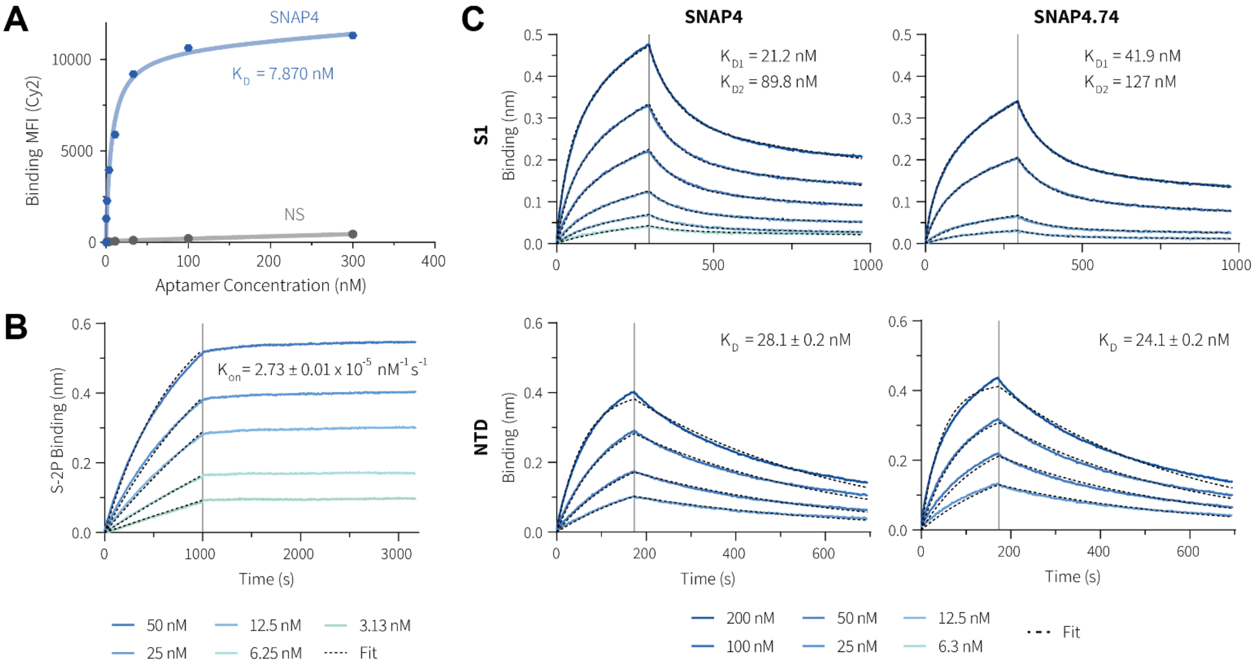

Figure 2.2. A) Cy5-labeled SNAP4 at various concentrations was incubated with HEK293_S-2P cells to generate a binding curve. The graph shows the total (blue) and non-specific (gray) binding of aptamer based on a one-site binding model (dashed lines). K_D was determined by non-linear regression (1 biological replicate.) B-C) Biotinylated aptamer was loaded on SA biosensors and associated with protein. The gray lines indicate the switch from analyte association to dissociation. K_{on} values (mean±s.d., n= 4-6) were determined from a global fit (dark gray line) of the kinetic data at various concentrations of proteins for the indicated binding model. B) SNAP4 aptamer binding to S-2P protein fitted to a 1:1 model for association only. C) SNAP4 aptamer (left) or SNAP4.74 aptamer (right) binding to S1 protein with 1:2 model fit (top) or NTD protein with 1:1 model fit (bottom).

SNAP4 aptamer truncations

Truncations have been shown to improve binding affinity and decrease synthesis costs[12,17]. We designed two truncations of SNAP4 aptamer (88nt original length): SNAP4.74 (74nt in length) and SNAP4.40 (40nt in length) (Table S2.2). We predicted the secondary structure of SNAP4, SNAP4.74, and SNAP4.40 through the computational tool NUPACK[36] and observed similar core structures in the 52-nt random region (Fig. S2.4A). We observed that SNAP4.74 binds similar targets and with similar affinity as SNAP4. SNAP4.74 bound S-2P and S1 in ELISA (Fig. S2.4B), and bound S1 and NTD with kinetic constants in the same range as those of SNAP4 (Fig. 2.2C, right half). We did not observe binding of SNAP4.40 aptamer to S-2P and S1 protein by ELISA and BLI (Fig. 2.S4B). Overall, the high affinity of SNAP4 and SNAP4.74 aptamer for S-2P-expressing cells as well as S-2P protein shows that the cell and protein SELEX strategy enriched for a robust, target-binding aptamer.

SNAP1 and SNAP4 competition study

To determine whether SNAP1 and SNAP4 compete for the same binding site and can be used together in detection assays, and we incubated various ratios of unlabeled aptamer to fluorescently-labeled Cy5-SNAP1 and measured binding of Cy5-SNAP1 to immobilized S1 protein by flow cytometry. As expected, unlabeled SNAP1 effectively reduced binding of Cy5-SNAP1 to S1 protein (Fig. S2.5). In contrast, there was no significant difference in Cy5-SNAP1 binding to S1 protein in the presence of either unlabeled scrSNAP1, an aptamer that does not bind S protein, and unlabeled SNAP4.74 at ratios of 10:1 and 20:1. These data support that SNAP1 and SNAP4.74 have minimal competition and are suitable to use together.

Aptamer sandwich LFA (AptaFlow)

To apply SNAP4 to SARS-CoV-2 testing, we developed an antibody-free aptamer-based lateral flow assay (AptaFlow) (Fig. 2.3A). We use biotinylated aptamer for analyte capture onto streptavidin-coated test band, and aptamer-conjugated gold nanoparticles for detection. First, all components, including analyte, biotinylated aptamer, and aptamer-conjugated gold nanoparticles, are incubated together. A lateral flow strip is dipped sequentially into the sample, wash buffer, and signal enhancing buffer. In total, the assay takes under 1 hour to complete. First, we tested whether AptaFlow could detect S-2P protein. We found that AptaFlow that used SNAP4.74-gold nanoparticles and SNAP4.74-biotin were highly sensitive, detecting as low as 100 pM S-2P protein (Fig. S2.6). We were able to detect as low as 500 pM S-2P protein spiked in healthy human volunteer nasal swab samples using AptaFlow with SNAP1-gold nanoparticles and SNAP4.74-biotin (Fig. S2.7), indicating that our system can detect S protein in clinically-relevant samples.

We validated that both SNAP1[16] and SNAP4 can detect UV-inactivated SARS-CoV-2 in aptamer-antibody sandwich ELISAs. Therefore, we hypothesized that SNAP1 and SNAP4.74 can be used in AptaFlow to detect UV-inactivated virus. First, we compared how well SNAP4.74- and SNAP1-conjugated gold nanoparticles can detect UV-inactivated SARS-CoV-2 virus. We found that AptaFlow using SNAP4.74-conjugated gold nanoparticles and SNAP4.74-biotin did not detect virus at 1 x 10^7 copies/mL. However, AptaFlow using SNAP1-conjugated gold nanoparticles and SNAP4.74-biotin gave an 8.7-fold higher signal for 1 x 10^7 copies/mL UV-inactivated virus than the equivalent concentration of our negative control, heat-inactivated virus. We previously showed that heat-inactivated virus, which contained denatured S protein, is not recognized by

SNAP1[16]. AptaFlow using SNAP1-conjugated gold nanoparticles and SNAP4.74-biotin can detect UV-inactivated virus at concentrations as low as 10^6 copies/mL (Fig. 2.3B).

In this application, AptaFlow required two different aptamer sequences with different epitopes to detect low concentrations of virus despite the trimeric nature of S protein and its multivalent display on SARS-CoV-2. It is possible that when the analyte is very limited, the sterically-unhindered biotinylated aptamer binds to the majority of potential sites on one analyte molecule, preventing the gold nanoparticle-conjugated aptamer from binding. Using minimally-competing aptamers such as SNAP1 and SNAP4.74 could avoid this limitation.

AptaFlow detected 100 pM S protein, which is equivalent to approximately 6×10^9 S protein in sample, but AptaFlow also detected 10^6 copies/mL virus, which is approximately 2×10^6 S protein in a sample (assuming ~20 S protein per virus[37]). The higher sensitivity with virus samples may be due to only needing one or few capture aptamers to anchor the virus particle onto the test band, allowing the majority of the other binding sites to be occupied by the detection aptamer.

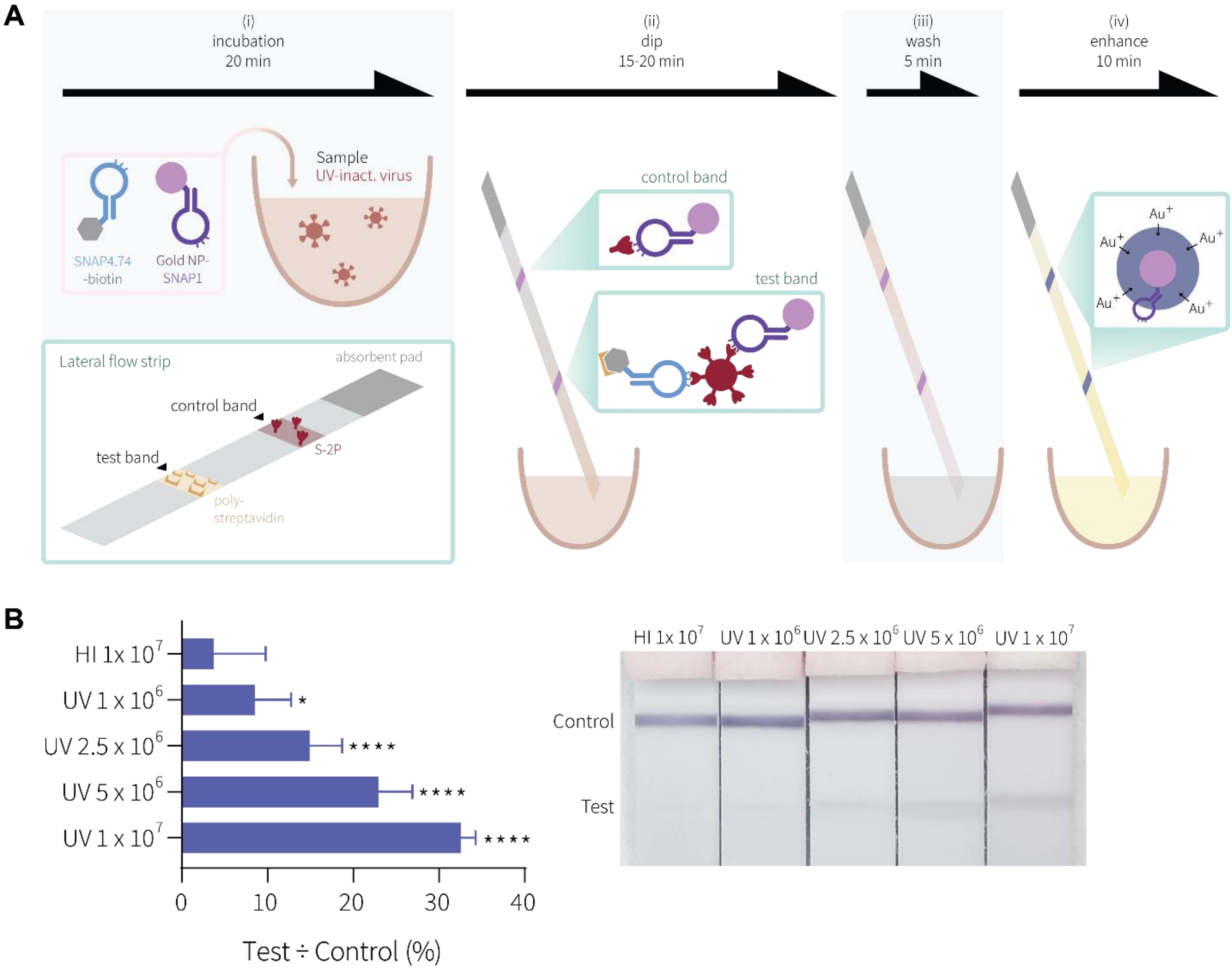

Figure 2.3. A) Step-by-step process for AptaFlow. (i) incubating reagents with SARS-CoV-2 sample. (ii) dipping of the test strip into the sample. (iii) washing to reduce non-specific signals. (iv) enhancing signal to increase sensitivity. B) Limit of detection of LFA system with UV-inactivated virus (UV) at various concentrations (copies/mL) and heat-inactivated (HI) virus (negative control). Bars indicate mean. Brackets indicate 95% CI. Statistical significance was determined by one-way ANOVA with Dunnett correction. * indicates $p < 0.05$ and **** indicates $p < 0.0001$ when compared to HI 1 x 107 copies/mL; n = 3-4 per experimental group. A representative image is shown.

Conclusion

In this article, we discovered and characterized SNAP4, a DNA aptamer that binds the SARS-CoV-2 S protein at the NTD. Using SNAP4 and SNAP1, we developed an aptamer sandwich LFA (AptaFlow) with a LOD for UV-inactivated virus of 10^6 copies/mL, which is the minimal LOD set by the WHO[38]. Compared to other antigen tests, AptaFlow theoretically outperforms five out of 18 commercially-available tests[38]. Recent findings suggest that individuals with low viral loads of $<10^6$ copies/mL are unlikely to transmit the disease[31–33, 39], suggesting that antigen tests like AptaFlow can be used to detect infectious cases. Additionally, AptaFlow provides results in under 1 hour and costs under $1 per test to manufacture in our hands. AptaFlow can be further improved by: (1) integrating gold nanoparticles and biotinylated aptamer onto sample pad of lateral flow strip to eliminate one step and save 20min; (2) using complementary DNA in the control band instead of S-2P protein to reduce costs and improve scalability; and (3) utilize multiple capture aptamers that bind to different mutation epitopes, which may allow detection of different variants. Although SARS-CoV-2 rapidly mutates and AptaFlow best detects the wild-type virus, SNAP1 and SNAP4 are modular and can be substituted with new aptamer sequences that detect other variants. By enabling more frequent at-home testing, more accessible diagnostic tools like AptaFlow may reduce the burden of the COVID-19 pandemic on healthcare systems.

Acknowledgements

We thank NIH RADx-Radical Data Coordination Center (DCC) at University of California San Diego (funded under NIH grant # 1U24LM013755-01) for the SARS-Related Coronavirus 2, Isolate USA-WA1/2020, NR-52281 deposited by the Centers for Disease Control and Prevention and obtained through BEI Resources, NIAID. We thank Lexi Walls and Dr. David Veesler for providing the SARS-CoV-2-FL_pseudo_2P_pcDNA3.1 plasmid, Lauren Carter from the Institute of Protein Design (IPD) who kindly produced S-2P protein through support from the Bill and Melinda Gates Foundation, Kelsi Penewit for NGS assistance, and Daniel Leon for lateral flow strip manufacturing assistance.

References

(1) Wouters, O. J.; Shadlen, K. C.; Salcher-Konrad, M.; Pollard, A. J.; Larson, H. J.; Teerawattananon, Y.; Jit, M. Challenges in Ensuring Global Access to COVID-19 Vaccines: Production, Affordability, Allocation, and Deployment. *The Lancet* **2021**, *397* (10278), 1023–1034. https://doi.org/10.1016/S0140-6736(21)00306-8.

(2) Peeling, R. W.; Olliaro, P. L.; Boeras, D. I.; Fongwen, N. Scaling up COVID-19 Rapid Antigen Tests: Promises and Challenges. *Lancet Infect. Dis.* **2021**, *21* (9), e290–e295. https://doi.org/10.1016/S1473-3099(21)00048-7.

(3) Larremore, D. B.; Wilder, B.; Lester, E.; Shehata, S.; Burke, J. M.; Hay, J. A.; Milind, T.; Mina, M. J.; Parker, R. Test Sensitivity Is Secondary to Frequency and Turnaround Time for COVID-19 Surveillance. *medRxiv* **2020**, 2020.06.22.20136309. https://doi.org/10.1101/2020.06.22.20136309.

(4) Mina, M. J.; Parker, R.; Larremore, D. B. Rethinking Covid-19 Test Sensitivity — A Strategy for Containment. *N. Engl. J. Med.* **2020**, *383* (22), e120. https://doi.org/10.1056/NEJMp2025631.

(5) Nimjee, S. M.; Rusconi, C. P.; Sullenger, B. A. Aptamers: An Emerging Class of Therapeutics. *Annu. Rev. Med.* **2005**, *56* (1), 555–583. https://doi.org/10.1146/annurev.med.56.062904.144915.

(6) Bunka, D. H. J.; Stockley, P. G. Aptamers Come of Age - At Last. *Nat. Rev. Microbiol.* **2006**, *4* (8), 588–596. https://doi.org/10.1038/nrmicro1458.

(7) Keefe, A. D.; Pai, S.; Ellington, A. Aptamers as Therapeutics. *Nat. Rev. Drug Discov.* **2010**, *9* (7), 537–550. https://doi.org/10.1038/nrd3141.

(8) Kumar Kulabhusan, P.; Hussain, B.; Yüce, M. Current Perspectives on Aptamers as Diagnostic Tools and Therapeutic Agents. *Pharmaceutics* **2020**, *12* (7), 646. https://doi.org/10.3390/pharmaceutics12070646.

(9) Tuerk, C.; Gold, L. Systematic Evolution of Ligands by Exponential Enrichment: RNA Ligands to Bacteriophage T4 DNA Polymerase. *Science* **1990**, *249* (4968), 505–510. https://doi.org/10.1126/science.2200121.

(10) Ellington, A. D.; Szostak, J. W. In Vitro Selection of RNA Molecules That Bind Specific Ligands. *Nature* **1990**, *346* (6287), 818–822. https://doi.org/10.1038/346818a0.

(11) Robertson, D. L.; Joyce, G. F. Selection in Vitro of an RNA Enzyme That Specifically Cleaves Single-Stranded DNA. *Lett. Nat.* **1990**, *344* (March), 467–468.

(12) Kacherovsky, N.; Cardle, I. I.; Cheng, E. L.; Yu, J. L.; Baldwin, M. L.; Salipante, S. J.; Jensen, M. C.; Pun, S. H. Traceless Aptamer-Mediated Isolation of CD8+ T Cells for Chimeric Antigen Receptor T-Cell Therapy. *Nat. Biomed. Eng.* **2019**, *3* (10), 783–795. https://doi.org/10.1038/s41551-019-0411-6.

(13) Gotrik, M. R.; Feagin, T. A.; Csordas, A. T.; Nakamoto, M. A.; Soh, H. T. Advancements in Aptamer Discovery Technologies. *Acc. Chem. Res.* **2016**, *49* (9), 1903–1910. https://doi.org/10.1021/acs.accounts.6b00283.

(14) Li, F. Structure, Function, and Evolution of Coronavirus Spike Proteins. *Annu. Rev. Virol.* **2016**, *3*, 237–261. https://doi.org/10.1146/annurev-virology-110615-042301.

(15) McCallum, M.; Walls, A. C.; Bowen, J. E.; Corti, D.; Veesler, D. Structure-Guided Covalent Stabilization of Coronavirus Spike Glycoprotein Trimers in the Closed Conformation. *Nat. Struct. Mol. Biol.* **2020**. https://doi.org/10.1038/s41594-020-0483-8.

(16) Kacherovsky, N.; Yang, L. F.; Dang, H. V.; Cheng, E. L.; Cardle, I. I.; Walls, A. C.; McCallum, M.; Sellers, D. L.; DiMaio, F.; Salipante, S. J.; Corti, D.; Veesler, D.; Pun, S. Discovery and Characterization of Spike N-terminal Domain-binding Aptamers for Rapid SARS-CoV-2 Detection. *Angew. Chem. Int. Ed.* **2021**, anie.202107730. https://doi.org/10.1002/anie.202107730.

(17) Schmitz, A.; Weber, A.; Bayin, M.; Breuers, S.; Fieberg, V.; Famulok, M.; Mayer, G. A SARS-CoV-2 Spike Binding DNA Aptamer That Inhibits Pseudovirus Infection by an RBD-Independent Mechanism. *Angew. Chem. - Int. Ed.* **2021**, 2–9. https://doi.org/10.1002/anie.202100316.

(18) Song, Y.; Song, J.; Wei, X.; Huang, M.; Sun, M.; Zhu, L.; Lin, B.; Shen, H.; Zhu, Z.; Yang, C. Discovery of Aptamers Targeting the Receptor-Binding Domain of the SARS-

CoV-2 Spike Glycoprotein. *Anal. Chem.* **2020**, *92* (14), 9895–9900. https://doi.org/10.1021/acs.analchem.0c01394.

(19) Posthuma-Trumpie, G. A.; Korf, J.; van Amerongen, A. Lateral Flow (Immuno)Assay: Its Strengths, Weaknesses, Opportunities and Threats. A Literature Survey. *Anal. Bioanal. Chem.* **2009**, *393* (2), 569–582. https://doi.org/10.1007/s00216-008-2287-2.

(20) Panpradist, N.; Beck, I. A.; Chung, M. H.; Kiarie, J. N.; Frenkel, L. M.; Lutz, B. R. Simplified Paper Format for Detecting HIV Drug Resistance in Clinical Specimens by Oligonucleotide Ligation. *PLOS ONE* **2016**, *11* (1), e0145962. https://doi.org/10.1371/journal.pone.0145962.

(21) Panpradist, N.; Beck, I. A.; Vrana, J.; Higa, N.; McIntyre, D.; Ruth, P. S.; So, I.; Kline, E. C.; Kanthula, R.; Wong-On-Wing, A.; Lim, J.; Ko, D.; Milne, R.; Rossouw, T.; Feucht, U. D.; Chung, M.; Jourdain, G.; Ngo-Giang-Huong, N.; Laomanit, L.; Soria, J.; Lai, J.; Klavins, E. D.; Frenkel, L. M.; Lutz, B. R. OLA-Simple: A Software-Guided HIV-1 Drug Resistance Test for Low-Resource Laboratories. *EBioMedicine* **2019**, *50*, 34–44. https://doi.org/10.1016/j.ebiom.2019.11.002.

(22) Panpradist, N.; Beck, I. A.; Ruth, P. S.; Ávila-Ríos, S.; García-Morales, C.; Soto-Nava, M.; Tapia-Trejo, D.; Matías-Florentino, M.; Paz-Juarez, H. E.; Del Arenal-Sanchez, S.; Reyes-Terán, G.; Lutz, B. R.; Frenkel, L. M. Near Point-of-Care, Point-Mutation Test to Detect Drug Resistance in HIV-1: A Validation Study in a Mexican Cohort. *AIDS Lond. Engl.* **2020**, *34* (9), 1331–1338. https://doi.org/10.1097/QAD.0000000000002524.

(23) Mahmoudi, T.; de la Guardia, M.; Baradaran, B. Lateral Flow Assays towards Point-of-Care Cancer Detection: A Review of Current Progress and Future Trends. *TrAC Trends Anal. Chem.* **2020**, *125*, 115842. https://doi.org/10.1016/j.trac.2020.115842.

(24) Grant, B. D.; Anderson, C. E.; Williford, J. R.; Alonzo, L. F.; Glukhova, V. A.; Boyle, D. S.; Weigl, B. H.; Nichols, K. P. SARS-CoV-2 Coronavirus Nucleocapsid Antigen-Detecting Half-Strip Lateral Flow Assay Toward the Development of Point of Care Tests Using Commercially Available Reagents. *Anal. Chem.* **2020**, *92* (16), 11305–11309. https://doi.org/10.1021/acs.analchem.0c01975.

(25) Panpradist, N.; Kline, E. C.; Atkinson, R. G.; Roller, M.; Wang, Q.; Hull, I. T.; Kotnik, J. H.; Oreskovic, A. K.; Bennett, C.; Leon, D.; Lyon, V.; Gilligan-Steinberg, S. D.; Han, P. D.; Drain, P. K.; Starita, L. M.; Thompson, M. J.; Lutz, B. R. Harmony COVID-19: A Ready-to-Use Kit, Low-Cost Detector, and Smartphone App for Point-of-Care SARS-CoV-2 RNA Detection. *Sci. Adv.* **2021**. https://doi.org/10.1126/sciadv.abj1281.

(26) Oliveira, S. C.; de Magalhães, M. T. Q.; Homan, E. J. Immunoinformatic Analysis of SARS-CoV-2 Nucleocapsid Protein and Identification of COVID-19 Vaccine Targets. *Front. Immunol.* **2020**, *11*.

(27) Lakhin, A. V.; Tarantul, V. Z.; Gening, L. V. Aptamers: Problems, Solutions and Prospects. *Acta Naturae* **2013**, *5* (4), 34–43.

(28) Baker, B. R.; Lai, R. Y.; Wood, M. S.; Doctor, E. H.; Heeger, A. J.; Plaxco, K. W. An Electronic, Aptamer-Based Small-Molecule Sensor for the Rapid, Label-Free Detection of Cocaine in Adulterated Samples and Biological Fluids. *J. Am. Chem. Soc.* **2006**, *128* (10), 3138–3139. https://doi.org/10.1021/ja056957p.

(29) Wrapp, D.; Wang, N.; Corbett, K. S.; Goldsmith, J. A.; Hsieh, C. L.; Abiona, O.; Graham, B. S.; McLellan, J. S. Cryo-EM Structure of the 2019-NCoV Spike in the Prefusion Conformation. *Science* **2020**, *367* (6483), 1260–1263. https://doi.org/10.1126/science.aax0902.

(30) Hsieh, C.; Goldsmith, J. A.; Schaub, J. M.; Divenere, A. M.; Kuo, H.; Javanmardi, K.; Le, K. C.; Wrapp, D.; Lee, A. G.; Liu, Y.; Chou, C.; Byrne, P. O.; Hjorth, C. K.; Johnson, N. V.; Ludes-meyers, J.; Nguyen, A. W.; Park, J.; Wang, N.; Amengor, D.; Lavinder, J. J.; Ippolito, G. C.; Maynard, J. A.; Finkelstein, I. J.; Mclellan, J. S. Structure-Based Design of Prefusion-Stabilized SARS-CoV-2 Spikes. **2020**, *1505* (September), 1501–1505.

(31) COVID-19 Target product profiles for priority diagnostics to support response to the COVID-19 pandemic v.1.0 **2020** https://www.who.int/publications/m/item/covid-19-target-product-profiles-for-priority-diagnostics-to-support-response-to-the-covid-19-pandemic-v.0.1 (accessed 2022 -03 -28).

(32) Cubas-Atienzar, A. I.; Kontogianni, K.; Edwards, T.; Wooding, D.; Buist, K.; Thompson, C. R.; Williams, C. T.; Patterson, E. I.; Hughes, G. L.; Baldwin, L.; Escadafal, C.; Sacks, J. A.; Adams, E. R. Limit of Detection in Different Matrices of 19 Commercially Available Rapid Antigen Tests for the Detection of SARS-CoV-2. *Sci Rep* **2021**, 11 (1), 18313. https://doi.org/10.1038/s41598-021-97489-9.

(33) Wölfel, R.; Corman, V. M.; Guggemos, W.; Seilmaier, M.; Zange, S.; Müller, M. A.; Niemeyer, D.; Jones, T. C.; Vollmar, P.; Rothe, C.; Hoelscher, M.; Bleicker, T.; Brünink, S.; Schneider, J.; Ehmann, R.; Zwirglmaier, K.; Drosten, C.; Wendtner, C. Virological Assessment of Hospitalized Patients with COVID-2019. *Nature* **2020**, *581* (7809), 465–469. https://doi.org/10.1038/s41586-020-2196-x.

(34) Wang, T.; Yin, W.; AlShamaileh, H.; Zhang, Y.; Tran, P. H.-L.; Nguyen, T. N.-G.; Li, Y.; Chen, K.; Sun, M.; Hou, Y.; Zhang, W.; Zhao, Q.; Chen, C.; Zhang, P.-Z.; Duan, W. A Detailed Protein-SELEX Protocol Allowing Visual Assessments of Individual Steps for a High Success Rate. *Hum. Gene Ther. Methods* **2019**, *30* (1), 1–16. https://doi.org/10.1089/hgtb.2018.237.

(35) Zadeh, J. N.; Steenberg, C. D.; Bois, J. S.; Wolfe, B. R.; Pierce, M. B.; Khan, A. R.; Dirks, R. M.; Pierce, N. A. NUPACK: Analysis and Design of Nucleic Acid Systems. *J. Comput. Chem.* **2011**, *32* (1), 170–173. https://doi.org/10.1002/jcc.21596.

(36) Liu, J.; Lu, Y. Preparation of Aptamer-Linked Gold Nanoparticle Purple Aggregates for Colorimetric Sensing of Analytes. *Nat. Protoc.* **2006**, *1* (1), 246–252. https://doi.org/10.1038/nprot.2006.38.

(37) Ke, Z.; Oton, J.; Qu, K.; Cortese, M.; Zila, V.; McKeane, L.; Nakane, T.; Zivanov, J.; Neufeldt, C. J.; Cerikan, B.; Lu, J. M.; Peukes, J.; Xiong, X.; Kräusslich, H.-G.; Scheres, S. H. W.; Bartenschlager, R.; Briggs, J. A. G. Structures and Distributions of SARS-CoV-2 Spike Proteins on Intact Virions. *Nature* **2020**, *588* (7838), 498–502. https://doi.org/10.1038/s41586-020-2665-2.

(38) Alemany, A.; Baró, B.; Ouchi, D.; Rodó, P.; Ubals, M.; Corbacho-Monné, M.; Vergara-Alert, J.; Rodon, J.; Segalés, J.; Esteban, C.; Fernández, G.; Ruiz, L.; Bassat, Q.; Clotet, B.; Ara, J.; Vall-Mayans, M.; G-Beiras, C.; Blanco, I.; Mitjà, O. Analytical and

Clinical Performance of the Panbio COVID-19 Antigen-Detecting Rapid Diagnostic Test. *J. Infect.* **2021**, *82* (5), 186–230. https://doi.org/10.1016/j.jinf.2020.12.033.

(39) Singanayagam, A.; Patel, M.; Charlett, A.; Bernal, J. L.; Saliba, V.; Ellis, J.; Ladhani, S.; Zambon, M.; Gopal, R. Duration of Infectiousness and Correlation with RT-PCR Cycle Threshold Values in Cases of COVID-19, England, January to May 2020. *Eurosurveillance* **2020**, *25* (32), 2001483. https://doi.org/10.2807/1560-7917.ES.2020.25.32.2001483.

Supplementary Information

Supplementary Tables

Table S2.1. SELEX conditions. T indicates 0.1 mg/mL yeast tRNA; S indicates 0.1 mg/mL salmon sperm DNA; M indicates million cells; HTID indicates His-Tag Isolation Dynabeads™.

Round	**Aptamer pool (nM)**	**Binding conditions**	**Negative Selection**	**Time (min)**	**Positive Selection**	**Time (min)**
1	14,000	0.25% BSA, T		-	10M HEK293_S-2P	60
2	500	0.5% BSA, T	10M HEK293	60	5M HEK293_S-2P	60
3	500	0.75% BSA, T, S	10M HEK293	60	2.5M HEK293_S-2P	30
4	250	0.75% BSA, T, S	10M HEK293 x2	30 x2	2M HEK293_S-2P	30
5	250	1.5% BSA, T, S	10M HEK293	60	1M HEK293_S-2P	30
6	100	2% BSA, T, S	10M HEK293 x2	30 x2	1M HEK293_S-2P	30
7	250	2% BSA, T, S	100 µL HTID	30	20 nM S-2P + 10 µL HTID	30
8	100	2% BSA, T, S	100 µL HTID	30	20 nM S-2P + 10 µL HTID	20
9	100	3% BSA, T, S	100 µL HTID	30	10 nM S-2P + 10 µL HTID	20
10	100	4% BSA, T, S	100 µL HTID	30	5 nM S-2P + 10 µL HTID	20

Table S2.2. Aptamer sequences. See methods for list of modifications. A1 through A4: random region underlined.

Name	**Sequence**
A1	5'-ATCCAGAGTGACGCAGCATGCACGCAGTTCTGTTGTTTTGATCATGGTACTCTGCTCTGGTTGTTTATCGTGGACACGGTGGCTTAGT-3'
A2	5'-ATCCAGAGTGACGCAGCATGGCATTGGGAGGTAGGTGGTGCATTCACTCTTCAAGATGTGGTCGTTTCATTGGACACGGTGGCTTAGT-3'
A3	5'-ATCCAGAGTGACGCAGCACGAGTATGCATCGTCATCGAGTTCAGTGGGTTCTGCTAACGCTCTTTATACATGGACACGGTGGCTTAGT-3'
A4, SNAP4	5'-ATCCAGAGTGACGCAGCAAGGGTATTGGCAGTGGTAGGTACTGCGTGCGTTGTGGTTCTAGCATGTTTAATGGACACGGTGGCTTAGT-3'
SNAP4.74	5'-CCGTGACGCAGCAAGGGTATTGGCAGTGGTAGGTACTGCGTGCGTTGTGGTTCTAGCATGTTTAATGGACACGG-3'
SNAP4.40	5'-GCGCAGCAAGGGTATTGGCAGTGGTAGGTACTGCGTGCGC-3'
NB	5'-CACAGTGACGCAGCAACAGAGGTGTAGAAGTACACGTGAACAAGCTTG-3'
scrSNAP1	5’-TCGCTCTTTCCGCTTCTTCGCGGGATCGCGTGGCCTATCGACCAAGCGCATCTATCTTCGAATCCGCGTAAGTCCGTGTGTGCGAA-3’
SNAP1	5'-TCGCTCTTTCCGCTTCTTCGCGGTCATTGTGCATCCTGACTGACCCTAAGGTGCGAACATCGCCCGCGTAAGTCCGTGTGTGCGAA-3'
SP6.51	5'-GATATCAACCCATGGTAGGTATTGCTTGGTAGGGATAGTGGGCTTGATGTT-3'

Supplementary Figures

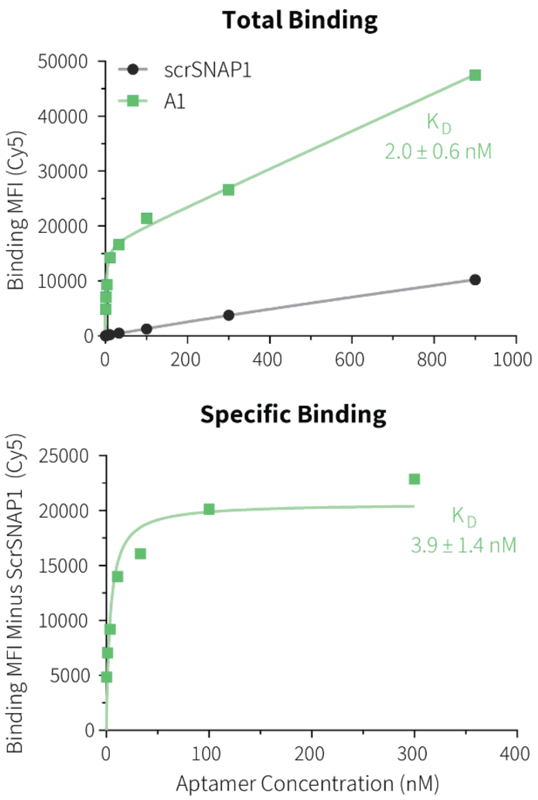

Figure S2.1. A1 binds HEK293_S-2P cells. Cy5-labeled A1 at various concentrations was incubated with S-2P-overexpressing HEK293 cells to generate a binding curve. The graph shows the total (green) and non-specific (gray) binding of A1 based on a one-site binding model (n=1). K_D was determined by non-linear regression.

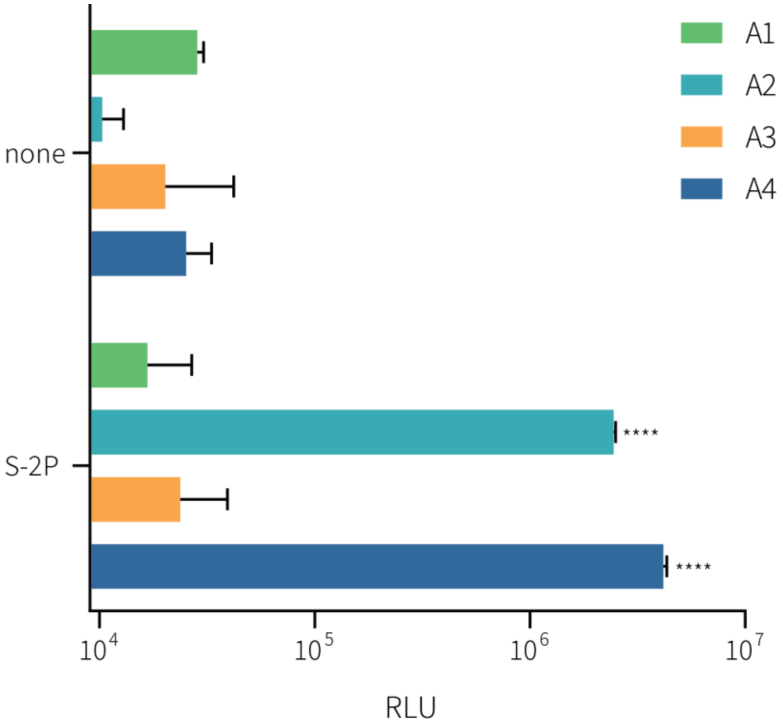

Figure S2.2. Screening of candidate aptamers by aptamer-antibody sandwich ELISA. ELISA assay using biotinylated aptamers (A1 through A4) as capture agents to detect 2.5 nM S-2P recombinant protein using anti-S HRP antibody. Data represent the mean of three replicates. Brackets represent S.D. **** denotes $p < 0.0001$ comparing S-2P to none, determined by 2-way ANOVA with Fisher's LSD test.

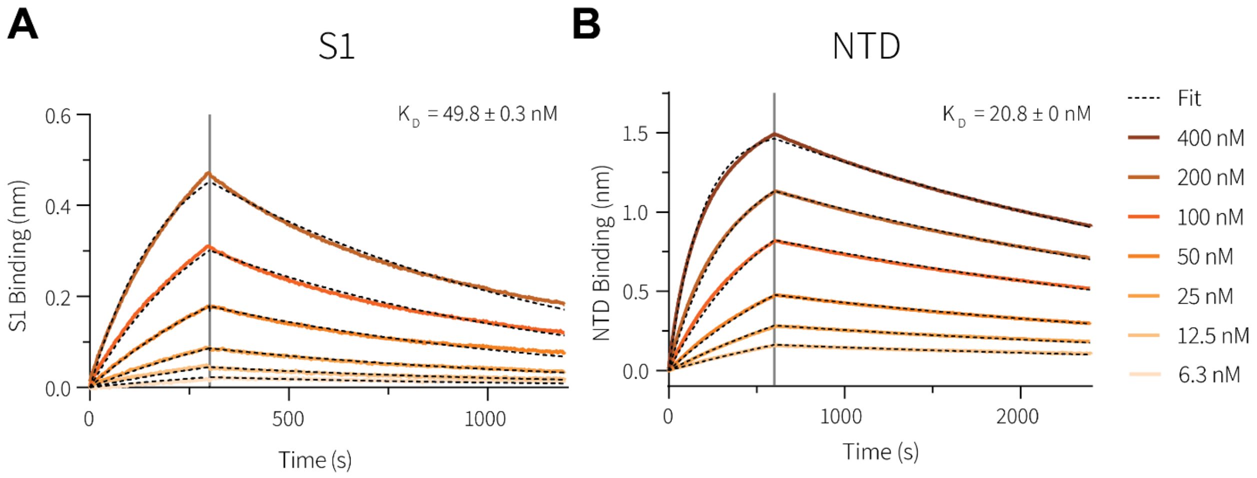

Figure S2.3. Aptamer SP6.51 binds S1 and NTD protein. A-B) Biotinylated aptamer was loaded on SA biosensors and associated with protein. The gray line indicates the switch from analyte association to dissociation. K_D values (mean ± S.D., n= 4-6) were determined from a global fit (dark gray line) of the kinetic data at various concentrations of proteins for the indicated binding model. A) SP6.51 aptamer binding to S1 protein fitted to a 1:1 model. B) SP6.51 aptamer binding to NTD protein fitted to a 1:1 model.

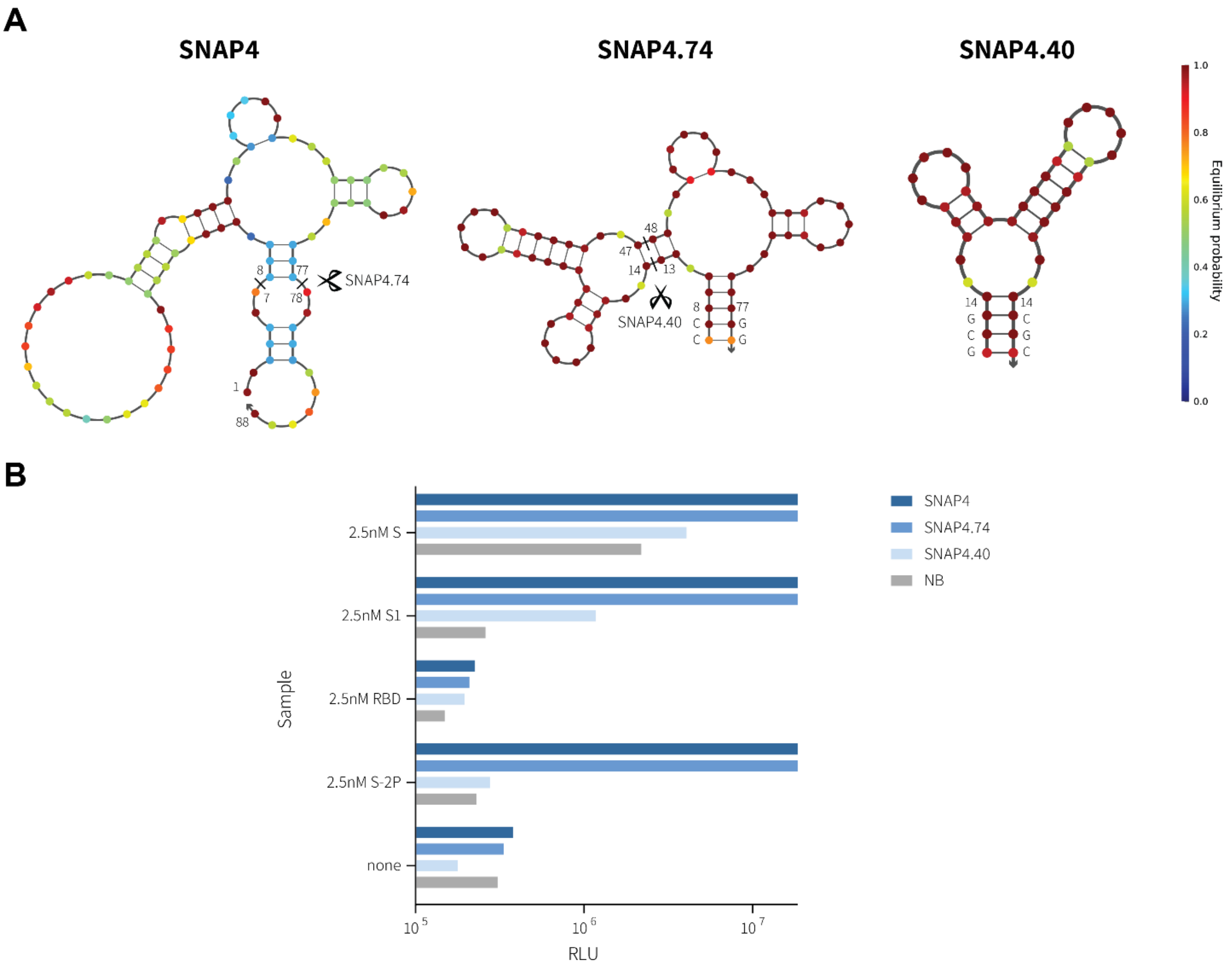

Figure S2.4. SNAP4 aptamer truncations. A) Secondary structure was predicted using NUPACK (http://www.nupack.org/) with the following conditions: 4ºC, 137 mM Na^{+}, 5.5 mM Mg^{++}. Arrows represent the 3' end of the aptamer. Nucleotides are color-coded by their equilibrium probability (see legend on right). B) ELISA assay using biotinylated aptamers as capture agents to detect various concentrations of SARS-CoV-2 using anti-S HRP antibody. NB is a non-binding aptamer. Data show one replicate.

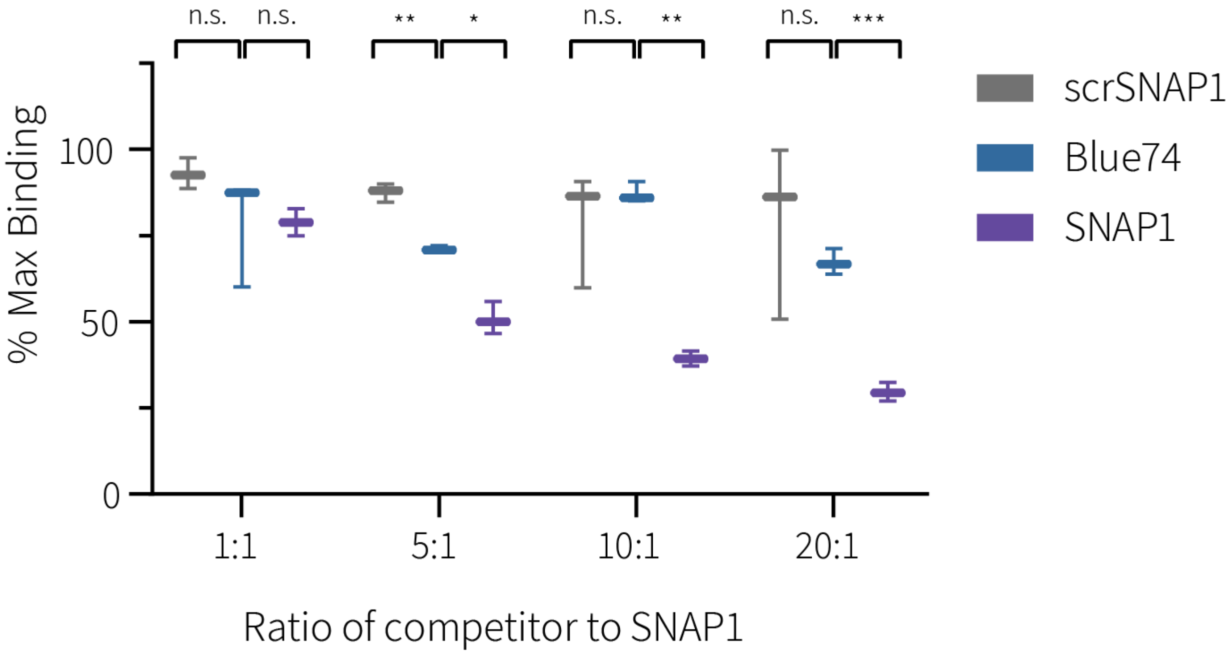

Figure S2.5. Competition binding to S1 protein between SNAP4.74 to SNAP1. Protein G magnetic spheres immobilized with Fc-tagged SARS-CoV-2 S1 protein were incubated with 30 nM Cy5-labeled SNAP1 in the presence of increasing concentrations of unlabeled scrSNAP1 (gray), SNAP4.74 (blue), or SNAP1 (purple). The fluorescence of spheres was measured by flow cytometry. Data shows three biological replicates. Bars represent range. Lines represent median. Boxes represent interquartile range. * denotes $p < 0.05$, ** $p < 0.01$, *** $p < 0.001$ as determined by 2-way ANOVA with Tukey's multiple comparison test.

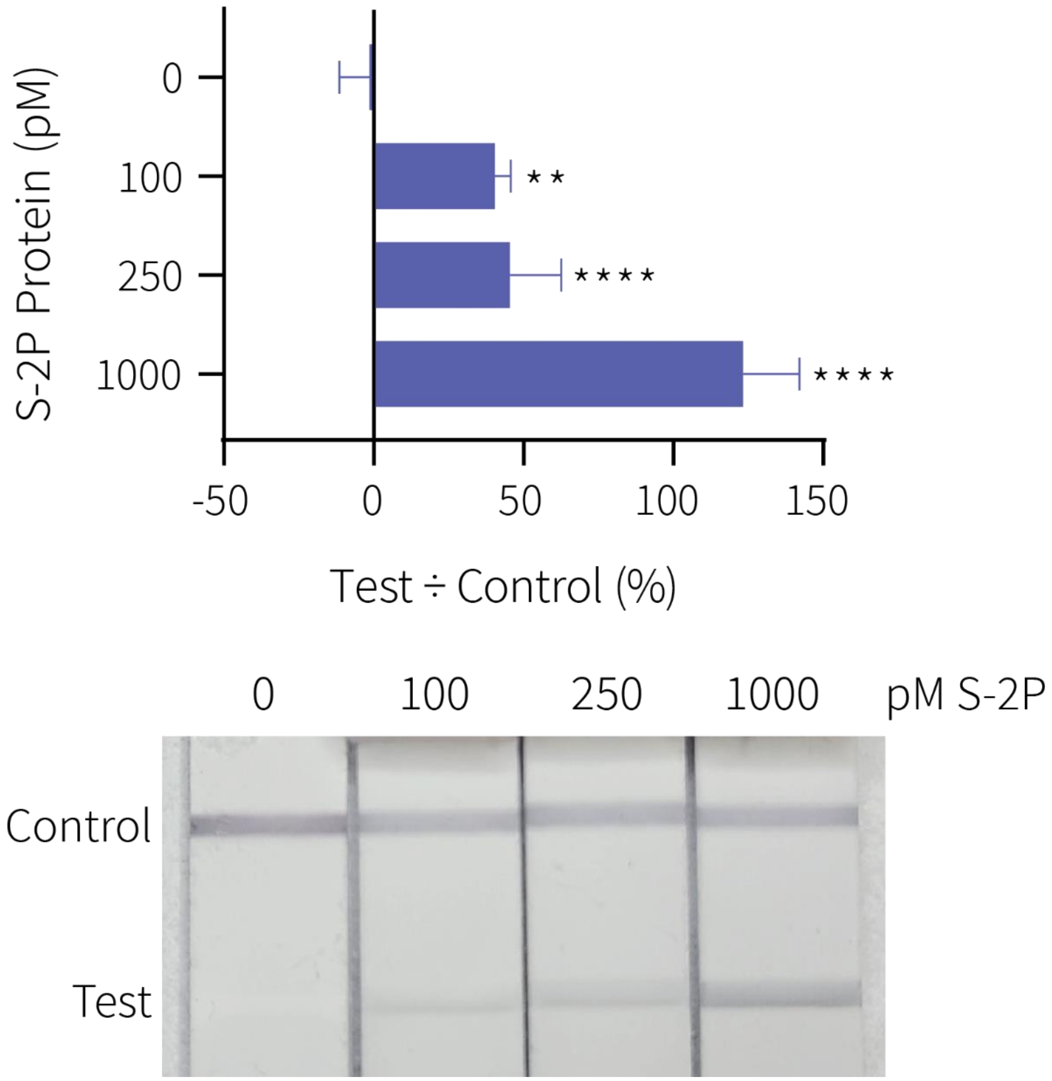

Figure S2.6. Detection of S-2P protein by aptamer-based LFA. Detection of S-2P protein at various concentrations including zero (negative control). Bars indicate mean. Brackets indicate 95% CI. Statistical significance determined by one-way ANOVA with Dunnett correction; * indicates $p < 0.05$, ** indicates $p < 0.01$, and **** indicates $p < 0.0001$ when compared to 0 pM S-2P; n = 3-4 per experimental group. A epresentative image is shown.

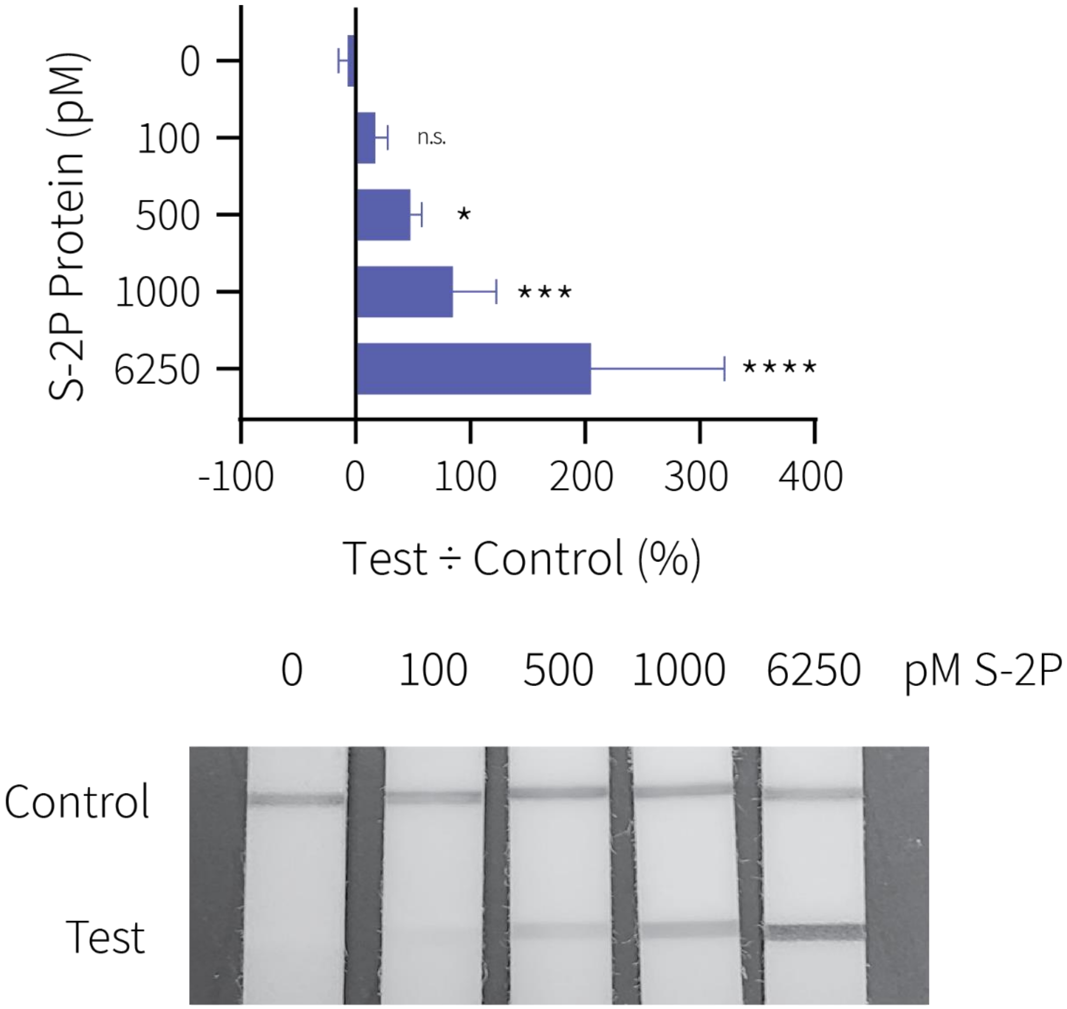

Figure S2.7. Detection of S-2P protein spiked in nasal swab samples by aptamer-based LFA. Detection of S-2P protein spiked into healthy human nasal swab at various concentrations including zero (negative control). Bars indicate mean. Brackets indicate 95% CI. Statistical significance determined by one-way ANOVA with Dunnett correction; * indicates $p < 0.05$, *** indicates $p < 0.001$, and **** indicates $p < 0.0001$ when compared to 0 pM S-2P; n = 3 per experimental group. A representative image is shown.

Chapter 3

SCORe: SARS-CoV-2 Omicron variant RBD-binding DNA ap-tamer for multiplexed rapid detection and pseudovirus neutral-ization

Adapted from publication in Analytical Chemistry

Lucy F. Yang, Nataly Kacherovsky, Joey Liang, Stephen J. Salipante, Suzie H. Pun

Abstract

During the COVID-19 (coronavirus disease 2019) pandemic, several SARS-CoV-2 variants of concern emerged, including the Omicron variant, which has enhanced infectivity and immune invasion. Many antibodies and aptamers that bind the spike (S) of previous strains of SARS-CoV-2 either do not bind or bind with low affinity to Omicron S. In this study, we report a high affinity SARS-CoV-2 Omicron RBD-binding aptamer (SCORe) that binds Omicron BA.1 and BA.2 RBD with nanomolar KD1. We employ aptamers SCORe.50 and SNAP4.74 in a multiplexed lateral flow assay (LFA) to distinguish between Omicron and wild-type S at concentrations as low as 100 pM. Finally, we show that SCORe.50 and its dimerized form SCOReD can neutralize Omicron S-pseudotyped virus infection of ACE2-overexpressing cells by >70%. SCORe there-fore has potential applications in COVID-19 rapid diagnostics as well as in viral neutralization.

Introduction

First identified to infect humans in 1967, the coronavirus subfamily has low pathogenic strains, such as HCoV-OC43, and severe disease-causing strains, such as SARS-CoV and SARS-CoV-2.[1] The evolution rate of coronavirus is impacted by its large RNA-based genome, a low fidelity of viral polymerase, and recombination with other coronavirus variants within the host.[1] SARS-CoV-2, the pathogen responsible for the on-going COVID-19 pandemic, has already evolved since its initial characterization in 2019. The World Health Organization has five SARS-CoV-2 variants as “variants of concern” (VOC) due to their increased global health significance: Alpha (B.1.1.7), Beta (B.1.351), Gamma (P.1), Delta (B.1.617.2) and Omicron (B.1.1529 AKA BA.1, BA.2) strains.[2] First detected in November 2021, Omicron variant SARS-CoV-2 has both improved immune evasion and more efficient spread compared to the ancestral virus.[3, 4] Plasma from both convalescent and vaccinated individuals have less neutralizing activity against Omicron pseudovirus versus earlier strains. In addition, the Omicron strain binds with 2.4-fold higher affinity to the angiotensin converting enzyme-2 (ACE2) receptor compared with wild-type Wuhan-Hu-1 virus.[3]

The SARS-CoV-2 enveloped virus has a lipid shell containing spike protein (S protein or S), a trimeric glycosylated protein that mediates virus binding to angiotensin converting enzyme 2 (ACE2) on host cells. Each S monomer is comprised of the exposed subunit 1 (S1) connected to the membrane-anchored subunit 2 (S2) by a furin cleavage sequence.[5] S1 contains both the critical receptor-binding domain (RBD) that contacts the ACE2 receptor through the receptor-binding motif (RBM, residues 438-506) as well as the amino-terminal domain (NTD). S1 is the primary target for anti-SARS-CoV-2 neutralizing antibodies, which have been reported to bind both the RBD and NTD domains of SARS-CoV-2 S protein.[6]

Molecular recognition agents that bind new variants are critical for rapid detection of SARS-CoV-2 in patient samples as well as in emerging technologies to sense intact virus in the environment. The two major types of molecular recognition agents are antibodies and aptamers, which are nucleic acid sequences that fold into secondary structures. Aptamers have target binding affinities on par with antibodies while offering several advantages such as small size and extended shelf life.[7] As chemically synthesized agents, aptamers are also produced more affordably and reproducibly than antibodies,[8] and are therefore well-suited for rapid viral detection assays. Numerous platforms for aptamer-based SARS-CoV-2 detection have been reported, including electrochemical sensors[9, 10], ion transport-sensing nanopores[11], metal nanostructure-based optical sensing[12], and lateral flow assays (LFAs), which provide rapid, point-of-care results from patient samples[13, 14].

DNA aptamers against SARS-CoV-2 S protein have been identified using a library selection process called systematic evolution of ligands by exponential enrichment (SELEX).[15] Most of the currently-reported aptamers were selected against wild-type or Alpha variant S protein.[13, 16, 17, 18, 19] To our knowledge, only the Li group has reported a DNA aptamer that binds to BA.1 S protein[20] that doesn't also bind non-specifically to His-tag-containing proteins (Fig. S3.1A).[18] We tested S-binding aptamers (SP6.51,[18] SNAP1,[13] SNAP4.74,[14] CoV2-4C[19], CoV2-6C3[21]), including two reported by our group, but none of these aptamers show specific binding to BA.1 NTD or S1 protein (Fig. S3.1) in our testing conditions.[13, 14, 18] While the CoV2-4C[19] and CoV2-6C3[21] aptamers showed binding to BA.1 NTD, S1 and RBD proteins, they also showed binding to a control, His-tagged protein (Fig. S3.1A).

In this work, we report a SARS-CoV-2 Omicron variant RBD-binding aptamer (SCORe) identified in protein SELEX using BA.1 S1 protein. Biolayer interferometry (BLI) measurements reveal that SCORe and its truncation SCORe.50 bind BA.1 RBD with a K_{D1} of 1.73 nM and 2.80 nM, respectively, and that SCORe.50 binds BA.2 RBD with 2.86 nM affinity. We demonstrate a proof-of-concept rapid lateral flow assay (LFA) that uses SCORe.50 and SNAP4.74 to differentiate between BA.1 and wild-type SARS-CoV-2 S protein. Lastly, we show that monomeric SCORe.50 as well as SCORe.50 dimers (SCOReD) can reduce BA.1 S pseudotyped virus infection of ACE2-expressing human cells by over 70%.

Experimental Section

Oligonucleotides

All oligonucleotides were synthesized by Integrated DNA Technologies. The ssDNA library used in the protein SELEX process was 5'-TCGCTCTTTC CGCTTCTTCGCGG-N40-CCGCGTAAGTCCGTGTGTGCGAA-3'. The forward primer for amplification was 5'-FAM-TCGCTCTTTCCGCTTCTTCG-3', and the reverse primer for amplification was 5'-Biotin-TTCGCACACACGGACTTACG-3'. Oligonucleotide sequences are listed in Table S2. Modifications to oligonucleotides included: FITC (5'-FITC – sequence – 3'), biotin (5'- biotin – iSp18 spacer – sequence – 3'), and Cy5 (5' – Cy5 – sequence – 3'). All aptamer pools and aptamers were annealed before use by diluting to 1 - 10 µM in SELEX wash buffer (SELEX WB), heating at 95°C for 5 min, and snap-cooling on ice for 5 min. Dimers (ex. SCOReD) were annealed by combining T linker aptamer (ex. SCORe.50-30T) and A linker aptamer (ex. SCORe.50-30A) sequences at 25 µM in SELEX WB, heating at 95°C for 5 min, and snap-cooling on ice for 5 min.

Buffers

SELEX wash buffer (SELEX WB) was prepared as previously described.[13] Binding buffer contained 0.1 mg/mL yeast tRNA (Invitrogen) (tRNA), 0.1 mg/mL salmon sperm DNA (Invitrogen) (SS DNA), and 2% MACS BSA solution (Miltenyi Biotec).

Recombinant proteins

BA.1 SARS-CoV-2 S protein S1 domain (ACROBiosystems S1N-C52Ha), BA.1 SARS-CoV-2 S protein trimer (ACROBiosystems SPN-C52Hz), BA.1 SARS-CoV-2 S protein NTD (ACROBiosystems SPD-C522df), BA.1 SARS-CoV-2 S protein RBD (ACROBiosystems SPD-C522e), BA.2 SARS-CoV-2 S protein RBD (ACROBiosystems SPD-C522g), SARS-CoV S1 protein (ACROBiosystems S1N-S52H5), human Axl (tyrosine-protein kinase receptor UFO) (ACROBiosystems AXL-H5226), and recombinant human CD8A protein (Sino Biological 10980-H08H) were purchased in lyophilized form. All proteins contained His-tag. Omicron variant (BA.1) S1, S trimer, NTD, and RBD contained the following mutations: A67V, HV69-70del, T95I, G142D, VYY143-145del, N211del, L212I, ins214EPE, G339D, S371L, S373P, S375F, K417N, N440K, G446S, S477N, T478K, E484A, Q493R, G496S, Q498R, N501Y, Y505H, T547K, D614G, H655Y, N679K, P681H, N764K, D796Y, N856K, Q954H, N969K, L981F. BA.2 RBD contained the following mutations: G339D, S371F, S373P, S375F, T376A, D405N, R408S, K417N, N440K, S477N, T478K, E484A, Q493R, Q498R, N501Y, Y505H. Anti-SARS-CoV-2 Spike RBD antibody, chimeric mAb, Human IgG1 (ACROBiosystems S1N-M130) and anti-SARS-CoV-2 Spike RBD broadly neutralizing antibody, Human IgG1

(ACROBiosystems SPD-M265) were purchased in lyophilized form. All proteins were reconstituted, aliquoted, and stored according to manufacturer's recommendations. SARS-CoV-2 wild-type S protein trimer was kindly provided by the Institute of Protein Design (IPD) at the University of Washington.

Viruses

Inactivated (UV or heat-inactivated) SARS-CoV-2 (wild-type, Alpha, Beta, Delta, BA.1) and HCoV-OC43 virus samples at known concentrations were kindly provided by the NIH RADx-Radical Data Coordination Center (DCC) at the University of California San Diego and BEI Resources.

Protein-SELEX

The protocol was based on the guidelines outlined by Wang et al.[22] and is outlined in Fig. 3.1. Experimental conditions for 7 rounds of SELEX are summarized in Table S1. Aptamers were partitioned by Dynabeads His-tag isolation & Pulldown (Novex by Life Technologies) on a rack magnet. Aptamers were amplified with Phusion® High-Fidelity DNA Polymerase (NEB). Annealing, strand separation, and composition of buffers were described previously[2].

Next-generation sequencing (NGS) and data analysis

The DNA pools from SELEX rounds were PCR amplified with barcoded primers described in Table S3 using the MiSeq Reagent Kit v2 (300-cycles) (Illumina) and MiSeq System (Illumina) per manufacturer's protocol. Sequence reads were analyzed as previously described.[13] NUPACK was used to predict secondary structure of candidate aptamers.[23]

Biolayer interferometry (BLI)

Studies were performed with an Octet Red96 machine (Sartorius) at 25^{o}C and 1,000 rpm sample agitation. Pre-soaked Ni-NTA (NTA) sensors were rinsed in 1% BSA, 0.1 mg/mL tRNA, 0.1 mg/mL SS DNA, 0.01% Tween-20 SELEX WB ("diluent") for 100s. For experiments containing nasal swab in buffer, nasal swab samples were collected as previously described and spiked into diluent.[14] Next, tips were loaded with 50 nM His-tagged protein until signal reached a 3.5 nm signal threshold. Subsequently, tips were cross-linked in 0.1 M EDC 0.025 M NHS in H_2O for 60 s, quenched in 1 M ethanolamine PBS (pH 8.5) for 60 s, and rinsed in diluent for 100 s. Then biosensors were baselined in diluent for another 100 s. After association with protein of interest diluted to the desired concentration, sensor tips were returned to the baseline diluent well for dissociation. Data were analyzed with Octet Data Analysis 9.0 (Sartorius). Kinetic values were determined from a global fit of several curves generated from serial dilutions of the protein with a 1:2 binding model (heterogenous ligand). The K_{D1} describes the rate of the initial binding and the K_{D2} describes the rate of a second binding event after the initial binding.

Aptamer round pool binding assay

The protocol was conducted using an ELISA-like plate binding assay as previously described.[13] In brief, 96 well plates were coated overnight with protein of interest. After washing and blocking wells with 5% BSA, 0.1 mg/mL tRNA, 0.1 mg/mL SS DNA and 0.01% Tween-20 SELEX WB, fluorescein-labeled aptamer pools were incubated in the wells (30 min, RT) before staining with HRP anti-fluorescein antibody for detection with TMB substrate. Aptamer binding was quantified by UV absorbance with measurements at 450 nm.

Protein binding plate assay

Nunc MaxiSorp™ flat-bottom 96-well plates (Thermo Fisher Scientific) were coated with 50 nM protein (except Omicron S trimer at 25 nM) at 4ºC overnight. Then wells were washed four times with wash buffer (0.5% BSA, 0.01% Tween-20 SELEX WB.) Next, wells were incubated with blocking buffer (5% BSA, 0.1 mg/mL tRNA, 0.1 mg/mL SS DNA, 0.01% Tween-20 SELEX WB) for 1.5 hr at room temperature. After blocking buffer removal via flick and tap, 100 nM biotin-labeled aptamer pools or control biotin-labeled aptamer in binding buffer were incubated for 30 min at room temperature. Then the plate was washed four times with wash buffer and stained with Pierce™ High Sensitivity streptavidin HRP (1:16,000 1 mg/mL, Thermo Scientific 21130) for 1 h at room temperature. Lastly, the plate was washed four times with wash buffer. Pierce™ TMB substrate kit (Thermo Scientific 1854050) was mixed at 1:1 according to manufacturer's protocol, then added to wells and incubated at room temperature until desired blue color was developed (5-30 min.) 2M sulfuric acid was added to each well to terminate the HRP reaction. The absorbance of the solution (yellow) was measured using the Infinite 200 PRO plate reader (Tecan) at 450 nm with 550 nm as reference. The absorbance values of the groups were deducted from wells without aptamer and plotted.

Gold nanoparticle synthesis

Gold nanoparticles were prepared by the citrate synthesis method that involves sodium citrate reduction of tetrachloroauric acid as previously described.[14]

Gold nanoparticle and antibody conjugation

Antibody-conjugate gold nanoparticles were prepared by adapting a protocol from Wang et al.[24] Anti-RBD chimeric mAb human IgG1 antibody (ACROBiosystems S1N-M130) was activated with 10-fold excess Traut's reagent in 2mM EDTA PBS (pH 8.0) for 1 hr, then desalted by Zeba™ Spin Desalting Columns, 7K MWCO (Thermo Scientific).[24] 10 μg/mL of activated antibody was added to 1 mL gold nanoparticles, and incubated for 5 min before addition of 150 μM thiol-PEG12-acid (Broadpharm BP-21916). After 2 hr incubation, 0.25% BSA was added to the solution and further incubated for 5 min before use.

LFA dipstick manufacturing

The protocol was conducted as previously described,[14] with adjustments to the striped test lines: Test line 1: 2 mg/mL polystreptavidin R (pSA) (Eagle Biosciences, # 10 120 030) in DPBS. Test line 2: 0.5 mg/mL anti-FITC antibody (BioLegend, #408302). Control line: 0.5 mg/mL anti-human IgG antibody (BioLegend #410701).

Multiplex LFA

Binding buffer (1% BSA, 0.1 mg/mL tRNA, 0.1 mg/mL SS DNA, 0.01% Tween-20), 25 nM biotinylated aptamer, 25 nM FITC-labeled aptamer, and 50 μL antibody-functionalized gold nanoparticles were prepared, then analyte was added to a total volume of 100 μL. The solution was incubated at RT for 20 min with rocking. Then, a lateral flow device was dipped into the solution for 15-20 min (entire volume absorbed). Lastly, the lateral flow devices are dipped in 25 µL SELEX WB for 5 min (partial volume absorbed. For each strip, the average pixel values in the control band, test bands, and background (blank area between bands) were calculated. The band values were background-subtracted, then the percent maximum signal across all strips for the same band was calculated. The LOD was determined from the lowest concentration of sample that was significantly higher than the negative control.

Cell culture

The HEK293 ACE2 cell line stably expressing ACE2, generously provided by Dr. Jesse Bloom (Fred Hutchinson Cancer Research Center), was cultured in DMEM (Gibco) 10% FBS at 5% CO_2 37^{o}C.[25]

HEK293 ACE2 competition

25 nM of His-tagged Omicron (BA.1) S trimer was incubated with 250 nM or 2.5 µM of SCOReD, 250 nM or 2.5 µM of SNAP1D, or 500 nM or 5 µM of SCORe.50 in binding buffer for 20 min at RT, then added to 200,000 HEK293T ACE2 cells for 20 min on ice. Cells were stained with anti-His-tag antibody-FITC (Invitrogen MA1-81891) and fluorescence read by flow cytometer (Attune NxT, Invitrogen). The median mean fluorescence intensity (MFI) of experiment groups were background subtracted from that of untreated cells. The percent inhibition was calculated by subtracting experiment value from S only average value and dividing by S only average value.

Virus neutralization studies

10,000 HEK293 ACE2 cells were plated in a 96-well plate and cultured to 75% confluence. Aptamers were annealed at 25 μM in DMEM 3 mM $MgCl_2$. 12.5 μL (1:500 dilution in DMEM 3mM $MgCl_2$ 2% FBS) of Omicron variant (BA.1) SARS-CoV-2 S protein pseudotyped virus (ACROBiosystems PSSO-HLGB003) and indicated concentrations of aptamer or neutralizing antibody (ACROBiosystems SPD-M265) were incubated together in DMEM 3 mM $MgCl_2$ for 1 hr at RT. Incubation media was removed and virus added for 2 hr at 37^{o}C. Next, media was replaced with fresh complete media, and cells were incubated for 48 hr. Cells were rinsed with 200 μL 1X PBS, then 40 μL Reporter Lysis Buffer (Promega) was added. Plate was frozen then thawed before 20 μL cell lysate was mixed with 100 μL Luciferase Assay Reagent. Light was measured using the Infinite 200 PRO plate reader (Tecan) at 1000 nm integration time. The relative light units (RLUs) of experiment groups were background subtracted from that of untreated cells. The percent infectivity was calculated by normalizing to virus-only treatment group values.

Results & Discussion

Aptamer selection

We designed a protein SELEX strategy to identify aptamers that bind to BA.1 S protein RBD. Our previous attempts using the RBD domain alone for SELEX were not successful, so we used SARS-CoV-2 BA.1 S1 protein for positive selection and SARS-CoV-2 BA.1 NTD for negative selection in later rounds. We conducted seven rounds of SELEX with increasing stringency, accomplished by increasing the amount of competitors (BSA, tRNA, SS DNA) and decreasing the amount concentration of aptamer pool and positive selection target Omicron (BA.1) S1 protein (Fig. 3.1). For the last three rounds, we evaluated binding of the fluorescein-labeled aptamer libraries from each selection round and observed binding to BA.1 S1 protein, but not to NTD or Axl (tyrosine-protein kinase receptor UFO) (negative control protein), starting in round 5 (R5) and increasing significantly in round 7 (R7) (Fig. S3.2). We analyzed libraries from rounds 3 through 7 by next generation sequencing (NGS) and identified four aptamers (named A1 to A4) of interest. A1 and A2 first appeared as early as round 3, while A3 appeared in round 4 and A4 in round 5. Between round 5 and 6, all motifs sharply increased in prevalence (Fig. S3.3). We tested A1, A2, A3, and A4 and observed that A3 bound BA.1 S1 but not BA.1 NTD (Fig. S3.1). Aptamers A1, A2 and A4 did not bind either protein and therefore were not further characterized.

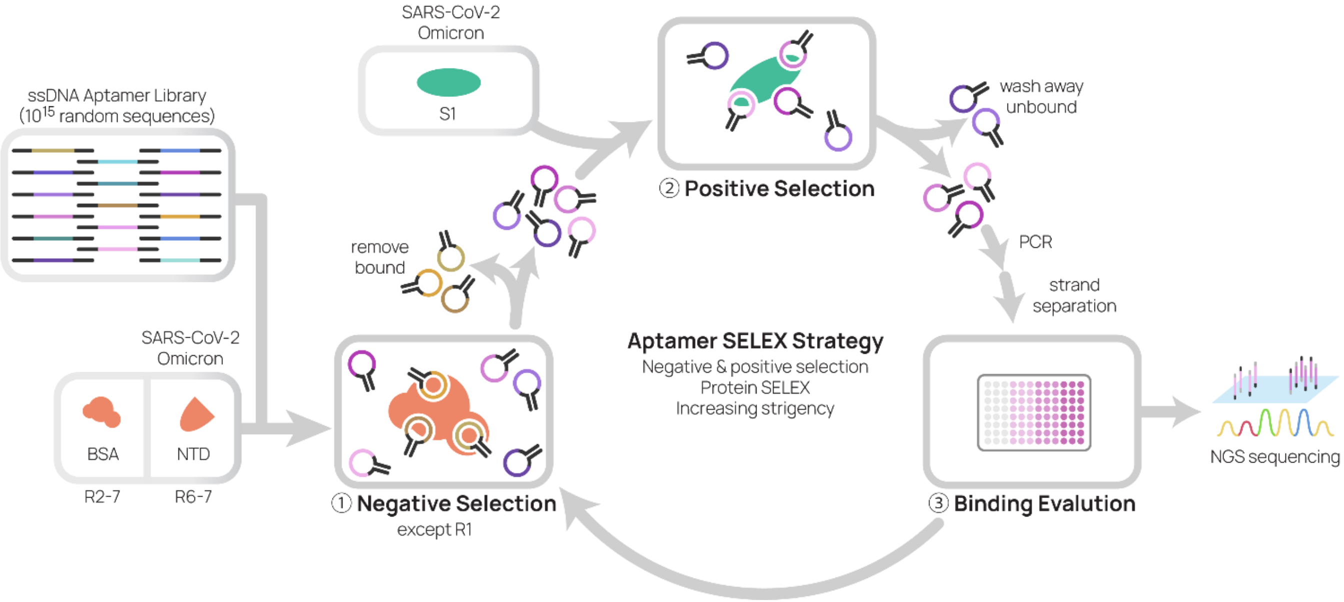

Figure 3.1. Schematic of SELEX process. A single-stranded DNA (ssDNA) aptamer library is subjected to SARS-CoV-2 Omicron (BA.1) S1 protein for seven rounds of positive selection with increasing stringency, and SARS-CoV-2 Omicron (BA.1) NTD negative selection in round 6 and 7 only. Binding of aptamer round pool is evaluated by protein binding assay, and aptamer round pools with positive binding are sequenced and analyzed.

Characterization of SCORe (A3)

To determine the binding location of A3 on S1 protein, we evaluated A3 (Fig. 3.2A) binding to Omicron S protein, S1, RBD and NTD via an ELISA-like plate binding assay, and found that A3 bound BA.1 RBD, BA.2 RBD, BA.1 S1, and BA.1 S protein (Fig. 2B) but not BA.1 NTD. Given the binding location, we renamed A3 to **S**ARS-**C**oV-2 **O**micron **R**BD-binding Aptam**e**r (SCORe). The selection of an RBD-binding aptamer demonstrates that our SELEX strategy using negative selection against NTD was effective.

We compared the sequence of SCORe to other aptamers reported to bind SARS-CoV-2 S protein at the RBD (CoV2-RBD-1C, CoV2-RBD-4C, CoV2-6C3, nCoV-S1-Apt1, MSA5, and MSA52-T5)[17, 19, 20] and found no similarity between SCORe and the other sequences when compared with local alignment (Fig. S3.4).[26]

We next truncated the aptamer sequence to reduce synthesis cost and potentially improve binding affinity.[9] The NUPACK secondary structure prediction of SCORe shows a stem formed by the constant sequences used for PCR amplification. We removed this stem in a 50-nt truncation called SCORe.50 (Fig. 3.2A).

We used biolayer interferometry (BLI) to measure the binding affinity of SCORe and SCORe.50 for immobilized BA.1 RBD, revealing a K_{D1} of 1.73 nM and 2.80 nM, respectively (Fig. 3.2C). In addition, we show that SCORe.50 binds BA.2 RBD with a K_{D1} of 2.86 nM. We did not observe binding of RBD to biotinylated SCORe, SCORe.50, or SCORe.50-30T (SCORe.50 with a 30-nt thymidine linker) bound to streptavidin sensor surfaces. We hypothesize that immobilization of the 5’ end of the aptamer may prevent conformational mobility required for binding. Lastly, we showed that SCORe and

SCORe.50 bound to UV-inactivated BA.1 virus with 18.8-fold and 11.2-fold higher signal, respectively, than heat-inactivated BA.1 virus (Fig. 3.2D).

We also evaluated aptamer binding to spike proteins of other variants of SARS-CoV-2 and other coronaviruses. We observed binding of SCORe and SCORe.50 to wild-type RBD and wild-type S protein in plate binding assay (Fig. S5A) but not by BLI (Fig. S3.5B). We observed binding of SCORe and SCORe.50 to Delta variant S1 protein, but not SARS-CoV S1 protein by plate binding assay (Fig S3.5C). We also observed binding of both SCORe and SCORe.50 to UV-inactivated SARS-CoV-2 virus of different variants, including Omicron (BA.1), Delta, and wild-type (Fig. 3.2D). SCORe and SCORe.50 did not bind as highly to heat-inactivated SARS-CoV-2 virus presumably due to denaturation of S protein. Based on these results, we hypothesize that while SCORe can bind to RBD of several variants, such as wild-type and Delta variant, it binds with the highest affinity to Omicron variant RBD. Due to similarity in binding patterns and affinities on the same order of magnitude (K_{D1} of 1.73 nM for SCORe and K_{D1} of 2.80 nM for SCORe.50), we used SCORe.50 in subsequent studies.

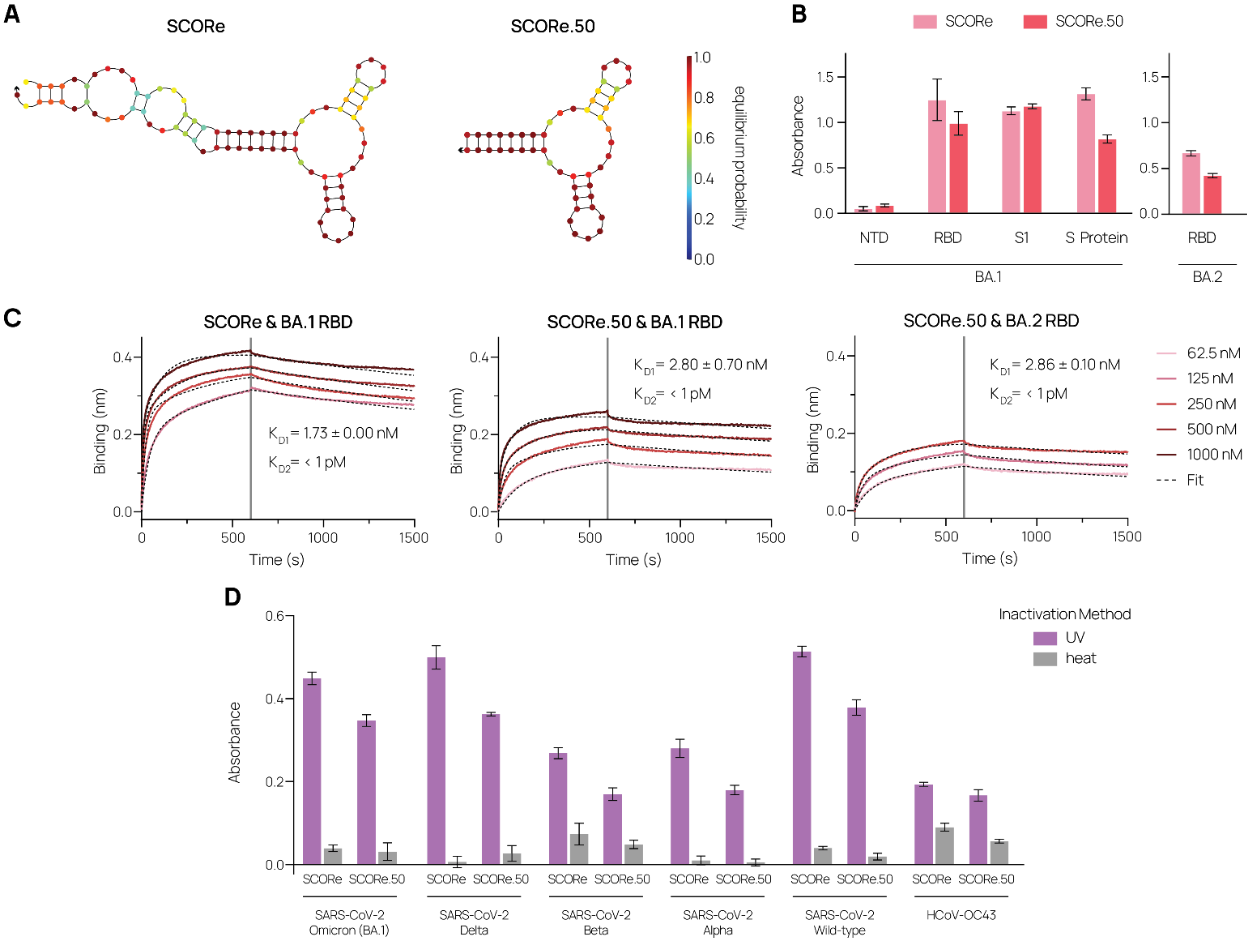

Figure 3.2. A) Secondary structure prediction with the following conditions: 22^{o}C, 137 mM Na^{+}, 5.5 mM Mg^{++}. Arrows represent the 3' end of the aptamer. B, D) Proteins (B) or inactivated virus (D) adsorbed onto surface are incubated with 100 nM biotinylated aptamer and stained with streptavidin-HRP with detection of the HRP substrate TMB by UV absorbance. Bars indicate mean, brackets indicate S.D., n = 3. C) Biolayer interferometry assessment of binding. His-tagged RBD was loaded on Ni-NTA biosensors and associated with SCORe-FITC or SCORe.50-biotin. The gray line indicates the switch from analyte association to dissociation after 600 s. K$_D$ values (mean ± S.D., n = 3-4) were determined from a global fit (dotted line) of the kinetic data at various concentrations of proteins for a 2:1 binding model.

Multiplexed LFA with SCORe.50 and SNAP4.74

We next applied SCORe.50 for multiplexed SARS-CoV-2 S protein detection in a lateral flow assay (LFA). Since SCORe.50 binds to Omicron S protein with higher affinity than wild-type S protein and our previously-reported SNAP4.74 binds to wild-type S protein,[14] but not Omicron S protein, we hypothesized that we could use the two aptamers in a rapid detection format to differentiate between Omicron and wild-type S protein. We used SNAP4.74-fluorescein for wild-type S protein capture using anti-FITC antibody and SCORe.50-biotin for Omicron (BA.1) S protein capture using streptavidin (Fig 3.3A). To test our custom LFA, we incubated S protein with a solution containing biotinylated SCORe.50, FITC-labeled SNAP4.74, and anti-RBD IgG gold nanoparticles (Ab-AuNP). We then dipped into the solution a lateral flow strip with three immobilized bands: (1) poly-streptavidin to capture SCORe.50-biotin, (2) anti-FITC antibody to capture SNAP4.74-FITC, and (3) anti-IgG antibody control to capture remaining Ab-AuNPs. Ab-AuNPs bind to captured S proteins, allowing users to read results with the naked eye (Fig. 3.3A). The lateral flow device differentiates between Omicron (BA.1) and wild-type S protein, with detection limit as low as 50 pM of Omicron (BA.1) S protein and 100 pM of wild-type S protein (Fig. 3.3B). Although SCORe.50 can bind wild-type S protein by plate binding studies, we did not observe binding of SCORe.50-biotin with 1 nM wild-type S protein in lateral flow, even in the absence of SNAP4.74-FITC. We also show that SCORe.50-biotin can bind BA.1 RBD in buffer containing nasal swab by BLI, demonstrating potential for patient nasal swab sample LFA (Fig. S3.6). Our system is a proof-of-concept for a modular aptamer-based LFA system for differentiation between SARS-CoV-2 variants or diseases with similar symptoms, such as influenza. Because disease severity differs between variants,[27] an LFA system that can distinguish between SARS-CoV-2 variants may provide information useful for patient care and disease epidemiology.

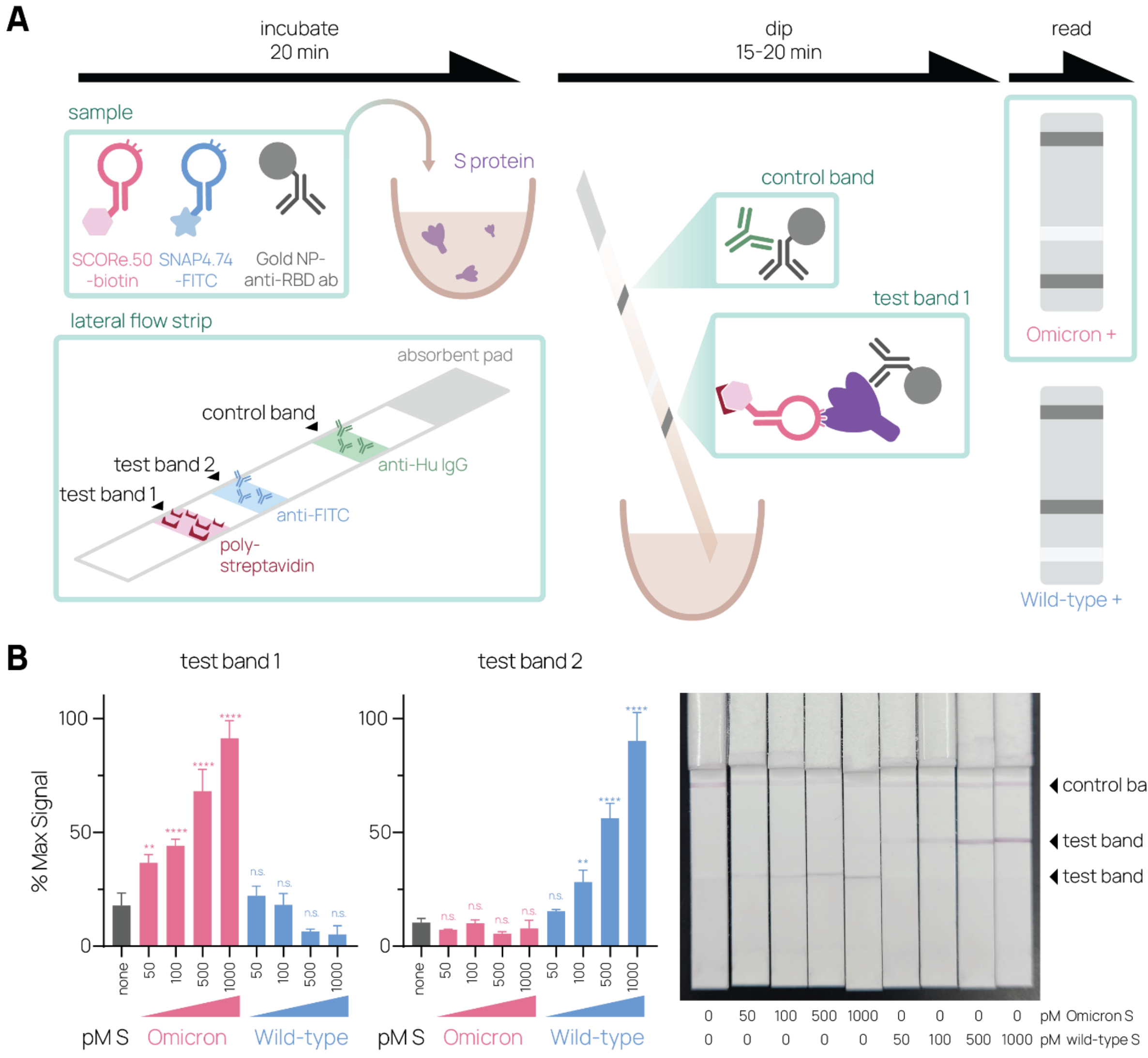

Figure 3.3. A) LFA schematic. B) Detection and differentiation between Omicron (BA.1) and wild-type SARS-CoV-2 S protein. “None” and “0 pM” indicate negative controls, which were treated identically as other samples except with no S protein added. Bars indicate mean. Brackets indicate S.D. Statistical significance determined by one-way ANOVA with Dunnett correction; ** indicates $p < 0.01$, **** indicates $p < 0.0001$ when compared to no protein; n = 3 per experimental group. Representative images are shown.

Pseudovirus neutralization by SCORe.50 and SCOReD

Multivalent aptamers have previously been shown to have tighter affinity for their target protein[10]. A trimeric RNA aptamer was shown to neutralize wild-type SARS-CoV-2 entry to cells. [28] Therefore, designed SCORe.50 dimers that connect two SCORe.50 with a 12-, 20-, or 30-nt stretch of A-T complementary binding in order to augment binding affinity for Omicron RBD (Fig. S3.7A). We first show co-staining between fluorescently-labeled SCORe.50 and BA.1 RBD binding to ACE2-overexpressing cells (Fig. S3.7B). We observe no correlation with negative control aptamer (SNAP1.50), which binds wild-type NTD. Next, we screened the three dimer types by flow cytometry for competition with BA.1 S protein to ACE2-overexpressing HEK293 cells. We found that 20 A/T and 30 A/T linker length dimers were slightly more effective in reducing binding of S protein than dimers with 12 A/T (Fig. S3.7C). We also tested binding of dimers to BA.1 RBD by BLI and observed similar binding patterns and affinities for each (Fig. S3.7D). We selected the 30 A/T linker length SCORe.50 dimer (SCOReD) to focus on in following experiments (Fig. 3.4A).

We confirmed that SCOReD binds to BA.1 RBD with a K_{D1} of 1.04 nM, similar to that of SCORe.50 (Fig. 3.4B). SCOReD inhibited BA.1 S protein from binding to ACE2-overexpressing HEK293 cells, knocking down binding by 38.0% at 10-fold molar excess of SCOReD to S and 69.0% at 100-fold molar excess of SCOReD to S (Fig. 3.4C). In comparison, monomeric SCORe.50 reduces binding by 38.5% at 200-fold molar excess (equivalent to 100-fold molar excess of SCOReD). Analogous negative control dimer with wild-type-NTD-binding SNAP1.50 (SNAP1D) shows no inhibition. Lastly, we show that

SCORe.50 and SCOReD can block Omicron (BA.1) S pseudotyped virus entry (OPV) to ACE2-overexpressing HEK293 cells (Fig. 3.4D). Cells were transduced with OPV virus carrying the luciferase reporter gene in the presence of SNAP1D (control dimer), monomeric SCORe.50-30T and SCOReD. Both SCORe.50-30T and SCOReD significantly reduced pseudovirus infection compared to control dimer. Both SCORe.50 and SCOReD significantly reduced infectivity in comparison to SNAP1D at 5 μM (Fig. 3.4D) and 10 μM (Fig. S3.8) of dimer or monomer molar equivalent. In particular, SCOReD reduced infection by 42.2±4.4% at 5 μM (Fig. 3.4D) and 71.1±9.9% at 10 μM (Fig. S3.8). To probe whether SCOReD dimer provided an advantage over SCORe.50, we compared treatment with heterodimer composed of SCORe.50 and SNAP1.50 to treatment with SNAP1D and SCOReD. There was a significant difference between SNAP1D and SCOReD, but there was no significant difference between heterodimer and SNAP1D or heterodimer and SCOReD. This indicates that dimerization may not significantly augment the neutralizing capabilities of SCORe.50 (Fig. S3.9). Treatment with 10 μM SCOReD is less effective than with 10 nM or 100 nM of neutralizing antibody, which both achieved virtually complete neutralization (Fig. S3.10).

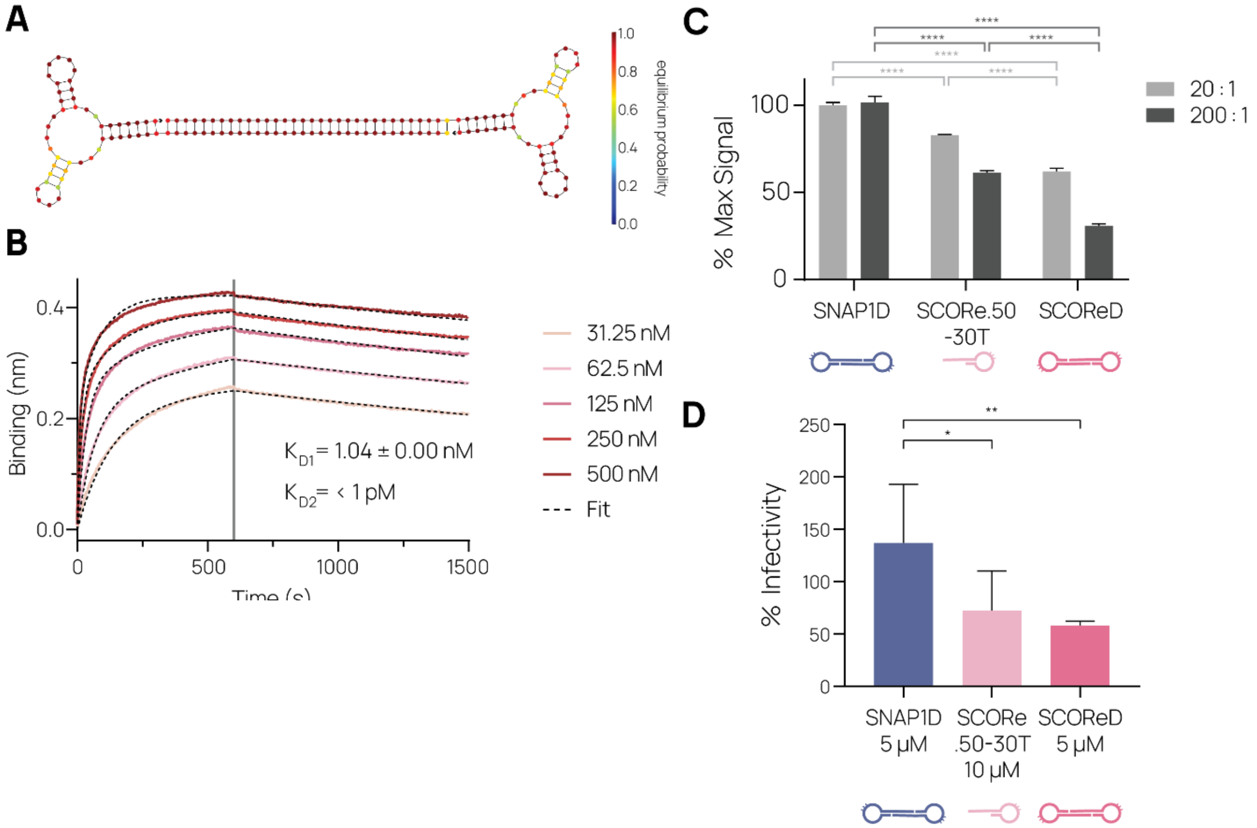

Figure 3.4. A) Secondary structure prediction as described in Fig 2. B) BLI characterization of SCOReD binding to immobilized RBD with experimental details and K_D determination as described in Figure 2. C) ACE2-overexpressing HEK293 cells were incubated with 25 nM Omicron S protein and 250 nM or 2.5 μM of indicated dimer or 500 nM or 5 μM of monomeric SCORe.50-30T. S binding was measured by flow cytometry. Ratios (20:1, 200:1) indicate molar ratio of monometic aptamer units to S protein. Three technical replicates shown. Bars represent mean, brackets represent S.D. **** denotes $p < 0.0001$ as determined by 2-way ANOVA with Tukey's multiple comparison test. D) Omicron S pseudotyped virus infection of ACE2-overexpressing HEK293 cells in the presence of various aptamer constructs. Three biological replicates performed with four technical replicates each shown. Bars represent mean, brackets represent S.D. * denotes $p < 0.05$ and ** denotes $p < 0.01$ as determined by 2-way ANOVA with Dunnett's multiple comparison test.

Conclusion

In this report, we discover and characterize SCORe, a high affinity aptamer for the Omicron BA.1 and BA.2 S protein RBD domain. We apply a SCORe truncation, SCORe.50, together with our previously reported wild-type S protein-binding aptamer, SNAP4.74, in a multiplexed lateral flow assay and demonstrate sub-nanomolar detection of and differentiation between Omicron (BA.1) and wild-type S. We demonstrated that SCORe.50 and its dimer SCOReD can compete with ACE2 for binding to Omicron (BA.1) S and inhibit pseudovirus infection. We use SCORe in rapid lateral flow assays and pseudovirus neutralization, demonstrating its versatile uses and potential for diagnostic and therapeutic applications.

Author Contributions

The manuscript was written through contributions of all authors. All authors have given approval to the final version of the manuscript. L.F.Y., N.K., and S.H.P. designed research; L.F.Y., N.K., and J.L. performed research. L.F.Y. and J.L. conducted protein plate binding studies, SELEX, and round binding studies; L.F.Y. performed NGS; L.F.Y. and S.S. analyzed NGS data; L.F.Y. generated predicted secondary structures, performed BLI studies, performed LFA studies; L.F.Y. and N.K. designed aptamer modifications; N.K. performed flow cytometry studies; N.K. And L.F.Y. conducted pseudovirus neutralization studies; L.F.Y. designed the figures; L.F.Y., N.K., J.L., and S.H.P. wrote the paper with input from all authors.

Acknowledgements

This work was supported by NIH 1U01AA029316. We thank NIH RADx-Radical Data Coordination Center (DCC) at the University of California San Diego (funded under NIH grant # 1U24LM013755-01) for the inactivated SARS-CoV-2 samples deposited by the Centers for Disease Control and Prevention and obtained through BEI Resources, NIAID. We also thank Kelsi Penewit for NGS assistance, Ruixuan Wan for gold nanoparticle synthesis assistance, Ian I. Cardle for helpful scientific discussions, Nuttada Panpradist for lateral flow assay assistance, and Dr. Jesse Bloom for kindly providing HEK293 ACE2 cells.

Abbreviations

SARS-CoV-2, severe acute respiratory syndrome coronavirus 2; S, spike protein; ACE2, Angiotensin-converting enzyme 2; RBD, receptor binding domain; NTD, N-terminal domain; LFA, lateral flow assay; SCORe, SARS-CoV-2 Omicron variant RBD-binding aptamer.

References

(1) Singh, J.; Pandit, P.; McArthur, A. G.; Banerjee, A.; Mossman, K. Evolutionary trajectory of SARS-CoV-2 and emerging variants. *Virology journal* **2021**, *18* (1), 1-21.

(2) Tao, K.; Tzou, P. L.; Nouhin, J.; Gupta, R. K.; de Oliveira, T.; Kosakovsky Pond, S. L.; Fera, D.; Shafer, R. W. The biological and clinical significance of emerging SARS-CoV-2 variants. *Nature Reviews Genetics* **2021**, *22* (12), 757-773. DOI: 10.1038/s41576-021-00408-x.

(3) Cameroni, E.; Bowen, J. E.; Rosen, L. E.; Saliba, C.; Zepeda, S. K.; Culap, K.; Pinto, D.; VanBlargan, L. A.; De Marco, A.; di Iulio, J. Broadly neutralizing antibodies overcome SARS-CoV-2 Omicron antigenic shift. *Nature* **2022**, *602* (7898), 664-670.

(4) Cele, S.; Jackson, L.; Khoury, D. S.; Khan, K.; Moyo-Gwete, T.; Tegally, H.; San, J. E.; Cromer, D.; Scheepers, C.; Amoako, D. G. Omicron extensively but incompletely escapes Pfizer BNT162b2 neutralization. *Nature* **2022**, *602* (7898), 654-656.

(5) Walls, A. C.; Park, Y.-J.; Tortorici, M. A.; Wall, A.; McGuire, A. T.; Veesler, D. Structure, function, and antigenicity of the SARS-CoV-2 spike glycoprotein. *Cell* **2020**, *181* (2), 281-292. e286.

(6) McCallum, M.; De Marco, A.; Lempp, F. A.; Tortorici, M. A.; Pinto, D.; Walls, A. C.; Beltramello, M.; Chen, A.; Liu, Z.; Zatta, F. N-terminal domain antigenic mapping reveals a site of vulnerability for SARS-CoV-2. *Cell* **2021**, *184* (9), 2332-2347. e2316. Piccoli, L.; Park, Y.-J.; Tortorici, M. A.; Czudnochowski, N.; Walls, A. C.; Beltramello, M.; Silacci-Fregni, C.; Pinto, D.; Rosen, L. E.; Bowen, J. E. Mapping neutralizing and

immunodominant sites on the SARS-CoV-2 spike receptor-binding domain by structure-guided high-resolution serology. *Cell* **2020**, *183* (4), 1024-1042. e1021. Harvey, W. T.; Carabelli, A. M.; Jackson, B.; Gupta, R. K.; Thomson, E. C.; Harrison, E. M.; Ludden, C.; Reeve, R.; Rambaut, A.; Peacock, S. J. SARS-CoV-2 variants, spike mutations and immune escape. *Nature Reviews Microbiology* **2021**, *19* (7), 409-424.

(7) Chen, A.; Yang, S. Replacing antibodies with aptamers in lateral flow immunoassay. *Biosensors and bioelectronics* **2015**, *71*, 230-242.

(8) Baker, M. Reproducibility crisis: Blame it on the antibodies. *Nature* **2015**, *521* (7552), 274-276. DOI: 10.1038/521274a.

(9) Abrego-Martinez, J. C.; Jafari, M.; Chergui, S.; Pavel, C.; Che, D.; Siaj, M. Aptamer-based electrochemical biosensor for rapid detection of SARS-CoV-2: Nanoscale electrode-aptamer-SARS-CoV-2 imaging by photo-induced force microscopy. *Biosensors and Bioelectronics* **2022**, *195*, 113595. Idili, A.; Parolo, C.; Alvarez-Diduk, R.; Merkoçi, A. Rapid and efficient detection of the SARS-CoV-2 spike protein using an electrochemical aptamer-based sensor. *ACS sensors* **2021**, *6* (8), 3093-3101. Lasserre, P.; Balansethupathy, B.; Vezza, V. J.; Butterworth, A.; Macdonald, A.; Blair, E. O.; McAteer, L.; Hannah, S.; Ward, A. C.; Hoskisson, P. A. SARS-CoV-2 Aptasensors Based on Electrochemical Impedance Spectroscopy and Low-Cost Gold Electrode Substrates. *Analytical Chemistry* **2022**.

(10) Zhang, Z.; Pandey, R.; Li, J.; Gu, J.; White, D.; Stacey, H. D.; Ang, J. C.; Steinberg, C. J.; Capretta, A.; Filipe, C. D. High-Affinity Dimeric Aptamers Enable the Rapid

Electrochemical Detection of Wild-Type and B. 1.1. 7 SARS-CoV-2 in Unprocessed Saliva. *Angewandte Chemie International Edition* **2021**, *60* (45), 24266-24274.

(11) Peinetti, A. S.; Lake, R. J.; Cong, W.; Cooper, L.; Wu, Y.; Ma, Y.; Pawel, G. T.; Toimil-Molares, M. E.; Trautmann, C.; Rong, L. Direct detection of human adenovirus or SARS-CoV-2 with ability to inform infectivity using DNA aptamer-nanopore sensors. *Science advances* **2021**, *7* (39), eabh2848.

(12) Aithal, S.; Mishriki, S.; Gupta, R.; Sahu, R. P.; Botos, G.; Tanvir, S.; Hanson, R. W.; Puri, I. K. SARS-CoV-2 detection with aptamer-functionalized gold nanoparticles. *Talanta* **2022**, *236*, 122841. Chen, H.; Park, S.-G.; Choi, N.; Kwon, H.-J.; Kang, T.; Lee, M.-K.; Choo, J. Sensitive detection of SARS-CoV-2 using a SERS-based aptasensor. *ACS sensors* **2021**, *6* (6), 2378-2385. Zavyalova, E.; Ambartsumyan, O.; Zhdanov, G.; Gribanyov, D.; Gushchin, V.; Tkachuk, A.; Rudakova, E.; Nikiforova, M.; Kuznetsova, N.; Popova, L. SERS-based aptasensor for rapid quantitative detection of SARS-CoV-2. *Nanomaterials* **2021**, *11* (6), 1394.

(13) Kacherovsky, N.; Yang, L. F.; Dang, H. V.; Cheng, E. L.; Cardle, I. I.; Walls, A. C.; McCallum, M.; Sellers, D. L.; DiMaio, F.; Salipante, S. J. Discovery and Characterization of Spike N-Terminal Domain-Binding Aptamers for Rapid SARS-CoV-2 Detection. *Angewandte Chemie* **2021**, *133* (39), 21381-21385.

(14) Yang, L. F.; Kacherovsky, N.; Panpradist, N.; Wan, R.; Liang, J.; Zhang, B.; Salipante, S. J.; Lutz, B. R.; Pun, S. H. Aptamer sandwich lateral flow assay (AptaFlow) for antibody-free SARS-CoV-2 detection. *Analytical chemistry* **2022**.

(15) Ellington, A. D.; Szostak, J. W. In vitro selection of RNA molecules that bind specific ligands. *nature* **1990**, *346* (6287), 818. Robertson, D. L.; Joyce, G. F. Selection in vitro of an RNA enzyme that specifically cleaves single-stranded DNA. *Nature* **1990**, *344* (6265), 467-468. Tuerk, C.; Gold, L. Systematic evolution of ligands by exponential enrichment: RNA ligands to bacteriophage T4 DNA polymerase. *Science* **1990**, *249* (4968), 505-510.

(16) Alves Ferreira-Bravo, I.; DeStefano, J. J. Xeno-nucleic Acid (XNA) 2’-fluoro-arabino nucleic acid (FANA) aptamers to the receptor-binding domain of SARS-CoV-2 S protein block ACE2 binding. *Viruses* **2021**, *13* (10), 1983. Gupta, A.; Anand, A.; Jain, N.; Goswami, S.; Anantharaj, A.; Patil, S.; Singh, R.; Kumar, A.; Shrivastava, T.; Bhatnagar, S. A novel G-quadruplex aptamer-based spike trimeric antigen test for the detection of SARS-CoV-2. *Molecular Therapy-Nucleic Acids* **2021**, *26*, 321-332. Liu, X.; Wang, Y. l.; Wu, J.; Qi, J.; Zeng, Z.; Wan, Q.; Chen, Z.; Manandhar, P.; Cavener, V. S.; Boyle, N. R. Neutralizing Aptamers Block S/RBD-ACE2 Interactions and Prevent Host Cell Infection. *Angewandte Chemie International Edition* **2021**, *60* (18), 10273-10278. Martínez-Roque, M. A.; Franco-Urquijo, P. A.; García-Velásquez, V. M.; Choukeife, M.; Mayer, G.; Molina-Ramírez, S. R.; Figueroa-Miranda, G.; Mayer, D.; Alvarez-Salas, L. M. DNA aptamer selection for SARS-CoV-2 spike glycoprotein detection. *Analytical biochemistry* **2022**, 114633. Shi, L.; Wang, L.; Ma, X.; Fang, X.; Xiang, L.; Yi, Y.; Li, J.; Luo, Z.; Li, G. Aptamer-Functionalized Nanochannels for One-Step Detection of SARS-CoV-2 in Samples from COVID-19 Patients. *Analytical chemistry* **2021**, *93* (49), 16646-16654. Sun, M.; Liu, S.; Wei, X.; Wan, S.; Huang, M.; Song, T.; Lu, Y.; Weng, X.; Lin, Z.; Chen, H. Aptamer

blocking strategy inhibits SARS-CoV-2 virus infection. *Angewandte Chemie* **2021**, *133* (18), 10354-10360.

(17) Li, J.; Zhang, Z.; Gu, J.; Stacey, H. D.; Ang, J. C.; Capretta, A.; Filipe, C. D.; Mossman, K. L.; Balion, C.; Salena, B. J. Diverse high-affinity DNA aptamers for wild-type and B. 1.1. 7 SARS-CoV-2 spike proteins from a pre-structured DNA library. *Nucleic Acids Research* **2021**, *49* (13), 7267-7279. Yang, G.; Li, Z.; Mohammed, I.; Zhao, L.; Wei, W.; Xiao, H.; Guo, W.; Zhao, Y.; Qu, F.; Huang, Y. Identification of SARS-CoV-2-against aptamer with high neutralization activity by blocking the RBD domain of spike protein 1. *Signal transduction and targeted therapy* **2021**, *6* (1), 1-4.

(18) Schmitz, A.; Weber, A.; Bayin, M.; Breuers, S.; Fieberg, V.; Famulok, M.; Mayer, G. A SARS-CoV-2 Spike Binding DNA Aptamer that Inhibits Pseudovirus Infection by an RBD-Independent Mechanism. *Angewandte Chemie International Edition* **2021**, *60* (18), 10279-10285.

(19) Song, Y.; Song, J.; Wei, X.; Huang, M.; Sun, M.; Zhu, L.; Lin, B.; Shen, H.; Zhu, Z.; Yang, C. Discovery of aptamers targeting the receptor-binding domain of the SARS-CoV-2 spike glycoprotein. *Analytical chemistry* **2020**, *92* (14), 9895-9900.

(20) Zhang, Z.; Li, J.; Gu, J.; Amini, R.; Stacey, H.; Ang, J.; White, D.; Filipe, C.; Mossman, K.; Miller, M. A Universal DNA Aptamer that Recognizes Spike Proteins of Diverse SARS-CoV-2 Variants of Concern. *Chemistry–A European Journal*.

(21) Sun, M.; Wu, Z.; Zhang, J.; Chen, M.; Lu, Y.; Yang, C.; Song, Y. Spherical neutralizing aptamer suppresses SARS-CoV-2 Omicron escape. *Nano today* **2022**, *44*, 101499.

(22) Wang, T.; Yin, W.; AlShamaileh, H.; Zhang, Y.; Tran, P. H.-L.; Nguyen, T. N.-G.; Li, Y.; Chen, K.; Sun, M.; Hou, Y. A detailed protein-SELEX protocol allowing visual assessments of individual steps for a high success rate. *Human gene therapy methods* **2019**, *30* (1), 1-16.

(23) Zadeh, J. N.; Steenberg, C. D.; Bois, J. S.; Wolfe, B. R.; Pierce, M. B.; Khan, A. R.; Dirks, R. M.; Pierce, N. A. NUPACK: Analysis and design of nucleic acid systems. *Journal of computational chemistry* **2011**, *32* (1), 170-173.

(24) Wang, X.; Mei, Z.; Wang, Y.; Tang, L. Gold nanorod biochip functionalization by antibody thiolation. *Talanta* **2015**, *136*, 1-8.

(25) Crawford, K. H.; Eguia, R.; Dingens, A. S.; Loes, A. N.; Malone, K. D.; Wolf, C. R.; Chu, H. Y.; Tortorici, M. A.; Veesler, D.; Murphy, M. Protocol and reagents for pseudotyping lentiviral particles with SARS-CoV-2 spike protein for neutralization assays. *Viruses* **2020**, *12* (5), 513.

(26) Madeira, F.; Pearce, M.; Tivey, A.; Basutkar, P.; Lee, J.; Edbali, O.; Madhusoodanan, N.; Kolesnikov, A.; Lopez, R. Search and sequence analysis tools services from EMBL-EBI in 2022. *Nucleic Acids Research* **2022**.

(27) Lauring, A. S.; Tenforde, M. W.; Chappell, J. D.; Gaglani, M.; Ginde, A. A.; McNeal, T.; Ghamande, S.; Douin, D. J.; Talbot, H. K.; Casey, J. D.; et al. Clinical severity of, and

effectiveness of mRNA vaccines against, covid-19 from omicron, delta, and alpha SARS-CoV-2 variants in the United States: prospective observational study. *BMJ* **2022**, *376*, e069761. DOI: 10.1136/bmj-2021-069761.

(28) Valero, J.; Civit, L.; Dupont, D. M.; Selnihhin, D.; Reinert, L. S.; Idorn, M.; Israels, B. A.; Bednarz, A. M.; Bus, C.; Asbach, B. A serum-stable RNA aptamer specific for SARS-CoV-2 neutralizes viral entry. *Proceedings of the National Academy of Sciences* **2021**, *118* (50).

Supplementary Information

Supplementary Tables

Table S3.1. SELEX conditions. T indicates 0.1 mg/mL yeast tRNA; S indicates 0.1 mg/mL salmon sperm DNA; volume indicates amount of His-Tag Isolation Dynabeads™.

Round	**Aptamer pool (nM)**	**Binding conditions**	**Negative Selection**	**Time (min)**	**Positive Selection**	**Time (min)**
1	5000	0.1% BSA, T	-	-	50 nM S1, 50 µL	60
2	427	0.25% BSA, T	10 µL	30	40 nM S1, 40 µL	30
3	250	0.5% BSA, T	10 µL	30	30 nM S1, 30 µL	30
4	200	1% BSA, T, S	10 µL	30	30 nM S1, 30 µL	30
5	150	1% BSA, T, S	30 µL	30	30 nM S1, 30 µL	30
6	100	1% BSA, T, S	5 nM NTD, 10 µL	30	30 nM S1, 30 µL	30
7	100	1.5% BSA, T, S	20 nM NTD, 20 µL	30	20 nM S1, 20 µL	30

Table S3.2. Aptamer sequences. See methods for list of modifications. A1 through A4: N40 random region underlined, constant region bolded.

Name	**Sequence**
SP6.51	5'-GATATCAACCCATGGTAGGTATTGCTTGGTAGGGATAGTGGGCTTGATGTT-3'
SNAP1	5'-TCGCTCTTTCCGCTTCTTCGCGGTCATTGTGCATCCTGACTGACCCTAAGGTGCGAACATCGCCCGCGTAAGTCCGTGTGTGCGAA-3'
SNAP4.74	5'-CCGTGACGCAGCAAGGGTATTGGCAGTGGTAGGTACTGCGTGCGTTGTGGTTCTAGCATGTTTAATGGACACGG-3'
A1	5'-**TCGCTCTTTCCGCTTCTTCGCGG**GTTGAAAACACTAGAAACTTAATGGGTGCACATAAAACTA**CCGCGTAAGTCCGTGTGTGCGAA**-3'
A2	5'-**TCGCTCTTTCCGCTTCTTCGCGG**AGTATAATGGTAGTACATCATCAAAAGTTTGGGTAACTGT**CCGCGTAAGTCCGTGTGTGCGAA**-3'
A3, SCORe	5'-**TCGCTCTTTCCGCTTCTTCGCGG**AGTAGTATATCGTGGTATCAAAAGCCGGGGGGGCTGTACT**CCGCGTAAGTCCGTGTGTGCGAA**-3'
A4	5'-**TCGCTCTTTCCGCTTCTTCGCGG**TCTGAGTATCTATGATCAAAAGTGTGTAGCACTGTCAGGG**CCGCGTAAGTCCGTGTGTGCGAA**-3'
SCORe.50	5'-CGCGGAGTAGTATATCGTGGTATCAAAAGCCGGGGGGGCTGTACTCCGCG-3'
SNAP1.50	5'-CGCGGTCATTGTGCATCCTGACTGACCCTAAGGTGCGAACATCGCCCGCG-3'
SCORe.50-12T	5'-GTTTTTTTTTTTTCGCGGAGTAGTATATCGTGGTATCAAAAGCCGGGGGGGCTGTACTCCGC-3'
SCORe.50-12A	5'-GAAAAAAAAAAAACGCGGAGTAGTATATCGTGGTATCAAAAGCCGGGGGGGCTGTACTCCGC-3'
SCORe.50-20T	5'-GTTTTTTTTTTTTTTTTTTTTCGCGGAGTAGTATATCGTGGTATCAAAAGCCGGGGGGGCTGTACTCCGC-3'
SCORe.50-20A	5'-GAAAAAAAAAAAAAAAAAAAACGCGGAGTAGTATATCGTGGTATCAAAAGCCGGGGGGGCTGTACTCCGC-3'
SCORe.50-30T	5'-GTTTTTTTTTTTTTTTTTTTTTTTTTTTTTTCGCGGAGTAGTATATCGTGGTATCAAAAGCCGGGGGGGCTGTACTCCGC-3'
SCORe.50-30A	5'-GAAAAAAAAAAAAAAAAAAAAAAAAAAAAAACGCGGAGTAGTATATCGTGGTATCAAAAGCCGGGGGGGCTGTACTCCGC-3'
SNAP1.50-30T	5'-GTTTTTTTTTTTTTTTTTTTTTTTTTTTTTTCGCGG

	TCATTGTGCATCCTGACTGACCCTAAGGTGCGAACATCGCCCGC-3'
SNAP1.50-30A	5'-GAAAAAAAAAAAAAAAAAAAAAAAAAAAAAACGCGG TCATTGTGCATCCTGACTGACCCTAAGGTGCGAACATC GCCCGC-3'

Supplementary Figures

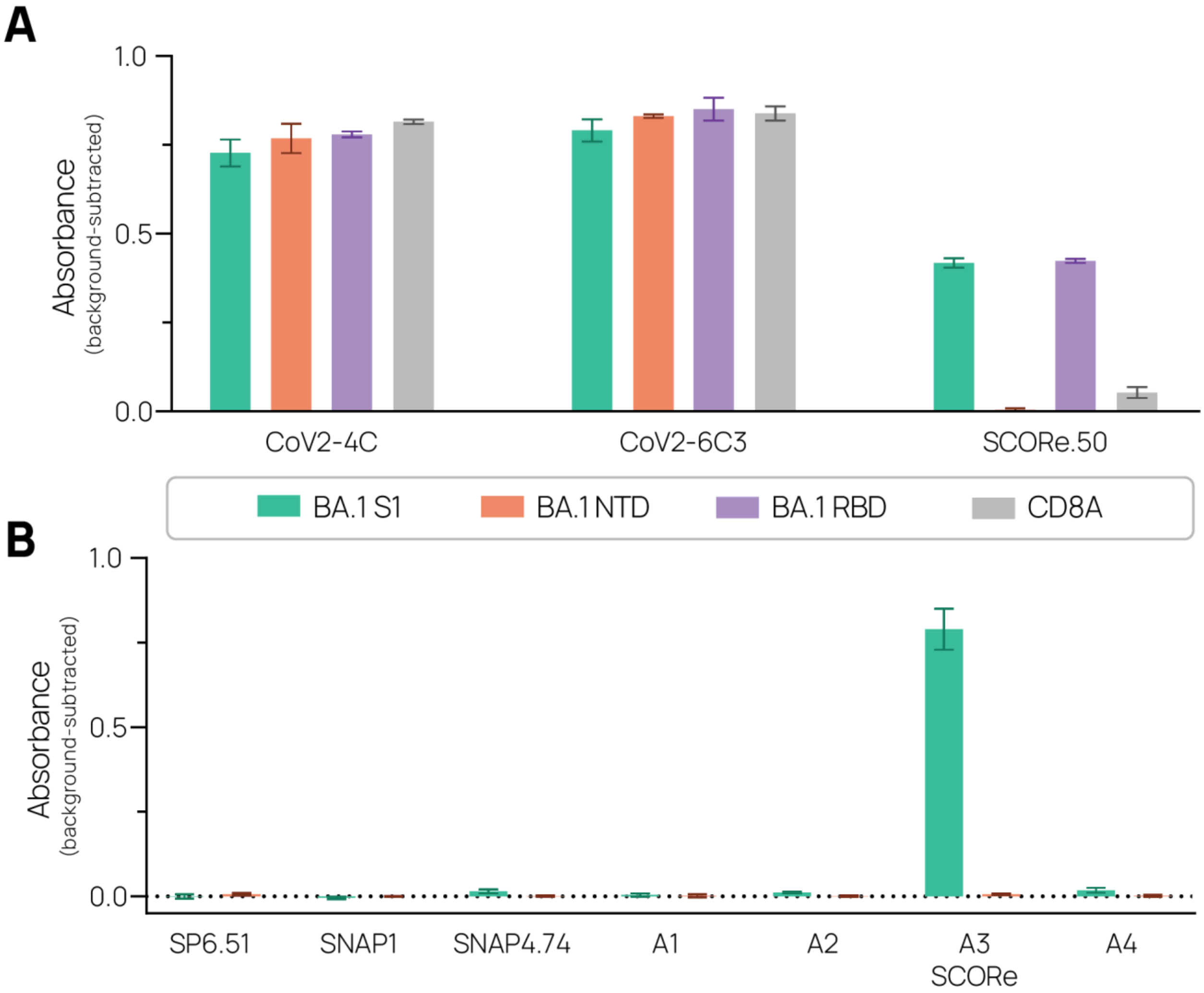

Figure S3.1. Preliminary binding screening. SARS-CoV-2 Omicron (BA.1) S1, BA.1 NTD, BA.1 RBD, or CD8A (negative control protein) His-tagged proteins were adsorbed onto plates then incubated with biotinylated aptamers (x-axis label). Streptavidin-HRP and colorimetric substrate were added and absorbance was measured. Data was background subtracted, bar is mean, and bracket is S.D. Three technical replicates are shown.

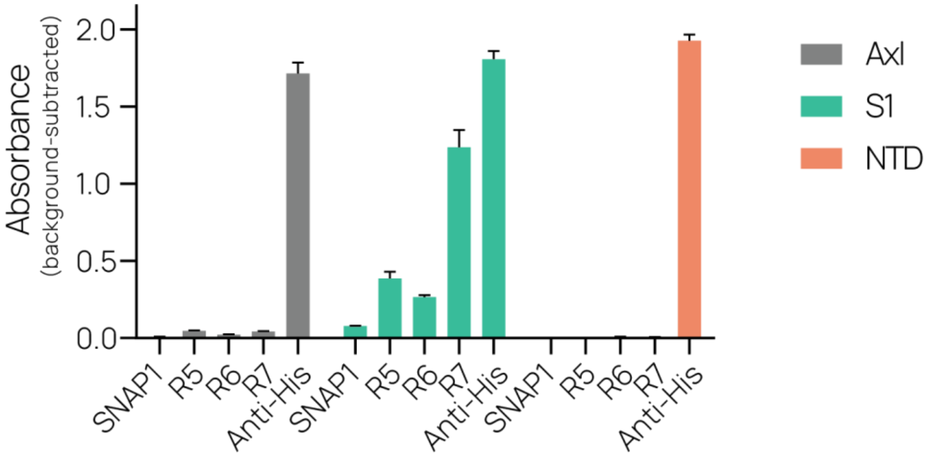

Figure S3.2. Aptamer round binding study. SARS-CoV-2 Omicron (BA.1) S1, NTD, or Axl (negative control) His-tagged proteins were adsorbed onto plates then incubated with negative control aptamer (SNAP1-FITC), positive control (FITC-labeled anti-His antibody), or FITC-labeled aptamer libraries. Anti-FITC HRP and colorimetric substrate were added and absorbance was measured. Data was background subtracted, bar is mean, and bracket is S.D. Three technical replicates are shown.

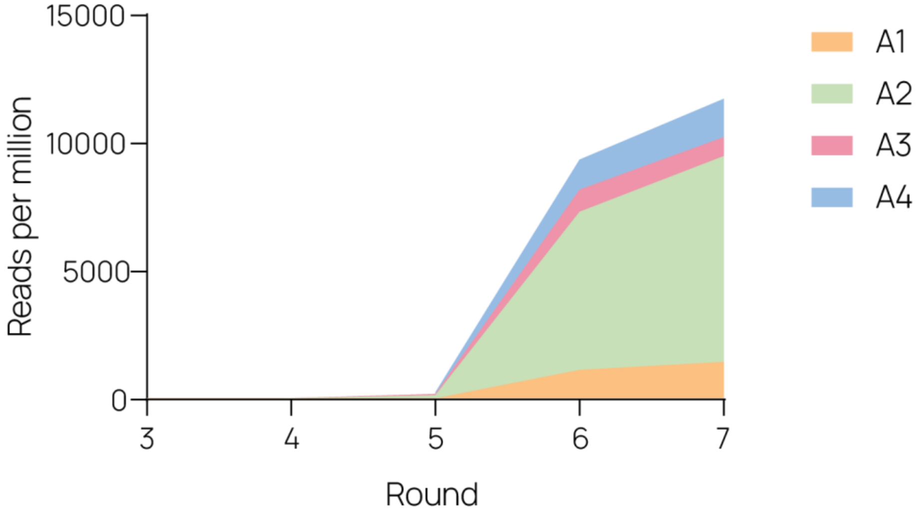

Figure S3.3. Prevalence of aptamers in SELEX rounds 3 through 7 measured by reads per million (RPM).

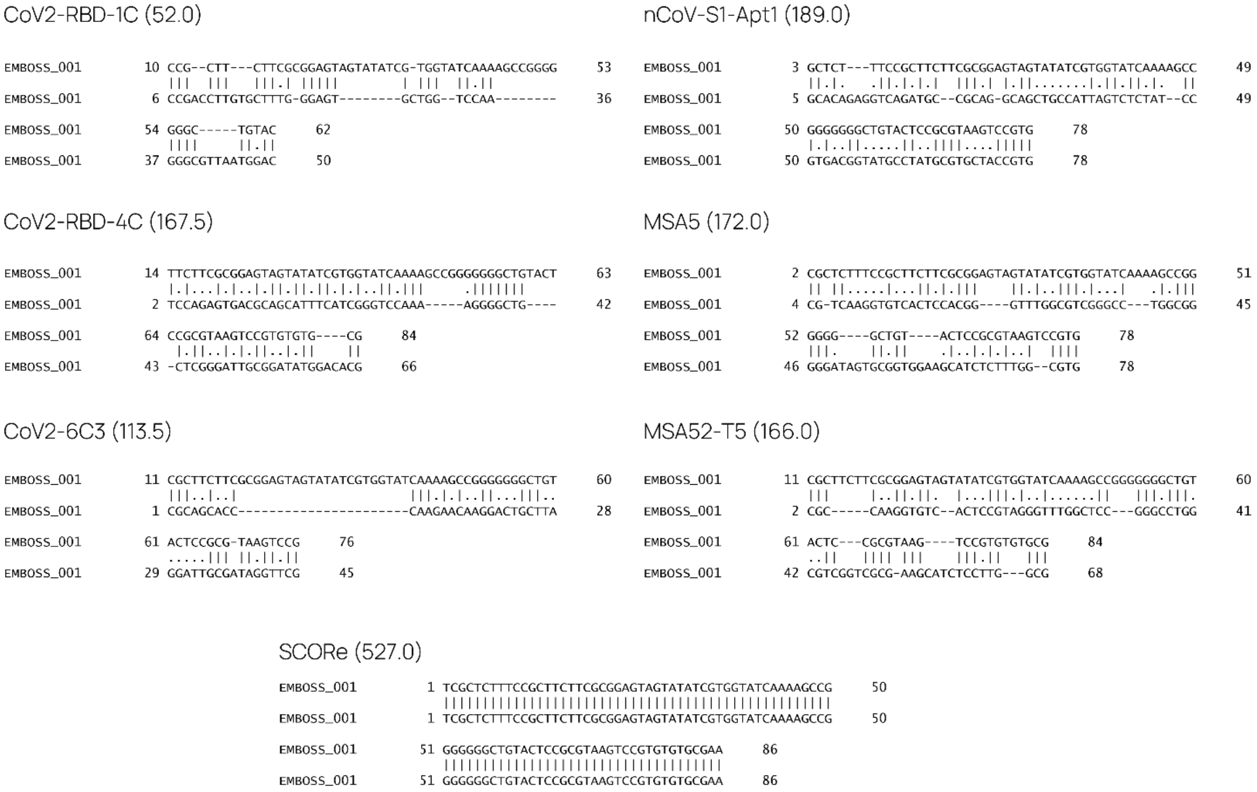

CoV2-RBD-1C (52.0)

```
EMBOSS_001        10 CCG--CTT---CTTCGCGGAGTAGTATATCG-TGGTATCAAAAGCCGGGG     53
                     |||  |||   |||.| |||||        | |||  ||.||
EMBOSS_001         6 CCGACCTTGTGCTTTG-GGAGT--------GCTGG--TCCAA--------     36

EMBOSS_001        54 GGGC-----TGTAC     62
                     ||||     ||.||
EMBOSS_001        37 GGGCGTTAATGGAC     50
```

CoV2-RBD-4C (167.5)

```
EMBOSS_001        14 TTCTTCGCGGAGTAGTATATCGTGGTATCAAAAGCCGGGGGGGCTGTACT     63
                     |.|...|.|..|.||.||.||.|.|..||.|||     .|||||||
EMBOSS_001         2 TCCAGAGTGACGCAGCATTTCATCGGGTCCAAA-----AGGGGCTG----     42

EMBOSS_001        64 CCGCGTAAGTCCGTGTGTG----CG     84
                      |.||..|.|.||..|.||    ||
EMBOSS_001        43 -CTCGGGATTGCGGATATGGACACG     66
```

CoV2-6C3 (113.5)

```
EMBOSS_001        11 CGCTTCTTCGCGGAGTAGTATATCGTGGTATCAAAAGCCGGGGGGGCTGT     60
                     |||..|..|                      |||.|.|..||...|||..
EMBOSS_001         1 CGCAGCACC----------------------CAAGAACAAGGACTGCTTA     28

EMBOSS_001        61 ACTCCGCG-TAAGTCCG     76
                     .....||| ||.||.||
EMBOSS_001        29 GGATTGCGATAGGTTCG     45
```

nCoV-S1-Apt1 (189.0)

```
EMBOSS_001         3 GCTCT---TTCCGCTTCTTCGCGGAGTAGTATATCGTGGTATCAAAAGCC     49
                     ||.|.   .||.|.|.|  |||.| |.||.......|.||.||.|.  ||
EMBOSS_001         5 GCACAGAGGTCAGATGC--CGCAG-GCAGCTGCCATTAGTCTCTAT--CC     49

EMBOSS_001        50 GGGGGGGCTGTACTCCGCGTAAGTCCGTG     78
                     |.|..||.....||..||||....|||||
EMBOSS_001        50 GTGACGGTATGCCTATGCGTGCTACCGTG     78
```

MSA5 (172.0)

```
EMBOSS_001         2 CGCTCTTTCCGCTTCTTCGCGGAGTAGTATATCGTGGTATCAAAAGCCGG     51
                     || ||.....|...||.|.|||    ||.|..|||.|...|   .|.|||
EMBOSS_001         4 CG-TCAAGGTGTCACTCCACGG----GTTTGGCGTCGGGCC---TGGCGG     45

EMBOSS_001        52 GGGG----GCTGT----ACTCCGCGTAAGTCCGTG     78
                     |||.    ||.||    .|..|.|.|..|  ||||
EMBOSS_001        46 GGGATAGTGCGGTGGAAGCATCTCTTTGG--CGTG     78
```

MSA52-T5 (166.0)

```
EMBOSS_001        11 CGCTTCTTCGCGGAGTAGTATATCGTGGTATCAAAAGCCGGGGGGGCTGT     60
                     |||     |..||.||.  |...|||.|..|......||   |||.|||.
EMBOSS_001         2 CGC-----CAAGGTGTC--ACTCCGTAGGGTTTGGCTCC---GGGCCTGG     41

EMBOSS_001        61 ACTC---CGCGTAAG----TCCGTGTGTGCG     84
                     ..||   |||| |||    |||.||   |||
EMBOSS_001        42 CGTCGGTCGCG-AAGCATCTCCTTG---GCG     68
```

SCORe (527.0)

```
EMBOSS_001         1 TCGCTCTTTCCGCTTCTTCGCGGAGTAGTATATCGTGGTATCAAAAGCCG     50
                     ||||||||||||||||||||||||||||||||||||||||||||||||||
EMBOSS_001         1 TCGCTCTTTCCGCTTCTTCGCGGAGTAGTATATCGTGGTATCAAAAGCCG     50

EMBOSS_001        51 GGGGGGCTGTACTCCGCGTAAGTCCGTGTGTGCGAA     86
                     ||||||||||||||||||||||||||||||||||||
EMBOSS_001        51 GGGGGGCTGTACTCCGCGTAAGTCCGTGTGTGCGAA     86
```

Figure S3.4. Local alignment of SCORe to previously reported SARS-CoV-2 RBD binding aptamers. SCORe was compared to each aptamer. Name of aptamer is above each alignment. Alignment score is in paranthesis.

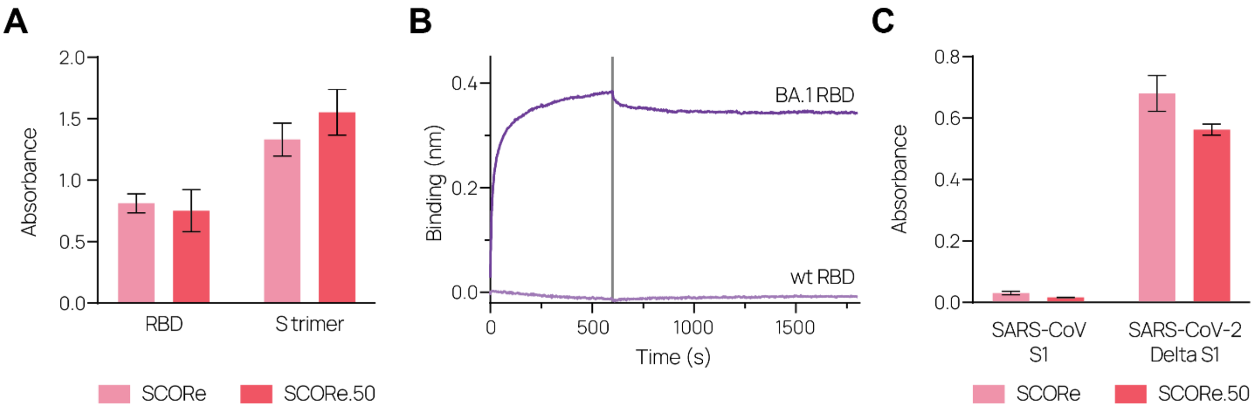

Figure S3.5. A, C) SARS-CoV-2 proteins adsorbed onto surface are incubated with 100 nM biotinylated aptamer and stained with streptavidin-HRP with detection of the HRP substrate TMB quantified by UV absorbance measurements. Bars indicate mean, brackets indicate S.D., n = 3. B) Biolayer interferometry assessment of binding. Wild-type or BA.1 SARS-CoV-2 RBD was loaded on Ni-NTA biosensors and associated with 500 nM of SCORe-FITC. The gray line indicates the switch from analyte association to dissociation at 600 s.

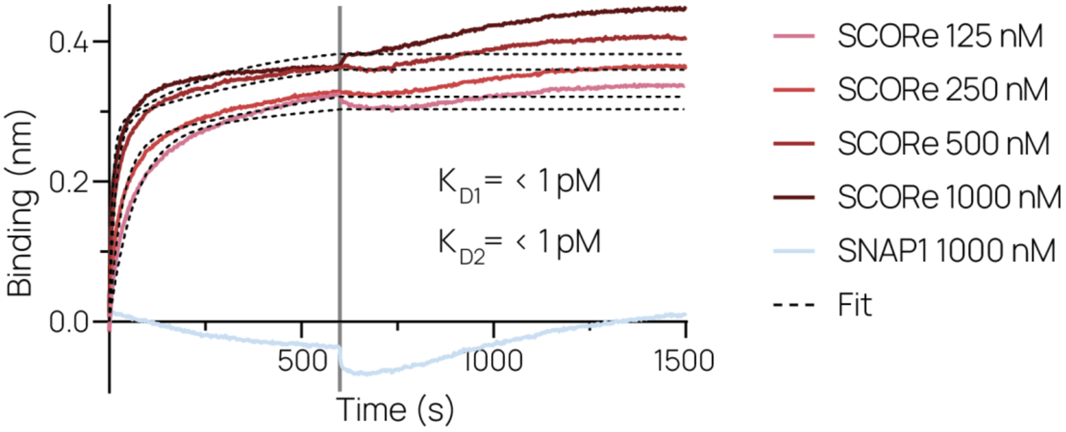

Figure S3.6. Biolayer interferometry assessment of binding with nasal swab in buffer. Wild-type or BA.1 SARS-CoV-2 RBD was loaded on Ni-NTA biosensors and associated with 125 to 1000 nM of SCORe-FITC or 1000 nM SNAP1-FITC. The gray line indicates the switch from analyte association to dissociation at 600 s. A global fit (dotted line) of the kinetic data at various concentrations of SCORe for a 2:1 binding model was determined.

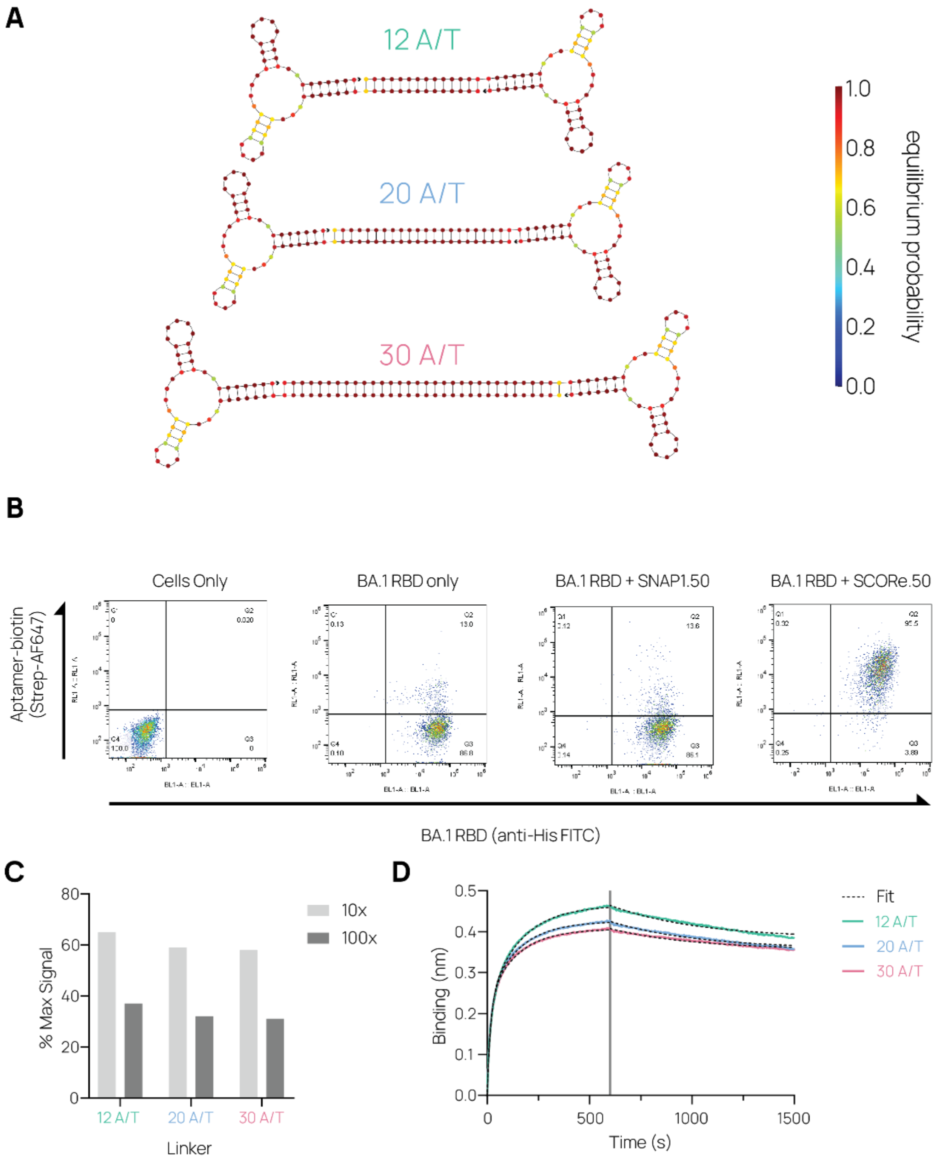

Figure S3.7. A) Secondary structure prediction with the following conditions: 22ºC, 137 mM Na$^+$, 5.5 mM Mg^{++}. Arrows represent the 3' end of the aptamer. B) Co-staining of HEK293 ACE2 cells with BA.1 RBD and aptamers. C) ACE2-overexpressing HEK293 cells were incubated with 25 nM Omicron (BA.1) S protein and indicated dimer. S protein binding was measured by flow cytometry. One technical replicate shown. Legend shows aptamer concentration with fold molar excess of dimer to S protein. D) BLI characterization of SCORe.50 dimers binding to immobilized RBD. His-tagged RBD was loaded on Ni-NTA biosensors and associated with 250 nM dimer. The gray line indicates the switch from analyte association to dissociation after 600 s.

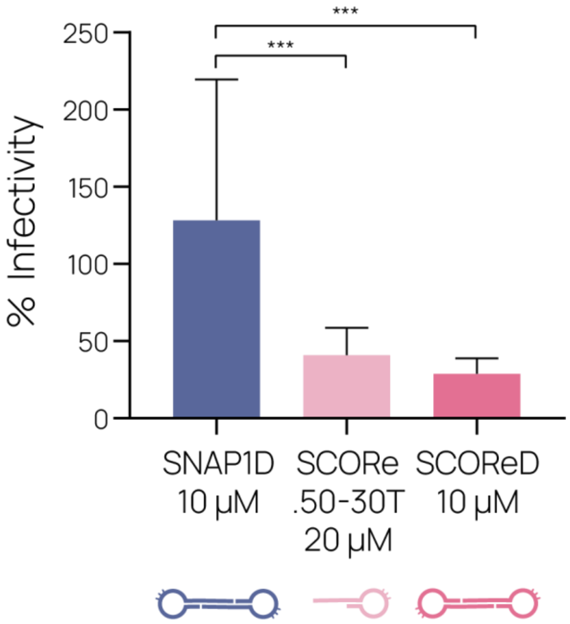

Figure S3.8. Omicron S pseudotyped virus infection of ACE2-overexpressing HEK293 cells in the presence of various aptamer constructs. Three biological replicates performed with four technical replicates each shown. Bars represent mean, brackets represent S.D. *** denotes $p < 0.001$ as determined by 2-way ANOVA with Dunnett's multiple comparison test.

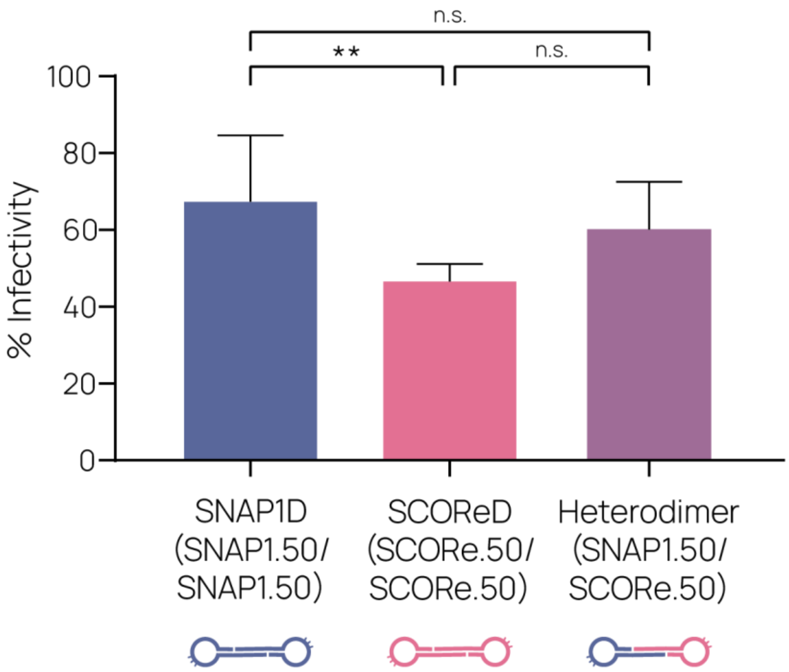

Figure S3.9. Omicron S pseudotyped virus infection of ACE2-overexpressing HEK293 cells in the presence of various aptamer constructs at 10 μM. Three biological replicates performed with four technical replicates each shown. Bars represent mean, brackets represent S.D. "n.s." denotes no significance and ** denotes $p < 0.01$ as determined by 2-way ANOVA with Dunnett's multiple comparison test.

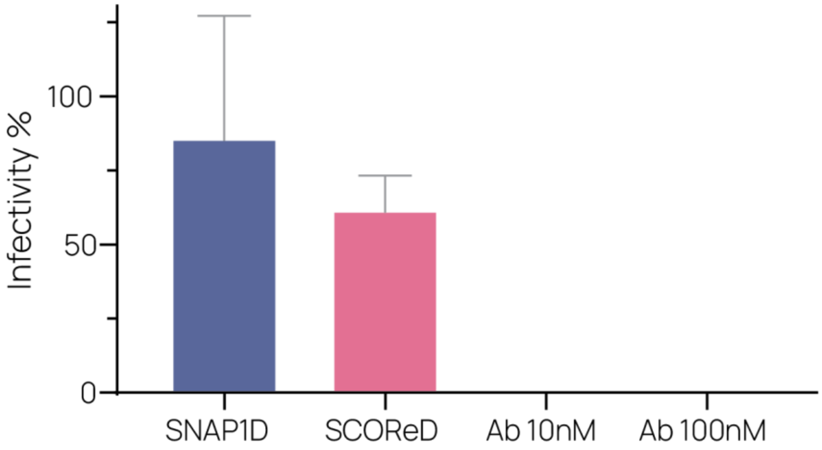

Figure S3.10. Omicron S pseudotyped virus infection of ACE2-overexpressing HEK293 cells in the presence of 10 μM SNAP1D, 10 μM SCOReD, or 10 – 100 nM neutralizing anti-RBD antibody. Four technical replicates shown. Bars represent mean, brackets represent S.D.

Chapter 4

Delivery of EGCG via boronic acid polymer for inhibiting fibrosis in CKD

Unpublished work

Lucy F. Yang, Kefan Song, Alex Prossnitz, Ben Nguyen, Joey Liang, Suzie H. Pun

Abstract

Chronic kidney disease (CKD) impacts 37 million people in the U.S., many of which require dialysis or kidney transplants to survive. Renal fibrosis irreversibly scars tissue and results in loss of function. Renal proximal tubular epithelial cells (TECs) have recently been shown to mediate fibrosis. After injury, TECs undergo epithelial-to-mesenchymal (EMT) transition, becoming more mobile and releasing transcription factors that promote fibrosis. Snail1, one of these transcription factors, has been shown to induce EMT and fibrosis in the kidney. The main active compound in green tea, epigallocatechin-3-gallate (EGCG) has been reported to inhibit EMT in renal tubular cells through two pathways, including one that uses Snail1. We have previously developed two different polymers whose principles can be applied to make a drug delivery vehicle of EGCG to TECs: (A) we observed accumulation of low-molecular weight, highly anionic polymers in proximal TECs; (B) we developed boronic acid-containing polymer-drug conjugates with pH-dependent reversible release for experimental kidney disease treatment. Conveniently, EGCG contains two catechol units and can be conjugated to boronic acid. We propose to deliver EGCG to TECs as a potential treatment for CKD by designing a new polymer has the TEC-accumulating properties by design and boronic acid by composition.

Introduction

Chronic kidney disease (CKD) is a serious healthcare burden with no curative treatment. In CKD, the kidneys progressively lose function because of injury and fibrosis, leading to a decrease in the glomerular filtration rate (GFR). Although about 15% of U.S. adults have CKD[1], the disease often goes unnoticed until symptoms appear when kidney function is greatly impaired[2]. At that point, it leads to end-stage renal disease (ESRD) and the only therapies available are dialysis or kidney organ transplantation. However, chronic dialysis is costly and detrimental to daily life, and donor kidneys are in short supply[2]. Thus, more effective treatments for CKD are needed[3].

On a pathogenic level, CKD is caused by maladaptive injury response. Chronic or severe injuries corrupt repair pathways meant to heal, leading to inflammation and fibrosis. However, the cellular origins of renal myofibroblasts and collagen in fibrosis are not well understood[4]. Several cell types execute maladaptive injury responses, including epithelial cells, myofibroblasts, endothelial cells, and immune cells[5]. Recently, tubular epithelial cells (TECs) that undergo a epithelial to mesenchymal transition (EMT) are suspected as mediators of renal fibrosis[4,6]. During EMT, cells become mobile, lose epithelial markers, like e-cadherin and zonula occludens-1 (ZO-1), and gain mesenchymal markers, such as vimentin and alpha-SMA. TECs that undergo EMT no longer retain their regular functions and are suspected to become myofibroblasts[5]. These changes are orchestrated by EMT-inducing transcription factors like Snail1. Targeted downregulation of Snail1 can revert fibrosis[7] and is a potential method for inhibiting CKD. Epigallocatechin-3-gallate (EGCG) is the active compound in green tea and has anti-fibrotic properties effective in several diseases[8–14]. In relation to CKD, EGCG has been reported to inhibit EMT in renal tubular cells through two pathways, including one that uses Snail1[15]. Thus, delivering EGCG to TECs could be a strategy to attenuate fibrosis in CKD.

We propose to incorporate EGCG in a boronic acid-based polymeric delivery vehicle for targeted delivery to renal TECs as a potential treatment for CKD. Previously, we have demonstrated that anionic polymers of 25 kDa molecular weight preferentially accumulate in kidney proximal tubule cells[16]. In addition, we have shown that boronic acid-functionalized polymers can deliver catechol-containing drug Bis-T-23 into kidney cells[17]. EGCG contains two catechols and is therefore highly suitable for conjugation to a boronic acid polymer. In ongoing work, we are confirming that EGCG given in solution inhibits TGFB-1 induced EMT in human tubular epithelial cells by measuring gene and protein expression of vimentin, alpha-SMA, ZO-1, and Snail1. We are designing and characterizing boronic acid polymers with the size and charge properties shown to accumulate in proximal tubule cells. We plan to test these polymers in efficacy and toxicity studies in cells and CKD model animals.

Results, Discussion, and Ongoing Work

Screening anti-fibrotic drugs

We initially screened several different drugs (Fig. 4.1) that demonstrated anti-fibrotic properties: (1) harmol, a Twist1 inhibitor with demonstrated anti-tumor activity in non-small cell lung cancers[18], and (2) celastrol, an active compound in thunder god vine root extracts with anti-inflammatory and anti-cancer properties[19,20]. However, in our hands, these did not reduce TGF-β1-induced EMT in HK-2 cells (data not shown). We present our positive and reproducible findings of EGCG's ability to reduce TGF-β1-induced EMT in HK-2 cells.

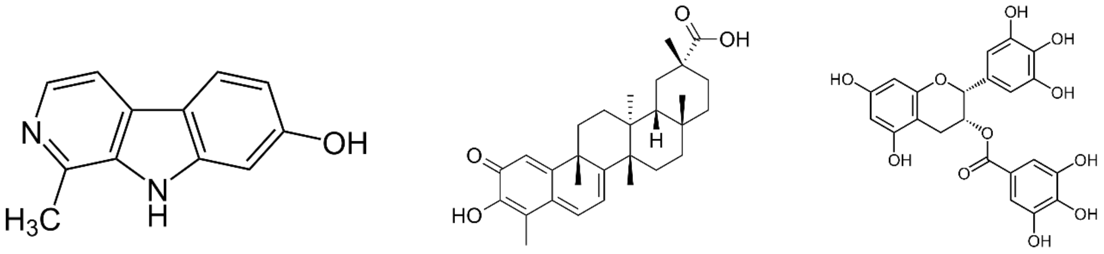

Figure 4.1 Chemical structures of candidate drugs. Left: harmol, middle: celastrol: right: EGCG.

Effect of EGCG treatment on HK-2 cell viability

We first assessed viability of HK-2 cells, a human proximal tubular cell line, treated with EGCG to determine the dosing strategy (Fig. 4.2). We observed that up to 10 µM EGCG did not decrease cell viability significantly. The IC_{50} was 63 µM, so we chose 5, 10, and 40 µM as concentrations for further studies.

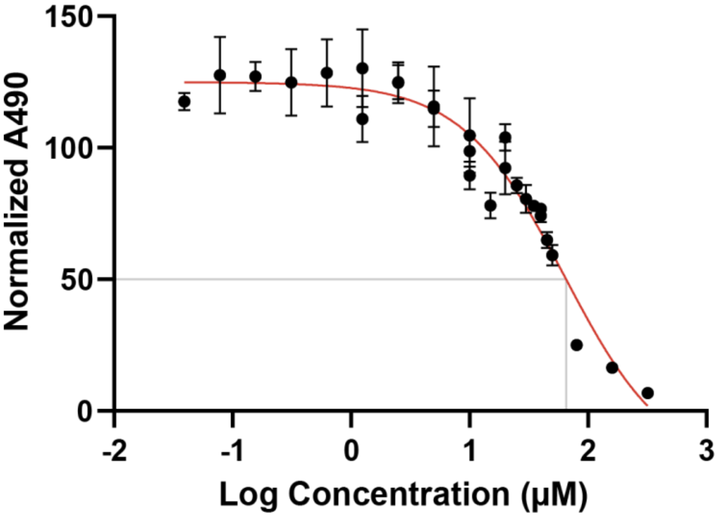

Figure 4.2 Viability assay of EGCG on HK-2 cells. Non-linear regression (Dose-Response – Inhibition) of three biological replicates conducted in technical triplicates.

Effect of EGCG treatment on gene expression in HK-2 cells undergoing EMT

Next, we tested whether TGF-β1 could induce EMT in HK-2 cells. We dosed TGF-β1 at different concentrations and observed that 5 ng/mL or higher doubled *vimentin* (an intermediate filament protein) expression compared to untreated cells (Fig. 4.3). As a preliminary experiment, we also treated cells with 40 µM EGCG and observed roughly 8-fold decrease in *vimentin* expression despite TGF-β1. The decrease in a mesenchymal marker's expression indicates that the earlier report of EGCG as an anti-fibrotic drug for kidney cells[15] was reproducible.

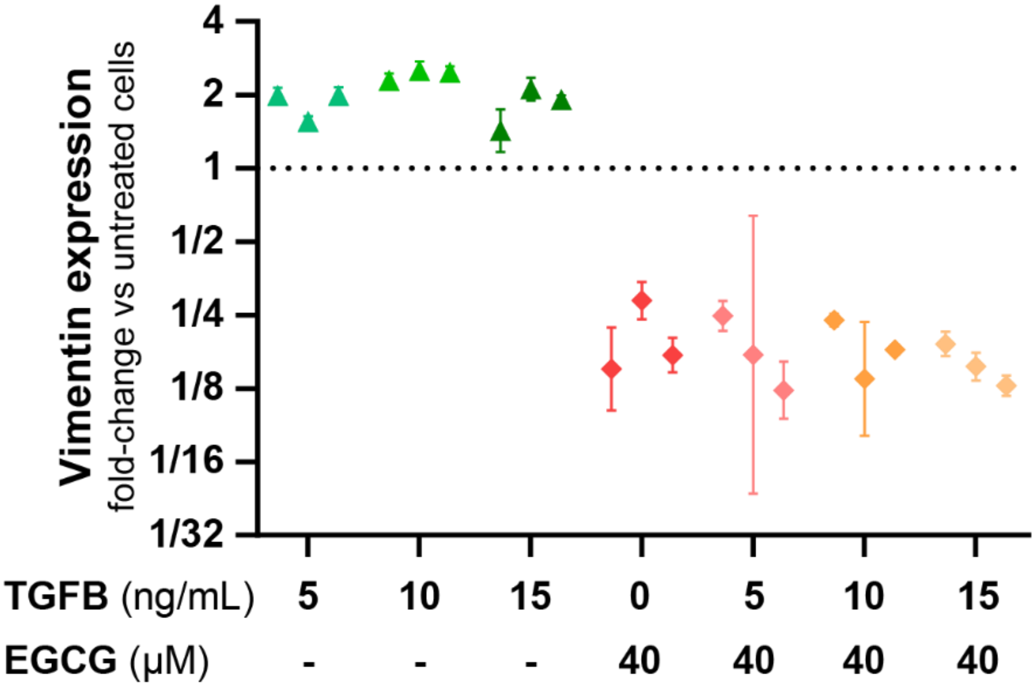

Figure 4.3 Pilot study for vimentin gene expression in HK-2 cells treated with different concentrations of TGF-β1 and EGCG. Non-linear regression (Dose-Response – Inhibition) of three biological replicates conducted in technical triplicates.

To further confirm that EGCG could inhibit TGF-β1-induced EMT, we dosed cells with different concentrations of EGCG and measured expression of other genes. We first measured change in gene expression of epithelial marker *e-cadherin* (a cell adhesion molecule important to retaining epithelial characteristics) and mesenchymal markers *vimentin*, *alpha-SMA* (an isoform of actin involved in smooth muscle contraction) and *Twist1* (a transcription factor that promotes EMT). We were unable to measure C_T values of *e-cadherin* and *alpha-SMA* (data not shown). This could be due to inherently low expression of E-cadherin in HK-2 cells or poor choice of qPCR primers despite testing several pairs. We observed a concentration-dependent decrease in *vimentin* and *Twist1* expression in cells treated with EGCG (Fig. 4.4). Cells treated with only TGF-β1 had 5.3-fold higher expression of *vimentin* compared to untreated cells. When cells were treated with TGF-β1 and 40 µM EGCG, their *vimentin* expression was 6.3-fold lower than untreated. A similar pattern was observed for *twist1* expression: Cells treated with only TGF-β1 had 4.1-fold higher *Twist1* expression, but cells treated with TGF-β1 and 40 µM EGCG expressed 13.6-fold less *Twist1* than untreated cells. We also observed a decrease in both mesenchymal markers measured even when cells were not treated with TGF-β1. Although the HK-2 cell line is epithelial, cultured epithelial cell lines tend to become mesenchymal over time and Vimentin staining is observed in regular HK-2 cells[21]. This could explain why EGCG being effective at reducing *vimentin* and *Twist1* expression with cells that weren't induced by TGF-β1. Overall, these data indicate that EGCG may be a potent inhibitor of EMT.

In future work, we will repeat the aforementioned studies for additional biological replicates. We will also measure the expression of additional markers, such as *ZO-1* and *snail1*, by designing and testing additional qPCR primers.

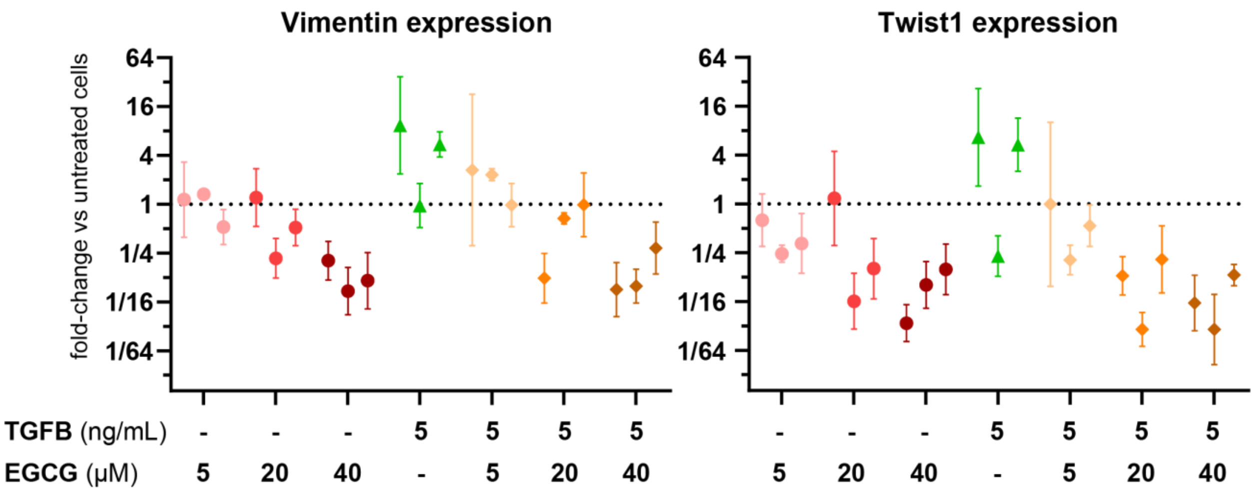

Figure 4.4 Change in gene expression after treatment with TGF-β1 and EGCG. HK-2 cells were pre-treated with EGCG then induced to undergo EMT with TGF-β1. Data points indicate one set of technical triplicates. Bars indicate range. Dotted line indicates no change compared to untreated cells. One biological replicate shown.

Effect of EGCG treatment on protein expression in HK-2 cells undergoing EMT

We are conducting Western blots to measure protein expression of epithelial and mesenchymal markers. In initial experiments, we observed bright staining with GAPDH, Vimentin, ZO-1, and Snail1 (Fig 4.4). For Twist1, we observed non-specific staining. We were not able to see protein band staining for E-cadherin or alpha-SMA. So far, our experiments have not been consistent between Western blot replicates or gene expression observations (data not shown). In ongoing work, we are optimizing the

Western blot protocol by testing different drug incubation times, BSA versus non-fat milk blocking, different concentrations of secondary antibody, and different primary antibodies.

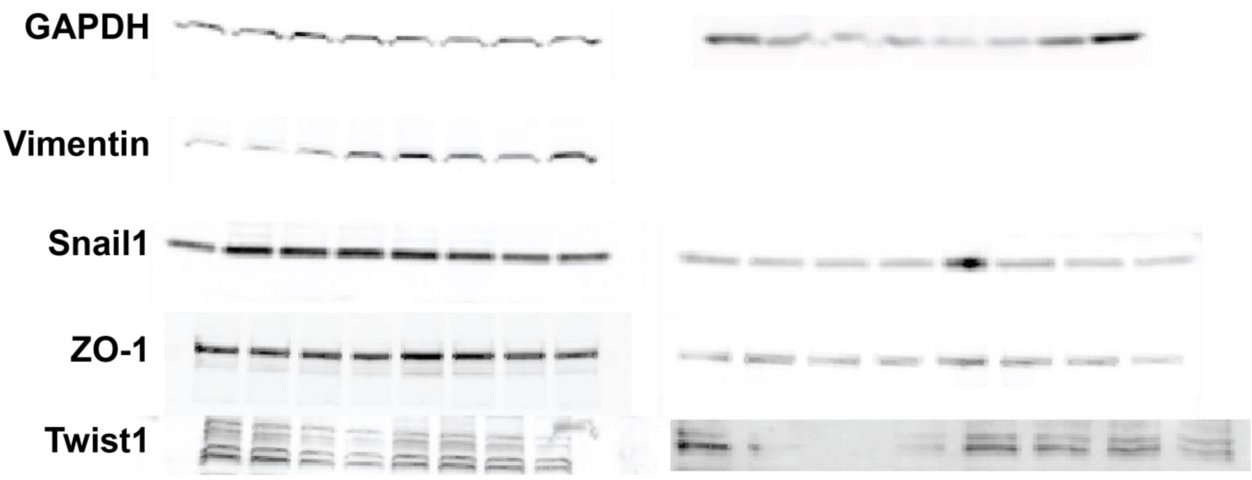

Figure 4.4 Preliminary Western blot images. Example blots taken from 4 different experiments. Lanes from left to right are: untreated, 5 µM EGCG, 20 µM EGCG, 40 µM EGCG, 5 ng/mL TGF-β1 only, 5 ng/mL TGF-β1 + 5 µM EGCG, 5 ng/mL TGF-β1 + 20 µM EGCG, and 5 ng/mL TGF-β1 + 40 µM EGCG.

Synthesis of EGCG-conjugated polymers

After initial validation of the anti-fibrotic potential of EGCG, we plan to synthesize a polymer with epithelial cell-targeting properties. First, we will synthesize an anionic polymethacrylamide base polymer (Fig. 4.5) Improving upon our previous study[16], we will use reversible addition−fragmentation chain-transfer (RAFT) polymerization[22] instead of atom transfer radical polymerization (ATRP)[23]. RAFT and ATRP both rely on reversible deactivation of a radical to propagate the polymer, but RAFT typically gives lower polydispersity polymers and higher conversion. After polymerization, we will conjugate boronic acid to the polymer by EDC/NHS coupling (Fig. 4.6). We have previously shown post-polymerization modification of polymethacrylamides with boronic acid functional groups[17], which allows adjustment of polymer physical properties without redoing the polymerization. Loading of catechol-containing EGCG onto boronic acid groups is a fast reaction at high concentrations of drug. It is also quick to dialyze to remove free EGCG and measure conjugation efficiency by absorbance at 312 nm.

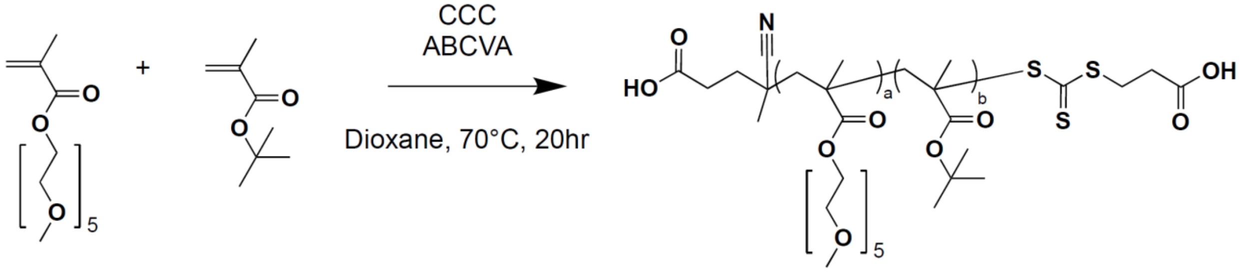

Figure 4.5 RAFT polymerization scheme. The chain transfer agents (CTAs) are 4-((((2-carboxyethyl)thio)carbonothioyl)thio)-4-cyanopentanoic acid (CCC) and azobiscyanovaleric acid (ABCVA).

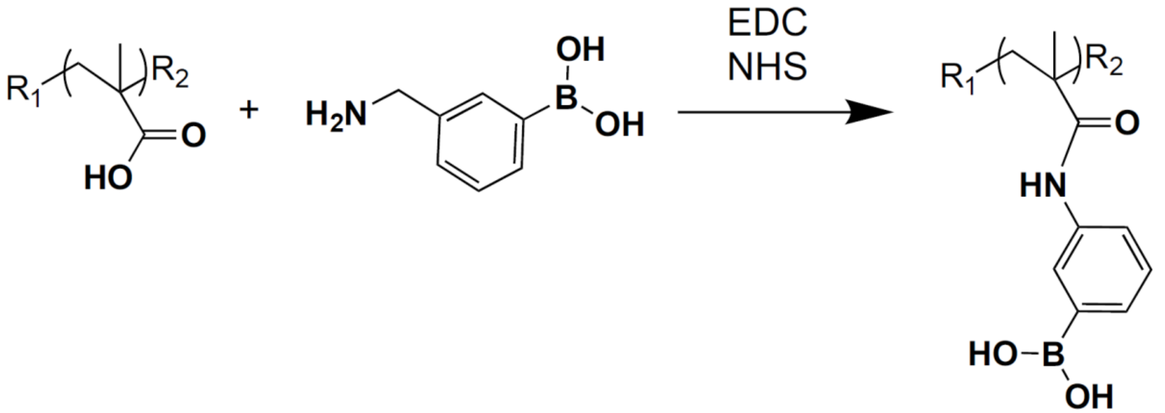

Figure 4.6 Modification of post-polymerization methacrylic acid with boronic acid.

Effect of EGCG-polymer on gene and protein expressions of HK-2 cells

After synthesis and verification of the polymer composition, we will test whether EGCG-conjugated polymers can reduce TGF-β1-induced EMT in HK-2 cells. We will perform similar experiments as the ones described for EGCG given in solution, including viability, gene expression change, and protein expression change. We expect the polymer-drug conjugate to show reduced potency compared to equivalent molar amount of free EGCG, which can enter the cell through diffusion and receptor-mediated entry[15,24]. Another potential challenge is that anionic polymers may not be taken up by cells readily. We could synthesize a neutral- or positive-charge polymer to overcome the issue.

Effect of EGCG and EGCG-polymer on experimental FSGS mice

While EGCG *in vitro* studies and polymer synthesis are being conducted, we will conduct a pilot animal study with free EGCG. Mice will be given experimental focal segmental glomerular sclerosis (FSGS) induced by a podocyte-targeting antibody[25–27]. FSGS is a disease in which podocytes are depleted, leading to glomerulus incapacitation and ESRD. (A tubule interstitial fibrosis animal model was not readily available at the time of writing.) Starting immediately after disease induction, we will give mice 50 mg/kg EGCG intraperitoneally in saline three times a week for 2-3 weeks, which are conditions that have worked in animal models for other diseases[8–14]. We will also longitudinally collect urine samples and measure its albumin content by radial immunodiffusion assay (RID). RID will quantify the severity of proteinuria, which is a sign of kidney damage. At the end of the study, we will harvest the kidneys for histology and stain for Vimentin, E-cadherin, and alpha-SMA to characterize the extent of fibrosis. We will compare the histology images to previously made slides of untreated animals. We expect that the EGCG may have anti-fibrotic effects on lesions that develop once FSGS progresses into ESRD. We may need to adjust the timing of EGCG treatment, length of study before kidney harvest, and other parameters depending on whether the effect of EGCG on experimental FSGS is observable. If EGCG does not reduce proteinuria or fibrosis in the experimental FSGS model, then we will repeat the study with a tubule interstitial fibrosis animal model.

Lastly, we will test the EGCG-polymer conjugate in an animal study similar to the aforementioned one. We will use unloaded polymer and free EGCG as controls for EGCG-polymer conjugate.

Materials & Methods

Cell culture. HK-2 (human kidney 2) cells were cultured in Keratinocyte SFM (Gibco) at 37^{o}C with 5% CO_2.

MTS assay. 20,000 cells were seeded on a 96-well dish 24h before changing media and adding 0-50 µM EGCG. After 48h, cells were incubated with MTS/PMS (Promega) for 2h. Absorbance at 490mm was measured with an Infinite 200 PRO plate reader (Tecan) then values were background-subtracted.

RT-qPCR. 250,000 cells were seeded in 10cm TC-treated dishes 47h before changing media and adding 0-40 µM EGCG. 1h later, 5 ng/mL TGF- β1 was added to the media. 48h later, cells are harvested and RNA is extracted using TRIzol™ Reagent (Invitrogen) according to manufacturer's protocol. C_T values were measured in technical triplicates. For each gene of interest, the C_T value was subtracted from that of the housekeeping gene, GAPDH. For each treatment group, fold-change was calculated in reference to untreated cells.

Western blot. 250,000 cells were seeded in 10cm TC-treated dishes 47h before changing media and adding 0-40 µM EGCG. 1h later, 5 ng/mL TGF- β1 was added to the media. 24h later, cells are harvested in RIPA buffer (Thermo Scientific™) according to manufacturer's protocol. Concentration of protein in lysates was measured by Pierce™ BCA Protein Assay Kit (Thermo Scientific™) according to manufacturer's protocol. 15 µg of protein in Laemmli sample buffer was loaded onto Invitrogen™ Novex™ WedgeWell™ 4 to 20%, Tris-Glycine, 1.0 mm, Mini Protein Gel, 10-well (Thermo Scientific™) and ran on the XCell SureLock™ Mini-Cell (Invitrogen™) according to manufacturer's protocols.

Proteins were blotted onto PVDF membrane with XCell II™ Blot Module (Invitrogen™) according to manufacturer's protocols. Membranes were stained with 1:1000 dilutions of the following antibodies overnight at 4ºC: Mouse anti-GAPDH D4C6R, Mouse anti-Vimentin 5F3F10, Mouse anti-alpha-SMA 1A4, Mouse anti-E-cadherin 4A2, Rabbit anti-Twist1 46702S, Rabbit anti-ZO-1 D7D12, or Rabbit anti-Snail1 C15D3 (Cell Signaling). Membranes were incubated with 1:5000 dilution of Anti-mouse HRP 115-035-174 (Jackson ImmunoResearch) or anti-rabbit HRP antibody A6154 (Sigma) for 1h. Lastly, membranes were stained with Pierce™ ECL Western Blotting Substrate (Thermo Scientific™) and imaged on a IVIS Xenogen for 1-60s exposure times.

References

1. Johansen, K. L. *et al.* US Renal Data System 2020 Annual Data Report: Epidemiology of Kidney Disease in the United States. *Am. J. Kidney Dis.* **77**, A7–A8 (2021).
2. Kalantar-Zadeh, K., Jafar, T. H., Nitsch, D., Neuen, B. L. & Perkovic, V. Chronic kidney disease. *The Lancet* (2021) doi:10.1016/S0140-6736(21)00519-5.
3. Carney, E. F. The impact of chronic kidney disease on global health. *Nat. Rev. Nephrol.* **16**, 251–251 (2020).
4. Huang, S. & Susztak, K. Epithelial Plasticity versus EMT in Kidney Fibrosis. *Trends Mol. Med.* **22**, 4–6 (2016).
5. Lovisa, S., Zeisberg, M. & Kalluri, R. Partial Epithelial-to-Mesenchymal Transition and Other New Mechanisms of Kidney Fibrosis. *Trends Endocrinol. Metab.* **27**, 681–695 (2016).
6. Qi, R. & Yang, C. Renal tubular epithelial cells: the neglected mediator of tubulointerstitial fibrosis after injury. *Cell Death Dis.* **9**, (2018).
7. Grande, M. T. *et al.* Snail1-induced partial epithelial-to-mesenchymal transition drives renal fibrosis in mice and can be targeted to reverse established disease. *Nat. Med.* **21**, 989–997 (2015).
8. Bai, Q. *et al.* Epigallocatechin-3-gallate promotes angiogenesis via up-regulation of Nfr2 signaling pathway in a mouse model of ischemic stroke. *Behav. Brain Res.* **321**, 79–86 (2017).

9. Bose, M. *et al.* The Major Green Tea Polyphenol, (-)-Epigallocatechin-3-Gallate, Inhibits Obesity, Metabolic Syndrome, and Fatty Liver Disease in High-Fat–Fed Mice. *J. Nutr.* **138**, 1677–1683 (2008).
10. Chen, J.-H. *et al.* Green tea polyphenols prevent toxin-induced hepatotoxicity in mice by down-regulating inducible nitric oxide–derived prooxidants. *Am. J. Clin. Nutr.* **80**, 742–751 (2004).
11. Chyu, K.-Y. *et al.* Differential Effects of Green Tea–Derived Catechin on Developing Versus Established Atherosclerosis in Apolipoprotein E–Null Mice. *Circulation* **109**, 2448–2453 (2004).
12. Rezai-Zadeh, K. *et al.* Green tea epigallocatechin-3-gallate (EGCG) reduces β-amyloid mediated cognitive impairment and modulates tau pathology in Alzheimer transgenic mice. *Brain Res.* **1214**, 177–187 (2008).
13. Rezai-Zadeh, K. *et al.* Green Tea Epigallocatechin-3-Gallate (EGCG) Modulates Amyloid Precursor Protein Cleavage and Reduces Cerebral Amyloidosis in Alzheimer Transgenic Mice. *J. Neurosci.* **25**, 8807–8814 (2005).
14. Tipoe, G. L. *et al.* Epigallocatechin-3-gallate (EGCG) reduces liver inflammation, oxidative stress and fibrosis in carbon tetrachloride (CCl4)-induced liver injury in mice. *Toxicology* **273**, 45–52 (2010).
15. Kanlaya, R. *et al.* Epigallocatechin-3-gallate prevents TGF-β1-induced epithelial-mesenchymal transition and fibrotic changes of renal cells via GSK-3β/β-catenin/Snail1 and Nrf2 pathways. *J. Nutr. Biochem.* **76**, 108266–108266 (2020).
16. Liu, G. W. *et al.* Glomerular disease augments kidney accumulation of synthetic anionic polymers. *Biomaterials* **178**, 317–325 (2018).

17. Boronic Acid Copolymers for Direct Loading and Acid-Triggered Release of Bis-T-23 in Cultured Podocytes | ACS Biomaterials Science & Engineering. https://pubs.acs.org/doi/10.1021/acsbiomaterials.8b01163.
18. Yochum, Z. A. *et al.* A first-in-class twist1 inhibitor with activity in oncogene-driven lung cancer. *Mol. Cancer Res.* **15**, 1764–1776 (2017).
19. Salminen, A., Lehtonen, M., Paimela, T. & Kaarniranta, K. Celastrol: Molecular targets of Thunder God Vine. *Biochem. Biophys. Res. Commun.* **394**, 439–442 (2010).
20. Guo, L. *et al.* Targeted delivery of celastrol to mesangial cells is effective against mesangioproliferative glomerulonephritis. *Nat. Commun.* **8**, (2017).
21. Ryan, M. J. *et al.* HK-2: An immortalized proximal tubule epithelial cell line from normal adult human kidney. *Kidney Int.* **45**, 48–57 (1994).
22. Chiefari, J. *et al.* Living Free-Radical Polymerization by Reversible Addition−Fragmentation Chain Transfer: The RAFT Process. *Macromolecules* **31**, 5559–5562 (1998).
23. Matyjaszewski, K. Atom Transfer Radical Polymerization (ATRP): Current Status and Future Perspectives. *Macromolecules* **45**, 4015–4039 (2012).
24. Hong, J. *et al.* Stability, Cellular Uptake, Biotransformation, and Efflux of Tea Polyphenol (−)-Epigallocatechin-3-Gallate in HT-29 Human Colon Adenocarcinoma Cells. *Cancer Res.* **62**, 7241–7246 (2002).
25. Kaverina, N. V., Eng, D. G., Schneider, R. R. S., Pippin, J. W. & Shankland, S. J. Partial podocyte replenishment in experimental FSGS derives from nonpodocyte sources. *Am. J. Physiol. Renal Physiol.* **310**, F1397-1413 (2016).

26. Schneider, R. R. S. *et al.* Compound effects of aging and experimental FSGS on glomerular epithelial cells. *Aging* **9**, 524–546 (2017).

27. Kaverina, N. V. *et al.* Tracking the stochastic fate of cells of the renin lineage after podocyte depletion using multicolor reporters and intravital imaging. *PloS One* **12**, e0173891 (2017).